MONASH University

Production of bulk metallic glass sheet and its hybrid laminates

Daniel Raymond East

A thesis submitted for the degree of
Doctor of Philosophy

Department of Materials Science and Engineering, Monash University
Victoria, Australia

June, 2016

To Claire

Copyright notice

Abstract

Bulk metallic glasses (BMGs) are a class of alloys that can retain an amorphous structure when cast at moderate cooling rates. This allows castings to be produced that have an amorphous structure at cross-sections that can be measured in the millimetre length-scale. The transfer of BMGs from laboratory settings to that of commercially produced alloys has been limited to date, with the lack of a production process that can produce commercial volumes of material being a limiting factor. This project aims to investigate the production of BMG sheet and BMG/Al laminates using processes that are readily scalable for transfer to an industrial setting. It investigates the use of twin roll casting (TRC) and warm rolling to produce BMG and BMG/Al hybrid in sheet form. The $Mg_{60}Cu_{29}Gd_{11}$ alloy is chosen due to its low processing temperatures and its tolerance to oxygen allowing the processing to be conducted in air.

It is found that it is possible to produce 100% amorphous sheet at thicknesses between 1 and 3 mm from the $Mg_{60}Cu_{29}Gd_{11}$ alloy using TRC. The effects of casting conditions, including contact length, roll speed and sheet thickness, are investigated and the relationship of these variables to casting parameters are established.

Bulk metallic glass of the $Mg_{60}Cu_{29}Gd_{11}$ alloy possesses a supercooled liquid region (SCLR) where it flows and can be formed similar to a plastic. Rolling trials within the SCLR are under taken and the effects of rolling parameters on the structure of the glass are examined using differential thermal analysis, transmission electron microscopy and X-ray absorption fine structure analysis. It is found that, when rolling at a low strain rate, it is possible to roll the alloy without inducing crystallisation. However, dynamic crystallisation occurs when the alloy is rolled to large reductions at large stain rates.

The crystallised phase that is dynamically formed has a quasicrystalline structure with a composition similar to that of the amorphous matrix. The formation of this quasicystalline phase in the Mg-Cu-Gd system has not been reported previously. The formation of chemically similar quasicrystals from an amorphous matrix has been shown in other glass forming systems to be an indication of icosohedral short-range atomic ordering within the matrix.

Roll bonding is used to produce laminates from BMG and aluminium interlayers. Rolling is conducted within the SCLR of the glass. In addition to the temperature regime being within the SCLR the reduction applied to the laminate is in excess of 50%. This resulted in an improvement of over 90% in the flexural stress, flexural strain and Charpy impact energy over that of the monolithic glass.

Declaration

This thesis contains no material which has been accepted for the award of any other degree or diploma at any university or equivalent institution and that, to the best of my knowledge and belief, this thesis contains no material previously published or written by another person, except where due reference is made in the text of the thesis.

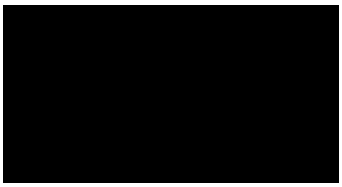

Daniel Raymond East

Acknowledgements

First, I would like to thank my supervisors Prof. Jian-Feng Nie and Dr. Daniel Liang for their guidance and patience in me over the years taken to complete this thesis. I am truly grateful for all their time spent assisting me.

Special thanks goes to Dr. Mark Gibson who acted as an unofficial supervisor during my candidature, his assistance was especially appreciated in the write up stage. I would also like to thank Prof. Michael Ferry, Dr. Colleen Bettles, Dr. Allan Morton and Prof. Kiyonori Suzuki for providing feedback during my candidature reviews.

I would like to thank Mr. Michael Kellam who assisted in conducting the twin roll casting experiments. The twin roll caster requires two operators working as a team and Michael was an excellent team mate.

I would like to thank the CSIRO staff development fund which provided funding for my time to work on this research.

I acknowledge the Monash Centre for Electron Microscopy (MCEM) for providing access to experimental facilities. I would like to thank Dr. Amelia Liu and Associate Prof. Laure Bourgeois for guiding me through the sample preparation and characterising amorphous materials.

I acknowledge the Australian Synchrotron, specifically the X-Ray absorption beam line and beam line scientist Dr. Bernt Johansson who went beyond the call of duty to assist in obtaining usable data of X-*ray absorption fine structure analysis.*

I would like to thank and acknowledge the help from Mr. Ian Madsen and Dr. Nathan Webster in conducting the in-situ XRD experiments.

Finally, my deepest thanks goes to my wife Claire who encouraged me to keep going when I wanted to give in.

CONTENTS

1 INTRODUCTION

Bulk metallic glasses (BMGs) are a class of alloys that retain their amorphous structure when cast using moderate cooling rates. By capturing the amorphous structure, BMGs have high strength, high corrosion resistance and high hardness when compared to the properties of the crystalline version of the same alloy. The presence of a supercooled liquid region (SCLR) is also another advantage of BMGs to their crystalline counterparts. A SCLR is a temperature region where the atoms are mobile enough to allow superplastic forming to take place, but transformation kinetics are not high enough to allow crystallisation to take place [1].

As the cross-section of a casting increases in size, the cooling rate at the centre of the casting decreases. The thickness at which crystals begin to form in a casting of BMG forming alloys is termed the critical thickness. To make components that are 100% amorphous, the critical thickness cannot be exceeded at any point within the components design. This limits the size of components that can be made from BMG forming alloys [2].

Flat products are the most common form of metallic products, occupying over 70% of the metals market [3]. The most common way of making flat products is to cast a large billet of material and mechanically reduce it in cross-section through an iterative sequence of either rolling or extrusion. This method of manufacture is not applicable to BMGs, as the cooling rates within the large billet castings are too low to prevent the formation of a crystalline structure. This excludes BMGs from the largest metallic materials market.

Twin roll casting (TRC) is a continuous casting process which produces sheet product directly from a melt. By utilising TRC it is possible to produce sheet with a 100% amorphous structure [4].

Most BMGs have very low elongation values in tension, due to their lack of microstructural barriers to shear band propagation. This means that BMGs can fail with sudden catastrophic failure through a single shear band. A method to counteract this is to introduce a second phase into the structure of the material. This can be done via in-situ or ex-situ methods [5].

Two major barriers to the implementation of BMGs into the marketplace are the lack of flat products and the low elongation to failure. To address these issues, this project aims:

- To develop a production method that can be used to produce BMG flat products and use scalable technologies to produce these products.
- To use scalable production technologies to produce BMG composite materials and determine the effect of composite structure on mechanical properties.
- To determine the influence of production variables on the structure of BMGs.

In Chapter 2 of this thesis, a review of the literature is presented. BMGs are introduced, the design rules for BMG systems and the typical properties of BMGs are described. The current production methods of BMGs, including both mould casting and continuous production methods, the operation and setup of the TRC system are described in detail. The current toughening strategies used for BMGs, including both in-situ and ex-situ toughening methods, and the atomic structure models of BMGs are presented, in addition to the current understanding on the relationship between the primary crystalline phase and the short-range atomic ordering of the amorphous phase. Finally, the current understanding of the effect of strain on crystallisation and the phenomena of dynamic crystallisation is given.

In Chapter 3, the experimental procedures used to produce the BMG products and the characterisation techniques used on these materials are explained in detail.

The production methods used to produce both monolithic glass and glass crystalline hybrid include centrifugal casting, planar flow casting (PFC), TRC and roll bonding. Mechanical testing methods included hardness testing, three-point bending test, Charpy impact testing and lap shear testing. To characterise the structure of the materials used in this thesis; X-ray diffraction (XRD), X-ray absorption fine structure analysis (XAFS), differential thermal analysis (DTA) scanning electron microscopy (SEM) and transmission electron microscopy (TEM) are also used.

The development of production methods which can be used to produce bulk metallic glasses are described in detail in Chapter 4. The effects of contact length, contact time and strip cross-sectional thickness on the production settings required to produce 100% amorphous material through TRC are explained. The major defects encountered during casting and the mechanisms behind defect formation are also presented.

In Chapter 5, the effects of strain, strain rate and temperature during rolling within the SCLR are investigated. The samples are characterised using a variety of techniques to examine the effect of processing on structure. X-ray absorption fine structure analysis revealed that the application of strain to a metallic glass causes the order within the amorphous structure to increase. In samples that processed under regions of high strain and high strain rate, quasicrystals are found to be dynamically crystallised within the amorphous matrix.

To improve the toughness and bending properties of the metallic glass samples, laminate composites are manufactured. The manufacture and mechanical properties of the laminates are described in Chapter 6. Laminates are tested for bending and impact resistance. The fracture faces within the laminates and monolithic samples are examined using SEM. The flexural stress and strain are measured along with the Charpy impact value of the monolithic and laminate samples. The laminates show an increase in each of flexural stress, flexural strain and impact energy absorption values.

Chapter 7 brings together the major conclusions from the thesis summarising the findings from the three experimental chapters.

Chapter 8 .is a list of publication outputs resulting from this thesis.

2 LITERATURE REVIEW

2.1 INTRODUCTION

The push to produce materials with high strength and lightweight is a constant driver of materials research. The need for lighter and stronger materials is a constantly varying target, set by the need to reduce weight in transportation and consumer electronic applications. This constantly moving goal has seen the development of high strength steels, aluminium, magnesium and titanium alloys.

One method of meeting the challenges of increasing performance of alloys is to control the microstructure of the alloy. The reduction in grain size of crystalline materials can improve the mechanical properties. Amorphous systems remove all grain structure from the material; this can lead to the improvement of the strength to near theoretical levels. Early amorphous alloy systems could only be produced through very rapid solidification rates and the cross-section of the material produced was limited to the micron scale. In 1969, Chen and Turnbull described the forming of a metallic glass in the Pd-Au-Si system that remained amorphous to thicknesses that could be measured in millimetres [6]. These systems are termed bulk metallic glasses (BMGs) and these can have strengths that are much higher than those of conventional crystalline materials of similar compositions. In 1993, Peker, from Caltech, reported an alloy that was based on the Zr-Be system that held its amorphous structure to over one centimetre. This large critical thickness and the use of non-noble metals created interest in BMGs as engineering materials [7].

Magnesium is the lightest of the common engineering alloys. The Mg-Cu-RE systems produce a number of BMG forming alloys and, as such; may prove to be the systems that can break into mass markets that value high strength, high stiffness and low weight such as transport and consumer electronics. Therefore this work will concentrate on the Mg-Cu-Y and Mg-Cu-Gd amorphous alloy systems.

The low toughness values of BMGs prevent them from being used as structural materials [1]. There are different approaches being applied to counteract the brittle nature of these materials. All methods involve the addition of secondary crystalline particles to the amorphous material. The secondary particles can be in the form of ceramic and metallic powders [8-10], wires [11, 12] secondary phases [5, 13] and laminates [14-16]. Each method of toughening has its own advantages and applications that will suit each particular need. For the improvement of toughness in sheet materials laminate structures have been chosen in this project as a suitable method for toughening magnesium-based metallic glass.

2.2 BULK METALLIC GLASS

The most dramatic illustration of non-equilibrium processing of a metal is the formation of an amorphous solid which, although looking and feeling the same, can possess physical and/or functional properties far removed from and often superior to its equilibrium crystalline counterpart.

The formation of BMGs occur in numerous alloy systems and there are three empirical rules design rules for their formation:

1. Multicomponent systems consisting of more than three elements.
2. Significant difference in atomic size ratios above about 12% among the three main constituent elements.
3. Negative heats of mixing among the three main constituent elements.

These three rules cause the stability of the liquid phase to increase and the initial nucleation and subsequent growth of crystals to be inhibited [17].

The mechanistic features of these three rules is shown in Figure 1, this diagram shows how the liquid is stabilized first and then the nucleation and growth of crystals is inhibited in glass forming systems.

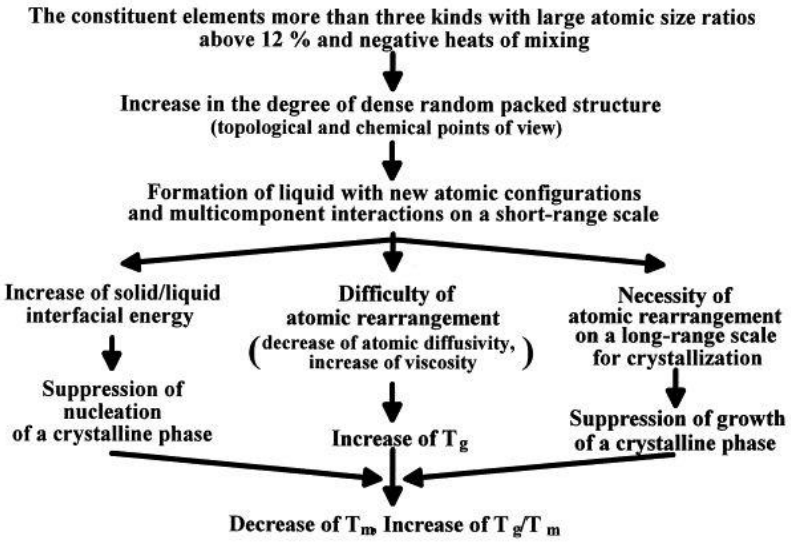

Figure 1 Mechanistic results of the empirical design rules for bulk metallic glass forming alloys [17].

Some of the main attributes of metallic glasses have described by Ashby and Greer [1] and are summarised in Table 1. Highly processable BMGs comprise a new class of engineering material that have attracted a significant degree of both scientific and technological interest in recent years [18]. Depending on the alloy composition, BMGs can present a combination of useful properties including high stiffness, high strength, high hardness, good wear and corrosion resistance, high fatigue strength and high workability. Another distinct advantage of BMGs over their crystalline counterparts is that they exhibit a SCLR between the glass transition temperature (T_g) and the onset of crystallisation temperature (T_x) where the viscosity decreases and the material becomes superplastic and will undergo large deformations without failure. Therefore, processing of BMGs via net-shape forming, micro- and nano-replication, extrusion, synthesis of amorphous metallic foams and superplastic forming of sheet material all become distinct possibilities. BMGs exhibit higher strain-rate sensitivity exponents when compared to crystalline systems that undergo superplastic

forming (SPF) and the strain rates that can be achieved with BMGs are about 2 to 4 orders of magnitude higher than those used in SPF crystalline metals. BMGs also display excellent surface finish even when processing in air. In addition, the deformation in BMGs takes place on the nano-scale, resulting in minimal surface roughening.

Table 1 Summary of properties of bulk metallic glasses [1].

Attributes	**Attractive Attributes**	**Unattractive Attributes**
General	• Absence of microstructural features such as grain and phase boundaries and of related composition variations (e.g. segregation). This allows components with features of near-atomic scale	• Present cost of components and processing • Optimisation of composition for glass-forming ability prevents easy optimization for other properties, including low density
Mechanical	• High hardness, H, giving good wear and abrasion resistance • High yield strength, σ_y • Fracture toughness K_c and toughness G_c can be very high • High specific strength, σ_y/ρ, $\sigma_y^{2/3}/\rho$ and $\sigma_y^{1/2}/\rho$ • High resilience per unit volume and mass , σ_y^2/E and $\sigma^2_y/E\rho$ • Low mechanical damping	• Severe localisation of plastic flow (shear-banding), giving zero ductility in tension • Fracture toughness K_c and toughness G_c can be very low • Can be embrittled by annealing • Small process-zone size (d < 1 mm) means that larger components may fail in a brittle manner
Thermal	• $T_g < T_x$ for some metallic glasses, allowing processing as a supercooled liquid	• Instability above T_x limits high temperature use
Electrical and magnetic	• High magnetic permeability • Resistivity is nearly independent of temperature	• Relatively high magneto-striction gives energy loss in oscillating field
Environmental and Chemical	• Lack of grain structure and associated microstructural features (e.g. solute segregation) gives corrosion resistance • Some compositions biocompatible	
Processing	• Low solidification shrinkage and lack of grain structure give high precision and finish in castings • The high viscosity and low strain-rate sensitivity of the supercooled liquid permit thermoplastic forming	• Not easily recycled once in a product (non-conventional compositions)

The terms T_g and T_x represent transformation temperatures in the structure of BMGs. Upon heating, the T_g temperature is the point at which the BMG transforms from a brittle material to a material that is able to flow. The viscosity of the BMG reduces as the temperature increases up to the T_x point. At the T_x temperature the BMG begins to crystallise, when this occurs the viscosity then decreases until the BMG transforms from a flowing amorphous material to a brittle crystalline solid. As mentioned previously, the temperature range between the T_g and T_x points of a BMG is called the SCLR. Within this region the flow characteristics of the material lend it to thermoplastic forming (TPF) techniques that can form complex parts. Techniques that fall into thermoplastic forming include blow moulding, injection moulding, stamping and extrusion. Table 2 lists some of the advantages and disadvantages of the thermo-based forming processes.

Table 2 Characteristics of thermoplastic forming of BMG [19].

Advantages of TPF-Based Processing	**Comment**	**Disadvantages of TPF-Based Processing**	**Comment**
Forming and fast cooling decoupled	Wide range of complex shapes can be net-shaped	Two- or more-step process	A requirement from the decoupling of cooling and forming
Highest dimensional accuracy	Due to negligible stresses and negligible solidification shrinkage		
Insensitive to heterogeneous influences	• Predictable and robust process • Allows to process in air		
Novel and unique process	New opportunities	Novel and unique process	Requires the development of novel processing methods
"Green" process	Due to low processing temperature and pressure you have the ability manufacture at net-shape		
Low capital investment	Also allows small series and custom shaped parts		

2.3 MAGNESIUM-COPPER-RARE EARTH BULK METALLIC GLASS

The Mg-Cu-Gd system is a good BMG former over a wide composition window. Figure 2 shows a large spread of BMG forming composition with a critical diameter (D_c) above 7 mm.

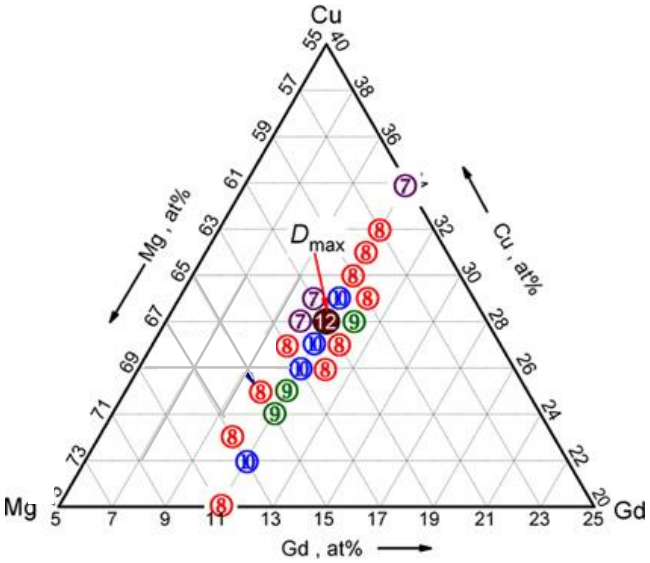

Figure 2 Composition range for BMG formation in the Mg–Cu–Gd ternary system. The number within the circles represents the critical diameter in mm [20].

A study by Men and Kim [21] shows the Mg-Cu-Gd system has a high tolerance for processing in air, other Mg-based BMG formers are sensitive to oxygen contamination and as such need to be cast in an inert atmosphere. This tolerance to casting in an air environment opens up several casting options that are not available to alloy systems that require an inert atmosphere.

The major problem with the Mg-Cu-Gd amorphous alloys is their brittleness. Due to the lack of microstructural barriers failure can occur along a single shear band. Changes in the height to diameter ratio (h / d) of the test specimen have some effect on the amount of strain that can be induced in a sample (see Figure 3). By decreasing h / d of the test sample the amount of strain applied to the sample can be increased. However, even with an h / d ratio of 0.25, the maximum strain achieved is still under 0.2%, and the failure is catastrophic in nature. Sudden failure occurs after a linear build up in stress [22].

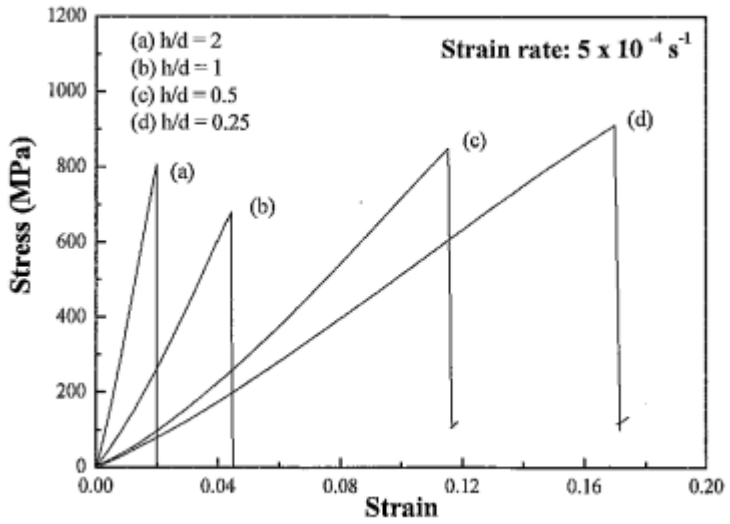

Figure 3 Compressive stress-strain curves of injection cast $Mg_{65}Cu_{25}Gd_{10}$ BMG with various height / diameter (h / d) ratios with a strain rate of 5 x 10^{-4} s^{-1} [22].

The thermal properties of the $Mg_{65}Cu_{25}Gd_{10}$ alloy when heated at 20 K·min^{-1} show a T_g temperature of 408 K and a T_x point of 478 K. This gives a SCLR of 70 K, a region in which thermoplastic forming can take place.

Within the SCLR changes start to take place, short range atomic ordering begins before crystallisation begining. A study by Li *et al.* shows that with heat treatment the short-range ordering in the $Mg_{65}Cu_{25}Gd_{10}$ alloy moves from a Cu-centred cluster to a Gd-centred cluster, and that this change in short-range atomic order causes embrittlement of the glass [23]. Other studies of atomic ordering in magnesium amorphous systems have concentrated on the effect of alloying additions combined with the effect of heat treatments on local ordering [24, 25].

Once the T_x has been exceeded crystallisation starts to take place. The phases reported initially to appear on crystallisation are Mg_2Cu and Cu_2Gd [26]. These phases are metastable, within this ternary composition space further phase changes taking place with an increase in temperature before the equilibrium phases of Mg_2Cu_9Gd and $MgCu_2Gd_2$ appearing [27].

Another Mg-Cu-Rare Earth BMG forming system is Mg-Cu-Y, this system has similar features to the Gd containing system in that it has a high oxygen tolerance, a wide SCLR and a good critical thickness (up to 7 mm) [28]. The critical thickness of both Y and Gd containing BMG alloys can be improved by adding silver to the alloy, however, because of the expense of silver this addition is not practical for commercial exploitation [29].

The Mg-Cu-Y system can also be modified by adding zinc, this addition causes a plate like long period order phase to form within the amorphous matrix [30]. Under a constant cooling rate the amount of second phase that is present is controlled by the composition ratio of Mg to Cu-Y. As the ratio increases, i.e. higher amounts of Mg within the alloy, the amount of second phase increases. This progression is illustrated In Figure 4, it can be seen that the amorphous content starts at 100% with a composition of $Mg_{65}Cu_{20}Y_{10}Zn_5$ and gradually increases its crystalline content with an increase in the Mg / Cu-Y ratio the volume fraction of second phase was measured as: (b) = 6%, (c) = 19%, (d) = 48% and (e)= 66%. These images were all taken from the core of a 3mm rod. In a cast piece the cooling rate varies from the skin of the casting to the centreline, which results in a mixed microstructure consisting of an amorphous skin, close to the mould wall, and a composite core, for samples with a diameter that exceeds the critical thickness for complete glass formation.

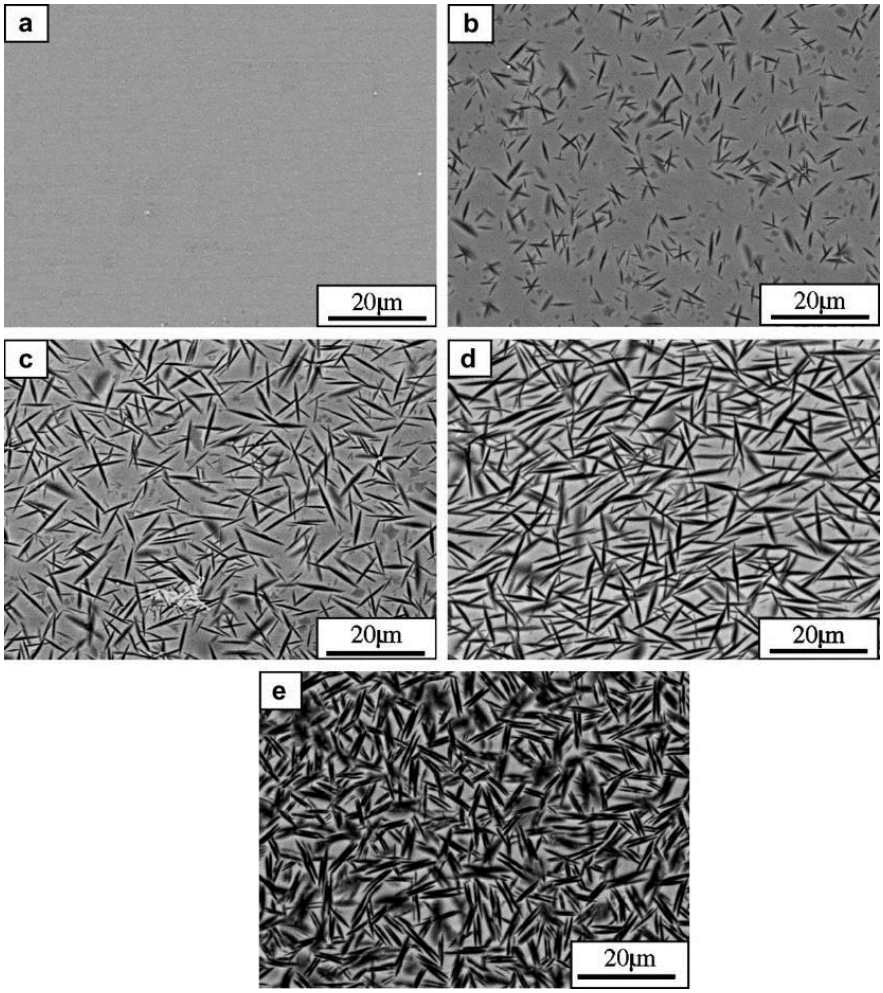

Figure 4 Backscattered electron SEM images taken from the centre of as-cast $Mg_{65+x}(Cu_{0.667}Y_{0.333})_{30-x}Zn_5$ rods with 3 mm diameter at: (a) x = 6; (b) x = 12; (c) x = 14; (d) x = 16; (e) x=18. [30].

2.4 PRODUCTION METHODS OF BULK AMORPHOUS ALLOYS

The ease of metallic glass formation is a strong function of the stability of the supercooled melt for the composition under consideration. In conventional metallic materials the critical time to the onset of crystallisation is extremely short (less than 10^{-5} seconds) and as a consequence it is difficult to avoid the nucleation and growth of crystalline phases even at the very high cooling rates associated with rapid solidification (up to 10^{6} $K \cdot s^{-1}$, the critical cooling rate, R_c, is indicated schematically by the blue curve in Figure 5). For compositions typical of amorphous alloys, crystal nucleation is delayed and therefore the 'nose' of the transformation curve can be by-passed and an amorphous metal is formed on cooling below the glass transition temperature, T_g. For certain alloy compositions, with exceptional glass forming ability (GFA), the supercooled liquid is so stable that it can resist the onset of crystal nucleation for hundreds of seconds and only relatively slow cooling rates (as little as 0.5 $K \cdot s^{-1}$, as represented by the red curve in Figure 5), are needed to produce a metallic glass. In these systems this glassy structure can be attained in large sections (up to centimetres thick) and these materials are known collectively as BMGs.

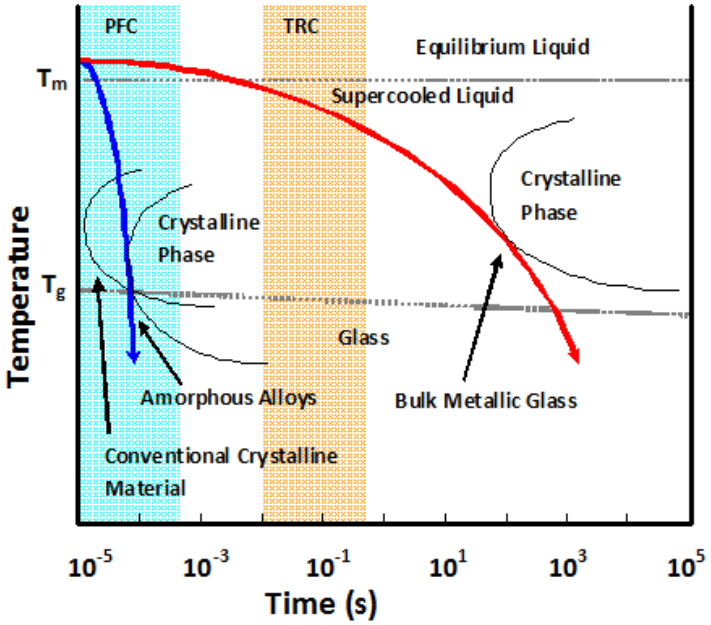

Figure 5 Schematic illustration of a series of continuous cooling-transformation (CCT) diagrams which of conventional crystalline materials, amorphous alloys and bulk metallic glasses respectively. The shaded region represents cooling rates typical of planar flow casting (PFC) and the orange shaded re typical of twin-roll casting (TRC) [31].

The maximum cross-section that can be achieved without violating the R_c is termed the critical thickness of the alloy [2]. The critical thickness imposes design constraints on parts made from BMGs direct from the melt, as at no point can the critical thickness be exceed. The size of cast parts that can be made from BMGs is restricted because of the difficulty casting narrow cross-sections.

Amorphous structures are produced when the solidification rate of the liquid alloy is of a sufficiently rapid rate to prevent crystallisation from taking place. There are several methods used to achieve the required solidification rates and they are summarised below.

2.4.1 Mould casting methods

- *Die-casting.* To maximise the solidification rates during casting, copper moulds are used when producing parts from bulk amorphous alloys. The copper mould has been used as a starting point for several casting processes. Laws, Gun and Ferry at the University of New South Wales have developed a low pressure die-casting system that has a copper mould coupled to a pressure injection furnace that can produce parts in a reproducible manner [32, 33]. At Liquidmetal Technology (a spinoff company from Caltech) a modified aluminium die-casting machine is used to produce commercial volumes of bulk amorphous alloy parts [34].
- *Injection casting* is a method in which a small charge of alloy is melted and then pressure injected into a copper mould [35].
- *Suction casting* is a casting method that is similar to injection casting but instead of applying a positive pressure to the melt in order to eject the melt to the mould, a negative pressure is applied, sucking the melt into the mould cavity [36].
- *Water quenching* is another production process for bulk amorphous alloys. In this process the alloy is heated into the molten state then dropped into an agitated water bath. There are two subsets to the water quenching method:
    - The alloy is heated in a silica tube and, when the desired temperature is achieved, the tube is dropped into the water bath, shattering the tube and rapidly cooling the melt into an amorphous solid [37].
    - The alloy is heated together with a metallic mould made of iron or another metal that will not react with the amorphous alloy. This assembly is then dropped into the water bath causing rapid cooling in the shape of the mould [38, 39].

2.4.2 Precursor production methods

Gas atomisation or PFC followed by powder metallurgy techniques are used to produce BMG parts [37, 40, 41]. However, these techniques are limited to producing small discrete articles or involve several post-cast processing steps.

- *Atomisation* is a method for the production of powders. The high solidification rates achieved in this process can cause an amorphous structure to form in bulk volume [41]. The powders produced then need to undergo consolidation to produce parts. When undertaking consolidation it is important not to apply excessive heat that can cause crystallisation of the amorphous material. Various consolidation methods can be used such as extrusion, plasma spark sintering and hot isostatic pressing [42-44].
- *Planar flow casting* is a method capable of producing amorphous ribbons. This process involves pouring molten metal onto a spinning copper wheel rotating at high speed. By controlling the pour characteristics and wheel speed, the thickness and structure of the ribbon produced can be controlled [45]. Similar to powder production the ribbons produced from PFC can be consolidated to produce thicker cross-section parts.

2.4.3 Twin roll casting

TRC is a manufacturing process capable of producing high quality sheet material several millimetres thick in long lengths. TRC is commercially used to produce steel [46, 47], aluminium [48], copper or other crystalline alloys and it is an important industrial technology due to its low energy consumption and high productivity.

Twin roll casting involves introducing molten metal into the roll gap of two counter rotating rolls. There are two distinct variants of TRC, i.e. horizontal or vertical TRC. In vertical TRC the strip exits the roll bite in a vertical direction. A molten pool is located on the upper side of the roll the solidifying metal prevents the melt from flowing through the roll gap (Figure 6).

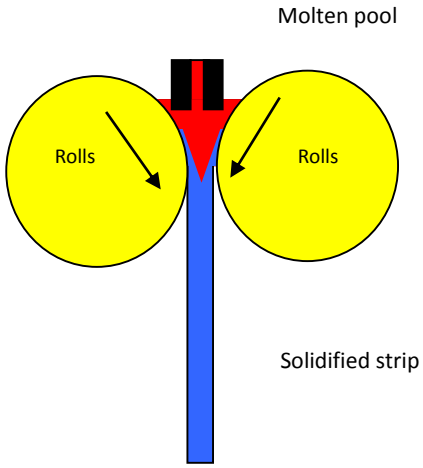

Figure 6 Schematic diagram of vertical twin roll casting, adapted from Ferry [49].

The second variant is horizontal TRC in this configuration the strip exits the roll in a horizontal direction (Figure 7). The melt is fed into the roll gap through a casting tip or nozzle. The melt solidifies on the roll surface and is cast and rolled in one operation. The melt is fed continuously into the roll gap replacing the material removed through the rolling process.

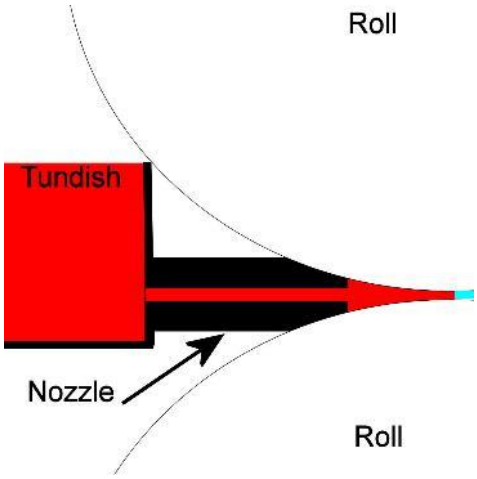

Figure 7 Schematic diagram of horizontal twin roll casting. Red region is molten metal, blue section solidified metal and the black regions are ceramic, adapted from Ferry [49].

The reduction in area as the melt moves through the roll gap causes pressure to be applied to the material thus increasing the heat transfer when compared with mould casting methods [50].

Bulk metallic glass sheet produced by TRC could be used directly or as a feedstock for downstream forming such as injection moulding, blow forming or hot pressing [19, 34, 51]. Twin roll casting has been attempted on the laboratory-scale to produce amorphous sheet in systems based on iron, zirconium and copper [3, 52, 53]. This sheet material could be used directly or as a feedstock for other downstream forming operations, this would significantly improve the economics of manufacture of BMG parts.

Iron-based amorphous alloys have been produced using TRC at POSTECH [53] and Tohoku University [52], the sheets produced were 1 mm and 0.5 mm in thickness, respectively. Both these programs failed to cast fully amorphous sheet with both examples showing small amounts of α-Fe within the microstructure. During the TRC of Zr-based alloy Vitreloy 1, crystalline particles were found in the as-cast sheet. The volume fraction of crystalline particles was found to be controlled by the superheat in the melt before twin roll casting. These crystalline particles, however, were found to increase the compressive strength of the strip cast material in comparison to permanent mould block cast samples of the same material using similar casting conditions [54]. The crystalline particles formed in the tundish and melt delivery system of the TRC unit, whereas when using the same melt temperature and injecting the melt straight into a copper mould no crystalline particles are formed. This would suggest the influence of the melt transfer parameters is more significant for the TRC compared with mould casting methods.

It is possible to produce sheet material through TRC that has an amorphous skin and a composite core. The transition of the microstructure occurs because of the decrease in cooling rate and solidification rate across the strip thickness. The higher cooling rate near the roll surface region compared with the interior region of the strip is responsible for the different morphology. The liquid metal near the roll surface is directionally solidified with rapid cooling rate and a large temperature gradient. The cooling rate near the roll surface is higher because the strip surface is in direct contact with the roll surface which increases the heat transfer from the liquid metal to roll surface [55]. Twin roll casting can be a very complicated system to model, incorporating heat flow, crystallisation kinetics and mechanical rolling. Each of these phenomena can cause feedback loops and have an effect on one another, but several TRC models have been developed. The POSCO developed model is

a thermal flow model that uses the FLUENT programming system. This model has been used to simulate the heat distribution through the roll gap in TRC of both crystalline and amorphous systems [4].

A model developed by researchers from Oxford University concentrates on casting narrow freezing range aluminium alloys [50]. This is by far the largest current market for TRC material. This model contains both thermal heat transfer components and solid deformation sections. The defects that most commonly appear in narrow freezing range aluminium alloys are rolling type cracking and buckling. These defects appear when the solidification front becomes uneven and the amount of rolling varies across the width of the strip. Small differences in the solidification front can be accentuated as areas that solidify early, have higher contact with the rolls, which leads to an increase in cooling rate and, in turn, causes the melt to solidify earlier still. Once these high cooling zones are established the hot melt can be channelled into the regions between these cool spots, pushing the solidification point further towards the roll bite. As such the nozzle design and heat balance across the width of the strip are very important for aluminium strip casting [50]. This model base has been modified by Duggan and Browne [56] to be applicable to zirconium-based BMGs. This model was used to simulate the casting of 2 mm thick $Zr_{41.2}Ti_{13.8}Cu_{12.5}Ni_{10}Be_{22.5}$ (Vitreloy 1) alloy strip and determined that acceptable casting speeds fall within the range 2.5 to 3.5 cm/s. They evaluated the effects of changing the strip thickness in relation to the range of casting speeds that would produce a fully amorphous strip and found that by doubling the strip thickness to 4 mm the range of possible casting speeds is greatly reduced to between 1 and 1.5 cm/s. As a result it is still possible to produce a fully amorphous strip but not at a rate that is as productive as thinner gauge strips. They also found that changing the heat transfer coefficient also had a significant effect on the allowable range of casting speeds. This variable, being very hard to determine, is one of the primary limits on the accuracy of their model.

Aachen University has a computational fluid dynamics based model that couples solidification, mechanical work and microstructural evolution. This model has been applied to magnesium crystalline materials. This model accurately predicts the formation of microstructural characteristics the main simplification of this model compared to the other two models is the simple letterbox nozzle used to inject melt into the roll gap and the corresponding limit of 100 mm to the strip width modelled [57].

Reasonable estimates of the heat transfer rates and in turn the casting conditions have been made and experimentally verified by Lee *et al.* [4] but if more accurate heat transfer figures could be obtained (via the inverse method) [58], the optimum casting conditions predicted by the model could be refined even more. In addition, the other extrinsic factors that affect the 'effective GFA' will need to be taken into consideration. This may become important as the possibility of TRC more and more amorphous alloys are examined. If these alloys are on the borderline of success then accurate modelling will help reduce the cost and effort of further development.

Published papers on operational variables of horizontal TRC of light alloys do not explain the effect of contact length on operational variables. The condition that is used for conventional TRC is roll load. The load variable in TRC is a function of the roll reduction in the solid zone, in order to change the load a combination of roll speed, contact length and melt temperature are changed. This variable is not as relevant to TRC of amorphous alloys due to the low loads that are applied to material in the SCLR and the very high loads that lead to stalling of the rolls in outside the SCLR.

2.4.4 Rolling bulk metallic glass

Rolling of BMGs within the SCLR has been performed previously to emboss fine surface detail onto the BMG [59]. Rolling has also been used to consolidate canned amorphous powders into a monolithic sheet [60]

Rolling trials conducted within the SCLR of Zr-based BMGs were found to cause dynamic crystallisation at reductions of 75%, at lower reductions no crystallisation was observed [61, 62]. The thermal properties of the rolled samples changed with rolling. The size of the dip prior to the T_g point reduces with an increasing amount of reduction see Figure 8. The reduction in the size of the dip is an indication of the reduction in the amount of free volume present within the glass structure [62].

In samples rolled within their SCLR as well as a decrease in the amount of free volume there is a corresponding increase in the hardness and strength of the rolled samples [61, 62].

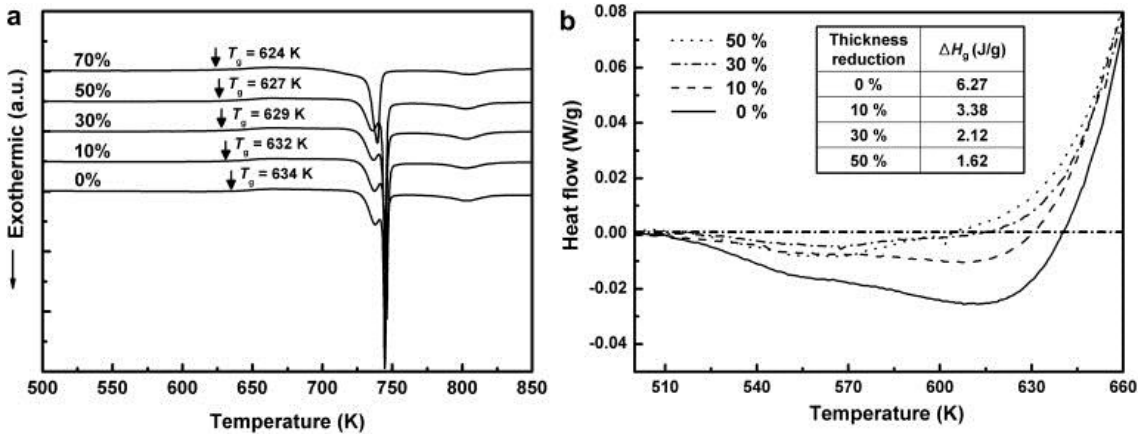

Figure 8 (a) DSC curves obtained from the rolled BMG samples of $Zr_{41.2}Ti_{13.8}Cu_{12.5}Ni_{10}Be_{22.5}$ and (b) magnified view of the DSC traces below T_g of (a) [62].

When rolling is used on crystalline metals, the effect of strain, strain rate and temperature on the resulting microstructure is well understood. The studies on rolling bulk metallic glasses within the SCLR have shown that at high reductions dynamic crystallisation is possible and rolling can cause the destruction of free volume within the glass. This thesis will aim to fill some of the gaps in knowledge of the relationship between rolling parameters and atomic arrangement in BMGs by undertaking a systematic investigation of the effects of strain, strain rate and temperature on $Mg_{60}Cu_{29}Gd_{11}$ bulk metallic glass. Previous work on the rolling on BMGs has not taken into account the effect of strain rate on structure change.

2.5 TOUGHENING METHODS FOR BULK AMORPHOUS ALLOYS

Magnesium-based BMGs are a strong, highly formable (under the appropriate processing conditions) class of material. The major shortcoming of this material is, however, the low level of toughness. The lack of toughness has been highlighted as an obstacle to the use of BMGs as structural materials. By combining a second ductile phase to form a hybrid structure the toughness levels can be increased substantially. This second phase toughening mechanism has been achieved via semi-solid processing in Zr- and Ti-based systems [5, 63]. Mg-based BMG systems also have compositions that form in-situ second phases, and research work is being conducted to exploit these systems for improved mechanical performance [64, 65]. Ex-situ methods of adding second phases to an amorphous matrix have also been trialled. Adding tungsten wire as a structural reinforcement has been tried with Zr-based amorphous alloys [11]. As with the previous reinforcement methods, the wires act to restrict shear band propagation and to promote the generation of multiple shear bands.

For most materials yielding near the crack tip is observed. As yielding takes place the crack tip is blunted, creating two new surfaces without advancing the crack tip. The volume of material that participates in yielding is given a radius termed the plastic zone radius (R_p). In metallic glasses cracks are blunted by shear bands that form at the crack tip, the length of these shear bands can be denoted as $2R_p$. For each metallic glass there will be a shear band length that defines the R_p value, each shear band is accompanied by a shear offset. At a critical shear band length the shear offset reaches a critical value and the crack grows [5]. The most successful mechanisms for toughening of bulk amorphous alloys involve introducing a second phase into the amorphous matrix that is spaced at a length scale similar to the plastic zone size ($2R_p$) of the alloy.

2.5.1 Dendrite/second phase composites

The inclusion of soft crystalline particles with in a glass matrix has been successfully optimised by Hofmann *et al.* [5] at Caltech. The two criteria that they developed for the formation of toughened metallic glass composites are:

- The introduction of “soft” elastic/plastic inhomogenities in a metallic glass matrix to initiate local shear banding around the inhomogeneity.
- Matching of microstructural length scales to the characteristic length scale R_p (for plastic shielding of a crack tip) to limit shear band extension, suppress shear band opening and avoid crack development.

In order to control the distribution of the second phase in a controlled manner semi solid casting techniques are employed. The melt is held in its semi solid zone and dendrites are allowed to grow to the desired volume fraction. The slurry is then cast creating an amorphous matrix with an even distribution of second phase dendrites. This control of the second phase distribution is a refinement of the second phase toughening method developed earlier by Hays *et. al*. [66].

There are Mg-based systems that form second phase composite structures with an amorphous matrix. Other research groups are looking at exploiting these systems for improved mechanical performance of bulk amorphous alloys [64, 65].

2.5.2 Ceramic particle metallic glass composites

"Hard" ceramic particles have also been used to improve the mechanical properties of amorphous alloys. This method has been shown to increase the strength of the alloys and increase the plasticity of the alloy slightly in compression [9]. The ceramic reinforcements act to stop the progression of shear bands and also act as a site of shear band initiation. The reported improvement in properties from this type of reinforcement is not as great as the improvements reported for soft phase reinforcement.

2.5.3 Fibre reinforcement

The addition of tungsten wire as structural reinforcement has been tried with Zr-based amorphous materials [11]. As with the previous reinforcement methods, the wires act to restrict shear band propagation and to promote the generation of multiple shear bands.

Carbon fibres have been used to reinforce Mg-based BMGs. In order to manufacture the composites the carbon fibre and the metallic glass were pressed together in the SCLR of the glass. The low temperatures within the SCLR of Mg-based glasses prevent the carbon fibres from reacting with the fibres. This results in excellent bonding between the carbon fibres and the amorphous matrix without any reaction products at the interface [67].

2.5.4 Glass/metal laminates

Laminate structures have been used to improve the impact resistance of BMGs. The work done on laminate structures involves press forming and forge casting of plates of crystalline metal and amorphous metal to improve impact strength of the alloy. All previous work has involved studies using Zr-based BMGs [14, 15, 68]. When designing BMG laminates the influence of the mechanical properties of the constituent materials need to be considered. It has been shown by Qiao *et al.* [69] that combining a glass matrix, with high yield strength uniformly dispersed ductile secondary crystalline phase, then a composite, that displays work hardening with high yield strength and homogenous deformation, can be produced. By following this strategy a similar improvement in the properties of BMG laminates could be achieved. Roll bonding is a method to produce large volumes of laminate material in a continuous manner. When roll bonding large rolling reductions are required in order to create strong interfacial bonds between layers [70]. The combination of TRC to produce the BMG and roll bonding to join the metallic glass to a crystalline metal layer results in a process that can be up-scaled readily. This project aims to produce a continuous production methodologies coupled with improved mechanical properties to potentially open the market for BMGs to structural applications.

2.6 PRODUCTION METHODS OF BULK METALLIC GLASS LAMINATES

Press forming and forge casting have been used to produce BMG laminates, both are press-based processes and as such the size of the part that can be made is limited by the press size.

2.6.1 Press forming

Press forming to produce laminates involves building up layers of glass and metal. Ragani *et al.* [71] describes the formation of metallic glass / light alloy laminates. In press forming he has found that the bonding between the metal and glass layers is improved with an increase in pressing temperature and pressure. For each temperature a strain of 0.5 was applied to each sample. Four different pressing temperatures were trialled 673, 683, 693 and 703 K. As the temperature of the work pieces increases the viscosity of the glass decreases. This change in viscosity of the glass changes the amount of deformation that is undertaken by the glass compared to the amount of deformation in the metal interlayer. The sample processed at 673 K is outside the SCLR of the alloy and as such the amount of strain accommodated by the glass layer is 0.04 the remainder of the strain is accommodated within the metal layer. At the highest temperature (703 K) 0.90 of the strain is accommodated by the glass layer. The pressing temperature is limited to the upper level of the SCLR of the metallic glass in order to prevent crystallisation of the glass. Ragani *et al.* [71] also states that deformation within the metal layer causes virgin metal free of oxide contamination to contact the metallic glass improving the bond strength [71].

2.6.2 Forge casting of bulk metallic glass

Forge casting is a processing route that is similar to squeeze casting in that pressure is applied to melt during solidification in order to increase the cooling rate achieved. Forge casting involves heating an ingot of bulk amorphous forming alloy within a press, Figure 9. When the alloy has reached the desired temperature the press is closed quenching the alloy between two water cooled blocks. In order to form a laminate structure a metal sheet is placed within the press and when the press closes the metal sheet comes into contact with the solidifying glass, a multilayer laminate can be produced by repeating this process several times [68].

For the alloy DH1 ($Zr_{36.6}Ti_{31.4}Nb_7Cu_{5.9}Be_{19}$) used in this study, the temperatures used are within the semi-solid region of the alloy, which is between 1073 and 1173 K [5]. As this is a hybrid casting / forging process the temperatures used are higher than the press forming process described previously. The use of high temperatures means that common engineering materials such as aluminium and magnesium alloys cannot be used as these temperatures are in excess of the melting points of these alloys. Due to this restriction only metals with melting points that exceed 1173 K can be used for this process.

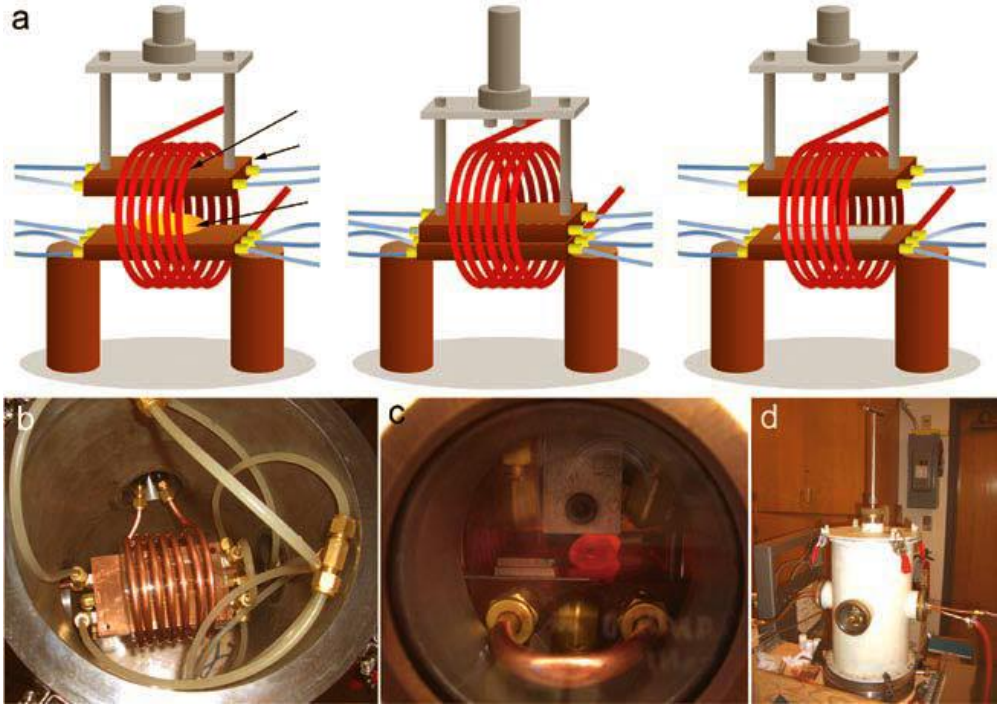

Figure 9 Forge casting assembly. (a) Schematic diagram of the process step 1 metal charge being inductively heated. Two water-cooled copper plates brought together to forge cast sample. Plates open with formed sample attached to bottom plate. (b) Top view of assembly. (c) Side view of assembly showing water cooled plates. (d) Outside of vacuum chamber press mechanism can be seen at top of chamber [11].

2.6.3 Epoxy bonding

It has been shown that by breaking the monolithic structure of the BMGs, by layering sheets of glass bonded by an epoxy, an improvement in toughness can be achieved [16]. The epoxy layer acts as a barrier to shear band movement stopping the catastrophic failure of the part across a single shear band.

2.7 THERMAL STABILITY OF MAGNESIUM BULK METALLIC GLASS

Metallic glasses are in a metastable state. It has been proposed in a predictive model that solidification rate has an effect on the atomic arrangement in glasses. Higher solidification rates result in a structure closer to the structure of the liquid, whereas solidification rates that are closer to the critical rate create a structure while still amorphous does contain short-range order. This predictive model has not been experimentally confirmed [72]. With the application of energy to the system changes will occur within the structure of the glass. From the amorphous structure short-range atomic ordering can take place prior to the formation of crystals [73]. When crystallisation occurs the equilibrium phases, may or may not form directly from the glass. Metastable crystalline structures can be formed, which, in turn, will transform further into the equilibrium phases [27].

2.7.1 Crystallisation kinetics of bulk metallic glass

The crystallisation of a BMG is a kinetically controlled process. The variation in the heating rate during thermal analysis testing has been shown to affect the value of the glass transition temperature, T_g, and the crystallisation temperatures, T_{x1} and T_{x2}, of the glass. As can be seen in Figure 10, an increase in heating rate during DTA causes an increase in value for the various thermal transformations [74]. This region is used for the superplastic forming of parts using amorphous alloys [19]. Figure 11 shows a tensile test conducted within the SCL region of $Mg_{65}Cu_{25}Y_{10}$ BMG showing an elongation of over 1000% [75].

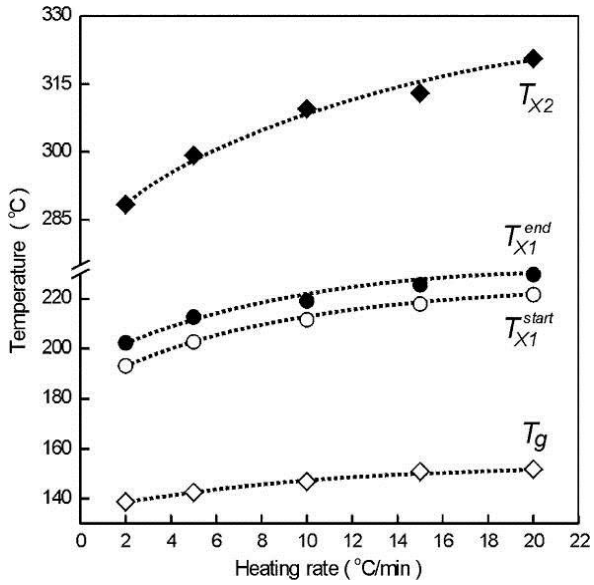

Figure 10 Effect of heating rate on the characteristic temperatures T_g, T_{x1}^{start}, T_{x1}^{end} and T_{x2} (the start and end temperatures for the primary crystallisation transitions from an amorphous base of $Mg_{65}Cu_{25}Y_{10}$, T_{x1}^{start}, T_{x1}^{end}. T_{x2} is the temperature for a second crystallisation event.) The error associated with each temperature measurement is ±3 °C (trends in the data are illustrated by the dashed lines and are provided as a guide to the eye) [74].

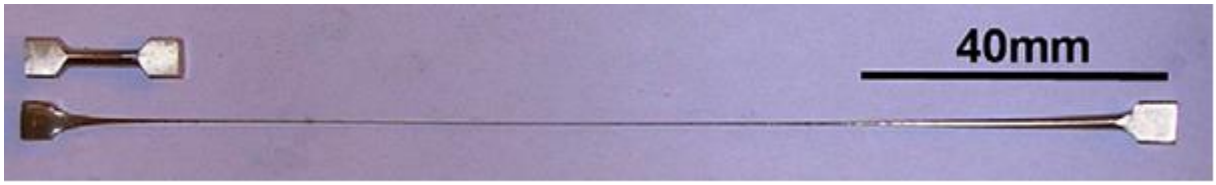

Figure 11 As-cast and deformed $Mg_{65}Cu_{25}Y_{10}$ glass samples showing an elongation of over 1000% (conditions: T = 433 K and $\dot{\varepsilon}$= 10−2 s^{-1}) [75].

Deformation of a BMG within the SCL region has been shown to have an effect on the crystallisation of the $Mg_{60}Cu_{30}Y_{10}$ [66] and the $Zr_{52.5}Al_{10}Ti_5Cu_{17.9}Ni_{14.6}$ glassy alloys [74, 76]. These two reports investigate the system respectively. Nieh *et al.* [46] has shown that an application of strain to a sample, within the SCLR, can cause the initiation of crystallisation. Figure 12 shows the initial stages of crystallisation with an amorphous matrix in the $Zr_{52.5}Al_{10}Ti_5Cu_{17.9}Ni_{14.6}$ system [76]. Gun *et al.* [74] have shown a similar result in a $Mg_{65}Cu_{25}Y_{10}$ alloy, with crystallites forming in the deformed regions, Figure 13.

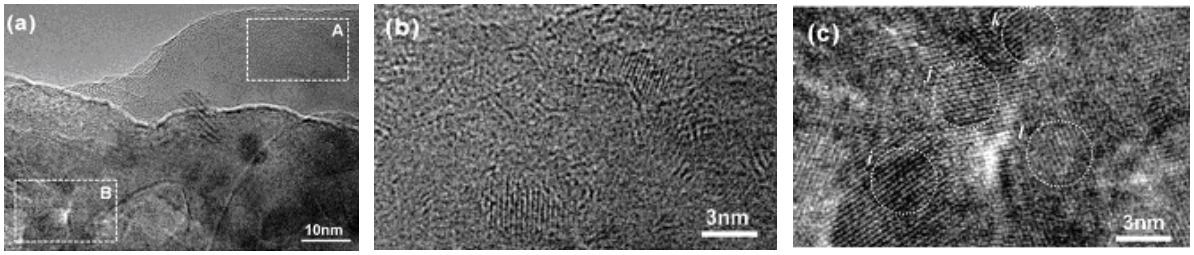

Figure 12 TEM image from the fracture tip of the amorphous $Zr_{52.5}Al_{10}Ti_5Cu_{17.9}Ni_{14.6}$ sample deformed at 683 K at a strain rate of 10^{-2} s^{-1}. (b) High magnification of area A in (a) showing individual nanocrystals (3 nm) dispersed in an amorphous matrix. (c) High magnification of area B in (a) showing aggregates of nanocrystallites (nanocrystallites are 5–10 nm in size) [76].

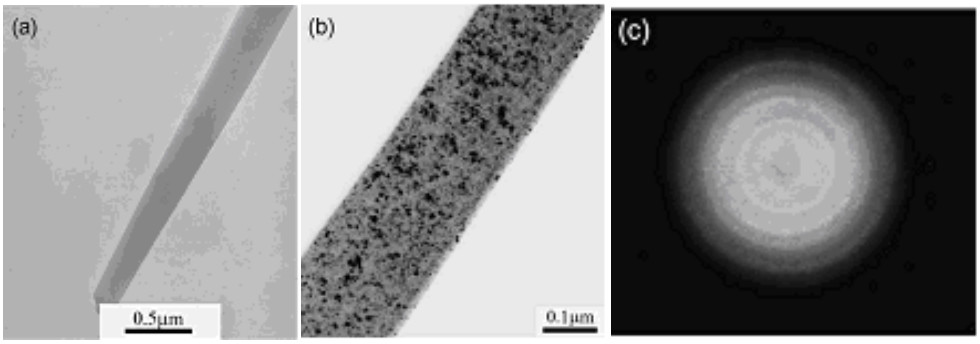

Figure 13 Bright field TEM micrographs of $Mg_{65}Cu_{25}Y_{10}$: (a) tip of a fractured sample after tensile testing at 438 K and 10^{-3} s^{-1} and (b) partly crystallized microstructure in the tip region. (c) SAED pattern indicating the nanosized crystallites shown in (b) [74].

The crystallisation of $Mg_{60}Cu_{30}Gd_{10}$ has been shown to involve the formation of metastable phases when heated at 40 K/min (see Figure 14) [27]. The XRD peaks from the traces taken at 488 K and 573 K show the same diffraction peaks present at these two temperatures. However, when compared to the equilibrium trace different phases are present. Soubeyroux *et al.* reported that Mg_2Cu (orthorhombic a = 0.0907 nm, b = 1.824 nm, c = 0.528 nm) and Cu_2Gd (orthorhombic a = 0.4320 nm, b = 0.6858 nm, c = 0.528 nm) phases formed first on crystallisation of amorphous $Mg_{65}Cu_{25}Gd_{10}$ (Figure 15) [26]. The equilibrium phases reported for the $Mg_{60}Cu_{30}Gd_{10}$ alloy are Mg_2Cu_9Gd and $MgCu_2Gd_2$. These phases have not been fully characterised, with only the chemical compositions reported. Neither of these phases are detected in the initial crystallisation of the amorphous ribbon Figure 14 [27].

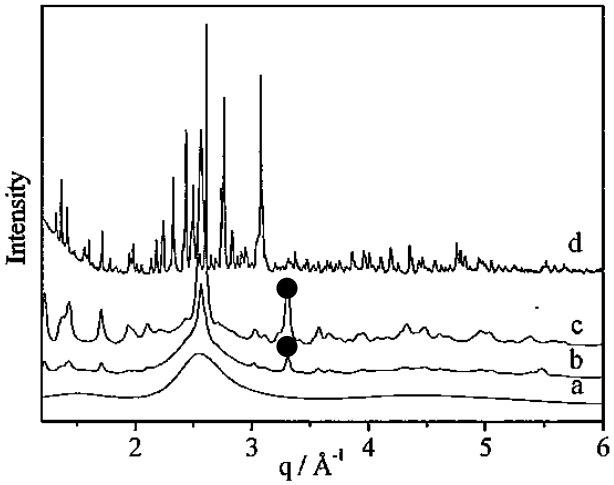

Figure 14 Selected XRD traces from in-situ experiments for $Mg_{60}Cu_{30}Gd_{10}$ ribbon, (a) 313 K, (b) 488 K, (c) 573 K, and (d) $Mg_{60}Cu_{30}Gd_{10}$ annealed master alloy. Peaks marked with a circle are not present in the scan from the equilibrium condition [27].

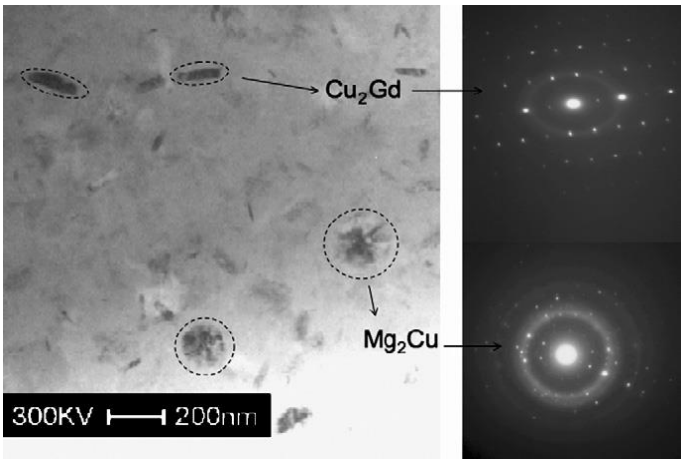

Figure 15 Bright field TEM image and electron diffraction patterns obtained from $(Mg_{0.65}Cu_{0.25}Gd_{0.1})_{97}Fe_3$ BMG showing Mg_2Cu and Cu_2Gd phases [26].

2.7.2 Short-range atomic ordering

Researchers have investigated crystallisation through strain by compression and tensile tests. The results from these studies show that the amount of strain and the temperature of deformation influence the formation of crystalline phases [77]. Crystallisation through strain has been observed in magnesium-based glasses [74, 75, 78]. The metastable primary phases that form in a Mg-Cu-Gd based glass, when subjected to compressive strain, has been characterised by Puech *et al.* [79], with the reported phases being Cu_2Gd and Mg_2Cu.

Formation of metastable quasicrystals from a BMG has been attributed to the icosohedral short-range ordering (ISRO) of the liquid, which is subsequently retained in the glass upon quenching. The growth of ISRO in the supercooled liquid raises the nucleation barrier for the formation of competing crystalline phases and increases the viscosity of the liquid to improve the glass forming ability [80]. As such, with the ISRO of the glass being the predominant structure, it has been suggested that the energy barrier to form quasicrystalline phases, during subsequent crystallisation transformations, is lower than that for crystalline phases [81, 82].

There have been two suggested atomic arrangement structures for BMGs based on Mg-Cu-RE type systems. These structures have been modelled using molecular dynamic modelling and have not been confirmed by experimental observation. The structure of the $Mg_{65}Cu_{25}Y_{10}$ metallic glasses has been studied by Ding *et al.* [83] and the short-range atomic ordering of this glass has been reported as a mixture of Cu centred tricapped trigonal prisms and bicapped square antiprisms. An alternative structure, of an icosohedral short range order, has been proposed by Gao *et al.* [84] for a $Mg_{60}Cu_{30}Gd_{10}$ alloy by using molecular dynamic modelling. To measure the atomic spacing within amorphous materials, X-ray absorption fine structure (XAFS) studies provide a method to measure the nearest neighbour distances. The effects of alloying additions on the structure of magnesium based BMGs have been examined by XAFS [24, 85]. XAFS have been used to investigate the structure of a BMG when annealed below the glass transition point of the alloy [86]. Thus, XAFS could also be used to study the effect of deformation on the structure of a BMG. The effect of rolling within the SCLR on the structure of BMGs has not been studied previously. In this work the effect of rolling on short range atomic ordering prior to crystallization is investigated using XAFS. The XAF investigation shows that with increasing levels of strain induced by rolling, within the SCLR, the short range atomic ordering within the glass structure is increased. In previously conducted Extended X-ray XAFS studies on short-range ordering in magnesium metallic glass alloys PFC was used to produce ribbons, and then the effect of various heat treatments on the local ordering of the atoms was investigated [85]. XAFS measurements are able to identify the nearest neighbour and next nearest neighbour elements, measure the bond length and bond angle of a targeted element. From this data it is possible to determine the short-range order, to the range of several elements around a core element (clusters). XAFS can show ordering on a scale of elemental pairs where as XRD scans may show these materials to be amorphous with no structure detectable. This change in short-range atomic ordering may explain changes in strength and ductility that have been detected in amorphous alloy systems with heat treatments below the crystallisation temperature of the alloy. One such study by Li *et al.* [23] shows that with heat treatment the short-range ordering in the $Mg_{65}Cu_{25}Gd_{10}$ alloy moves from a Cu-centred cluster to a Gd-centred cluster, and that this change in short-range atomic order causes embrittlement of the glass. Other studies of atomic ordering in magnesium amorphous systems have concentrated on the effect of alloying additions combined with the effect of heat treatments on local ordering [24, 25].

2.8 SUMMARY

Bulk metallic glasses are a group of alloys that can maintain an amorphous structure when cooled at moderate cooling rates. To achieve the “bulk” term when casting using a copper mould the cross section that remains amorphous should be equal or greater than 1 mm. A high proportion of metallic glass research has focused on small lab based production methods and as such there is limited knowledge on the effect of processing conditions on bulk metallic glasses using scalable industrial processing techniques. This project concentrates on using scalable production techniques to manufacture sheet and laminates from bulk metallic glass. The alloy system $Mg_{60}Cu_{29}Gd_{11}$ is chosen to conduct this work due to its ability to be processed in air and its good glass forming ability. To produce sheet, twin roll casting is used. Twin roll casting is a production process that produces sheet directly from a melt. The use of rolling to produce flat products from bulk metallic glass has not been investigated in depth. In crystalline metals the relationship between rolling parameters and microstructure are relatively well understood, but this is not the case with metallic glasses. In this work an investigation into the effect of rolling parameters on the resultant structure is carried out for $Mg_{60}Cu_{29}Gd_{11}$ bulk metallic glass. Due to the lack or grain boundaries or slip systems bulk metallic glasses often have strengths that exceed that of their crystalline counterparts. However, this lack of internal structure also makes bulk metallic glasses brittle materials with failure occurring across a single shear band. In order to provide barriers to shear band propagation secondary crystalline phases can be added to the amorphous matrix. This can be done either by in-situ methods such as semi-solid casting or ex-situ methods such as melt infiltration. In this project an ex-situ method to introduce the second phase will be used. Roll bonding will be developed as a process to produce laminates. Roll bonding is chosen as it is a scalable process and the spacing of the crystalline and amorphous layers can be controlled. Material that has been produced via casting and rolling will be studied to understand the relationship between processing parameters and atomic arrangement of the glass. This will be done on the amorphous material prior to crystallisation and on crystalline particles that form dynamically during processing or through heat treatment.

3 EXPERIMENTAL PROCEDURES

3.1 INTRODUCTION

The aims of this work are twofold; the first is to develop scalable production methods for the manufacture of bulk metallic glass sheet and its hybrid laminates. The second is to study to study the influence of processing conditions on the structure of the glass.

In order to achieve this, the following experiments are conducted:

- Twin roll casting production trails – to identify the production variables required to produce castings with a 100% amorphous structure.
- Rolling trials – to identify the effect of strain and strain rate on the ability to roll bulk metallic glass within the supercooled liquid region.
- Three-point bend trials – to measure the effect of laminate composition on the mechanical performance of the laminate.
- Microstructural characterisation using transmission electron microscopy (TEM), X-ray diffraction (XRD), differential thermal analysis (DTA), and X-ray absorption fine structure analysis (XAFS) – to determine the effect of production variables on the structure of the glass. The effect of post-production processing on structure is also examined.

These are required to set up the production variables for amorphous material (Chapter 4), the effect of processing on structure development (Chapter 5) and the effect of laminate composition on mechanical properties (Chapter 6).

3.2 CENTRIFUGAL CASTING

Centrifugal casting is a production method that allows small samples to be cast. The type of caster used in this work is a Minco Rotocast 500 centrifugal casting machine Figure 16. This machine consists of an induction coil that heats a metal charge located on an arm. Few of the production variables in the Rotocasting process can be monitored or altered. The rotational speed is set and the temperature of the melt prior to casting is not monitored. When setting the heating time a viewing window allows the crucible to be monitored visually. Once the metal is molten the coil is lowered and the arm is rotated. This rotation causes the melt in the crucible to flow into the mold located at the end of the rotating arm through centrifugal force. The operating parameters that can be adjusted in the Rotocasting process are the power to the induction coil, the time of heating and the duration of motion of the rotating arm.

Once the coil is lowered the arm is spun for a set period of time. This time can be varied between 5 seconds and 1 minute. The system is fitted with 5.5 kW power supply, with a frequency of 60 Hz. The melting settings for magnesium BMG forming alloys is 30 seconds melt time, with a power input of 30% of maximum, with a spin time of 20 seconds.

The moulds are made from 38 mm diameter copper rods the melt flows into the mould cavity though a melt nozzle. The centrifugal force of the rotating arm drives the melt into the mould cavity. The contact between the melt and the mould is excellent due to centrifugal force caused by the spinning arm. An image of the process is shown in Figure 16.

Before the Rotocaster can be used for casting, the spinning arm has to be balanced.

The procedure for balancing the arm is:

1. Load the mould into the holding bracket (d).
2. Close the safety cover and press the spin arm button on the control panel.
3. If the arm is out of balance, the machine will have a large amount of vibration.
4. If the machine vibrates, press the stop button and when the arm has stopped spinning open the safety cover.
5. Adjust the counter weight (a) by loosening the lock nut and moving the weight along the threaded bar. Relock the counter weight.
6. Go to step 2 and repeat procedure until the arm swings without vibration.

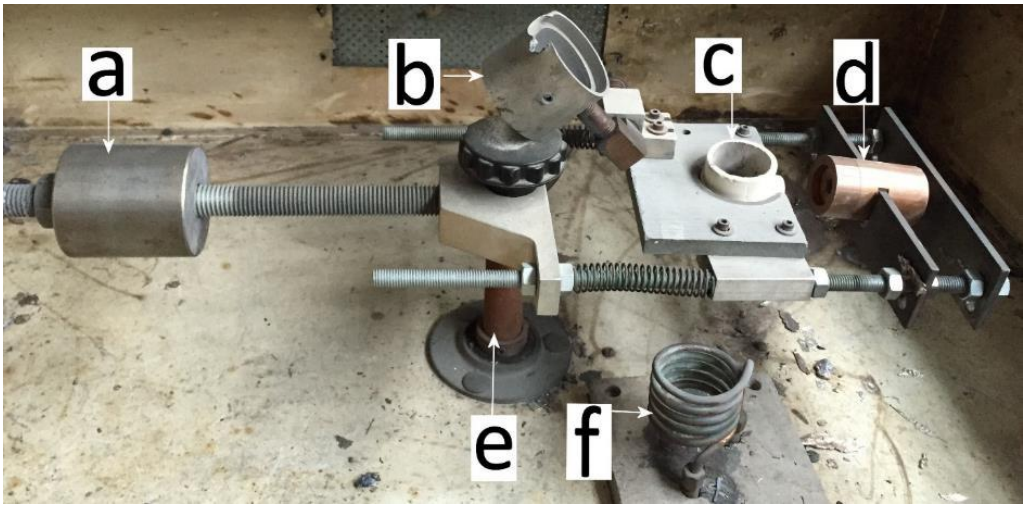

Figure 16 Rotocaster assembly. (a) Counter weight. (b) Protective gas cover lid. (c) Crucible. (d) Mould. (e) Central shaft, rotating axis. (f) Induction coil.

When casting a sample the following procedure is used:

1. The charge is placed in the crucible (c).
2. The mould is placed in the holding clamp and a transition piece is placed between the mould (c) and the mould (d).
3. The rotating arm is moved by hand until the crucible is above the induction coil (f).
4. Raise the induction coil and adjust the position of the crucible to ensure that the crucible is not touching the induction coil.
5. Inspect the induction coil for holes or areas where the coils may be touching.
6. Place the protective gas cover lid on the crucible.
7. Close the safety cover.
8. Turn on the induction coil. The protective cover gas should start automatically at this point.
9. The induction power can be adjusted by the large dial on the left hand side of the caster.
10. When the charge is molten, press the stop melting button.
11. At this point, the induction coil should drop and the rotating arm should spin, pushing the melt into the mould via centrifugal force.
12. When the arm stops spinning, the safety cover lid can be raised and the mould removed from the arm.
13. The mould can now be disassembled and the casting removed.

3.3 PLANAR FLOW CASTING

Planar flow casting (PFC) is a production method for thin metallic ribbons. During this process the melt is ejected onto a wheel rotating at high speed. The melt is cooled rapidly on the roll surface and separated from the wheel via centrifugal force and delivered into a take-off chamber.

The PFC process is conducted within a vacuum chamber, which is evacuated to a pressure of 900 mbar and then back filled with argon. This process is repeated three times to reduce the oxygen content of the chamber. The oxygen gauge on the chamber moves off scale at 0.1% oxygen and this level is reached after the first flush.

BMG ribbons of $Mg_{60}Cu_{29}Gd_{11}$ composition are made via PFC, ribbons 25 mm wide and 100 μm thick are produced using a 1 mm wide nozzle slot and a 933m.min^{-1} wheel speed. The casting wheel is a 450 mm diameter Cu-Be wheel.

An image of the equipment used is given in Figure 17. During casting, the melt is heated in the induction coil (b), while the temperature is recorded via the optical pyrometer (a) which has a line of sight to the melt through a sapphire window. The ribbon is cast against the spinning wheel (c) when the ribbon has solidified it leaves the roll surface and it collects in the take-off chamber (d).

The processing variables, such as slot geometry, metallostatic melt head height and wheel speed, are varied and the resulting effect on ribbon quality will be studied. The dominant variable in the production of amorphous ribbon is controlling the flow of metal onto the roll surface. Changing of the roll speed effected the ribbon thickness with slower speeds resulting in thicker ribbon.

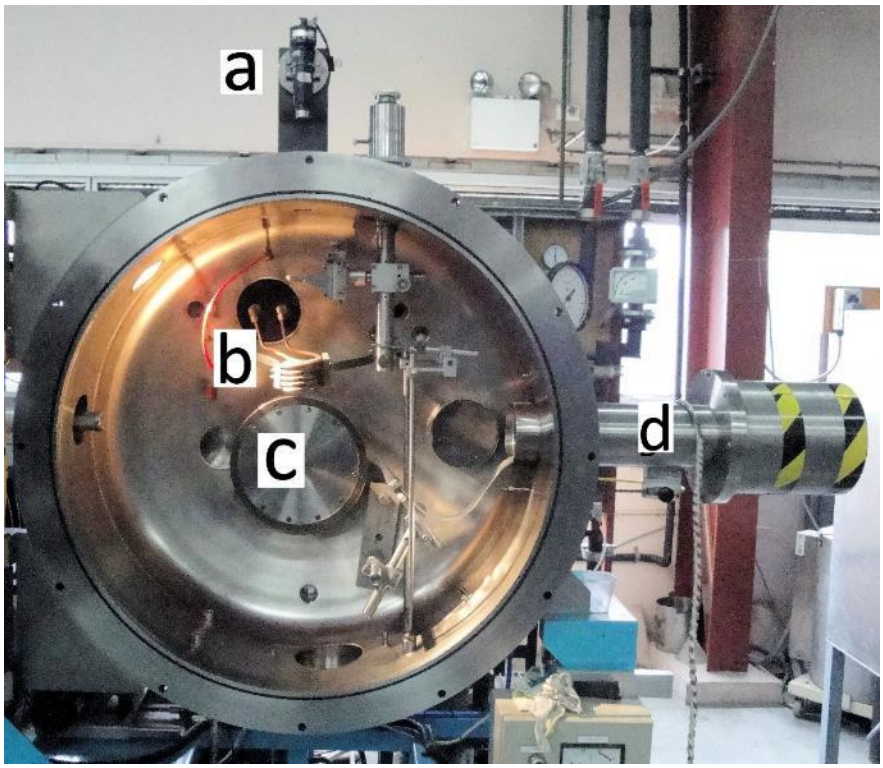

Figure 17 Phoenix Scientific Industries planar flow caster. (a) Mirkon optical pyrometer. (b) Induction coil. (c) Cu-Be alloy shell casting wheel. (d) Take off Chamber.

3.4 TWIN ROLL CASTING

Twin roll casting: a casting method where a melt is delivered into the roll gap of two counter rotating rolls. The melt solidifies on the roll surface and is rolled and cast in one production step. This process can produce material at thicknesses between 1 and 8 mm. For commercial aluminium alloys, sheet can be continuously cast at a width of 2 metres and a thickness of 5 mm using this technique.

The melt is cast and rolled in one process producing sheet or strip in a continuous manner. The melt delivery system consists of a furnace, transfer tube, tundish and a nozzle. Variables in the casting process such as contact time between the rolls and the melt, the contact length from the mouth of the melt delivery nozzle to the roll bite and the roll bite separation distance are systematically varied to establish the operating window for the process.

The melt is held in an electrical resistance furnace and held at the desired temperature. In this lab-scale work a furnace with a 5 kg capacity of $Mg_{60}Cu_{29}Gd_{11}$ is used. When the desired temperature has been achieved the melt is transferred to the tundish by pressurising the furnace to push the melt through the transfer pipe into the tundish. The amount of melt within the tundish controls the metalostatic head pressure that is applied to the melt as it is exiting the nozzle orifice and contacts the roll surfaces. A schematic of the TRC system is shown in Figure 18, the furnace, transfer tube and tundish are all held under a protective atmosphere of 0.3% SF_6 in nitrogen, to minimise the oxidation of the reactive magnesium based melt.

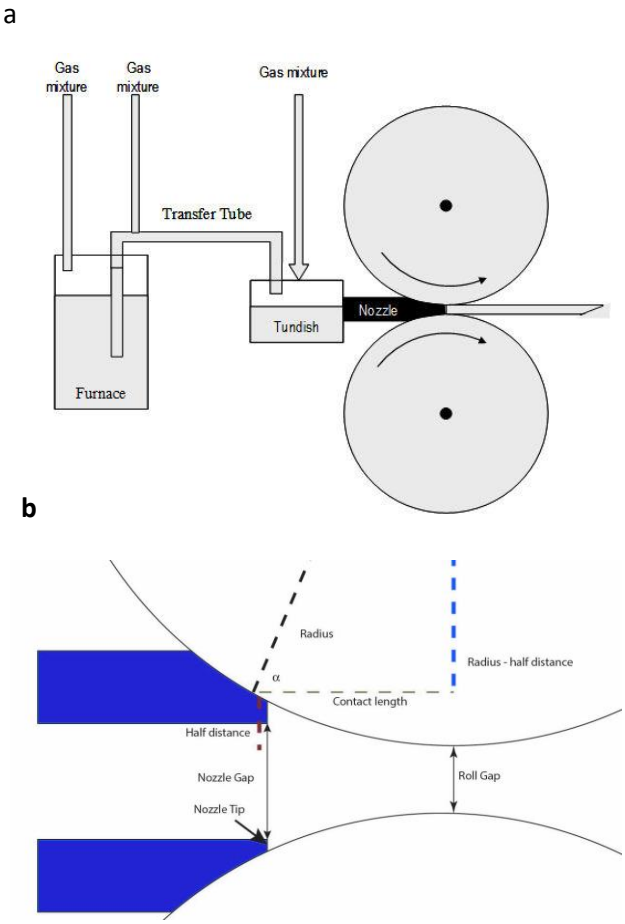

Figure 18 (a) Schematic diagram of the TRC process. Counter rotating water-cooled rolls have a Cu-Be shell that allows high heat transfer, (b) detailed schematic showing the calculation of the contact length.

3.4.1 Setting of the roll gap

To set the roll gap of CSIRO's laboratory-scale TRC machine, a spacer block is placed on the roll bearing blocks. The restraining bolts are tightened until the top bearing block meets the spacer block.

3.4.2 Setting the roll speed

The roll speed of the TRC device is controlled by a SEW Eurodrive variable speed drive (VSD) and a cone drive mechanical variable speed drive. The rolls are protected by a slipping clutch plate that prevents excess load being applied to the roll shells. The roll speed is coarsely set to the desired speed through the mechanical cone drive with fine adjustments to the roll speed set through the VSD.

3.4.3 Nozzle design

Because of the small widths, a simple letterbox style of nozzle has been chosen. The only constraints on this type of nozzle are that the side plates and nozzle opening must be of such size that they form a tight fit with the rotating rolls. For larger strip widths more care is required to design a nozzle that will deliver melt of equal temperature and flow rate across the width of the strip.

3.4.4 Setting of the contact length

The contact length is controlled by the placement of the ceramic melt delivery nozzle within the roll bite. With the known roll gap and the total nozzle thickness, the required contact length where the nozzle touched both the top and bottom roll can be calculated using Eqns 1-3. The ceramic melt delivery nozzle has to touch both the top and bottom roll of the TRC unit in order to prevent backflow of the melt prior to solidification.

$$Half\ distance = \frac{(2\ x\ Nozzle\ tip\ thickness + Nozzle\ gap) - Roll\ Gap}{2} \quad (1)$$

$$cos\alpha = \frac{Roll\ radius - Half\ distance}{Roll\ radius} \quad (2)$$

$$contact\ length = sin\alpha\ \times\ Roll\ radius \quad (3)$$

The placement of the nozzle is controlled by the casting table. The nozzle and tundish are bolted to the casting table. The casting table can be adjusted in both horizontal and vertical directions.

3.4.5 Pre-casting preparation

Once the nozzle and tundish assembly has been manufactured and placed into the roll gap, the protective atmosphere and preheating system needs to be attached to the melt delivery system. For the melt furnace, the protective atmosphere connected to the furnace consists of a mix of 0.3% SF_6 in nitrogen. For the melt delivery tube and tundish, the protective atmosphere is a high purity argon. To pre-heat the tundish and Nozzle sections of the melt delivery system, a high flow hot air gun is used to pass air pre-heated to 873 K through the tundish and nozzle. The melt delivery tube is preheated using an electrical resistance tube heater controlled by a Eurotherm controller. During pre-heat of the melt delivery system, the rolls of the caster should be turned on in order to prevent hot spots developing on the rolls.

3.4.6 Start-up procedure

1. Turn on gas flow to the melt delivery system protective atmosphere system.
2. Remove the hot air gun from rear of tundish.
3. Close the bleed valve on melting furnace.
4. Pressurise the melting furnace with argon to eject melt into tundish.
5. Raise the melt height to desired height for casting.
6. Roll speed may need to be adjusted to produce good quality strip.

The $Mg_{60}Cu_{29}Gd_{11}$ alloy is a candidate for TRC due to its relatively high GFA, with a critical thickness of ~8 mm when cast in air [21]. The alloy is prepared from commercially pure ingots melted in an electrical resistance furnace under a protective atmosphere of 0.3% SF_6 in nitrogen. The alloy is cast into sheet using a horizontal TRC facility at CSIRO. This facility consists of an electrical resistance furnace that can be pressurised for melt ejection, a tundish, a nozzle and a pair of water cooled Cu-Be rolls. After the holding furnace is stabilised at the desired casting temperature, the melt is ejected through a transfer tube, into the tundish by applying an additional gas pressure to the melt surface. From the tundish, the metal flows through the nozzle into the roll gap of the TRC unit. The amorphous sheet produced at 3, 2 and 1 mm in thickness. The width of the sheet is 50 mm, with the cast length being limited to two metres by the current furnace capacity. Different roll speeds and contact lengths will be trialled to study the effect of casting conditions on the production window for amorphous sheet. The casting temperature of the alloy is 953 K.

3.5 ISOTHERMAL ROLLING

Rolling of the BMG strip is undertaken to determine whether the rolling of the amorphous strips is feasible. The samples are heated in an air circulating furnace, monitored with a K-type thermocouple, and when the desired rolling temperature is reached the samples are then transferred to the rolling mill. In order to prevent quenching of the work piece by the rolls, the roll surface temperature is raised to the same temperature as the work piece, i.e. isothermal rolling. The heating method employed to raise the roll surface temperature is via an electrical resistance heating cartridge inserted into the core of the roll. The roll surfaces were coated with graphite to lubricate the rolling process minimising friction while still allowing heat transfer from the roll to the work piece. This system consists of a heating element in the centre of the rolls controlled through a Shimaden proportional-integral-derivative (PID) controller, with the control thermocouple being a contact thermocouple on the roll surface. The temperature of the roll surface can be controlled to ±1 K with a maximum temperature of 473 K, Figure 19.

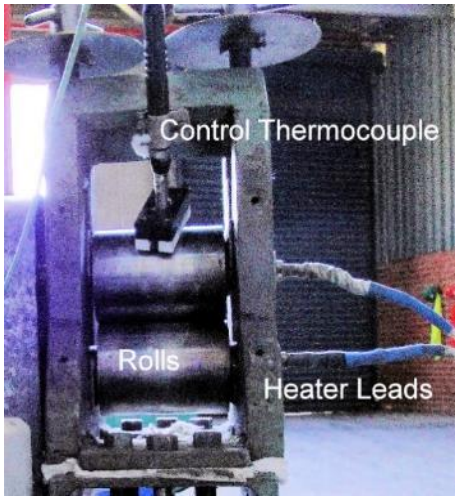

Figure 19 Rolling mill with heated rolls. Electrical resistance expanding cartridge heaters inserted into roll core. Electrical connection through a mercury joint to allow rotating electrical confection.

3.6 PRODUCTION OF LAMINATES

Prior to roll bonding of the laminate material, sandwich pre-forms are made by alternating aluminium and BMG layers, with the layers being held together with aluminium fasteners prior to bonding in order to stop twisting and movement of the individual layers. The laminate pre-forms are heated in an air circulating furnace, monitored with a K-type thermocouple, and when the desired rolling temperature is reached the samples are then transferred to the rolling mill. In order to prevent quenching of the work piece by the rolls isothermal rolling is employed, using the rolling mill shown in Figure 19. Roll bonding of the metallic glass to the crystalline material is under taken in order to form laminate structures. For successful bonding, the surfaces of both materials are required to be mechanically cleaned thoroughly prior to rolling in order to remove any surface contamination. Isothermal rolling within the SCLR of the metallic glass being bonded needs to be conducted in order to prevent fracture of the metallic glass layers.

3.7 MECHANICAL TESTING

3.7.1 Overloaded Vickers hardness testing

A plate of $Mg_{60}Cu_{29}Gd_{11}$ bulk metallic glass plate is polished with diamond compound lapping pads to a 1 μm polish. The glass is then indented using a Vickers hardness indenter with a 10 kg load. The lengths of the cracks are measured with point A being the centre of the indent and point B being the tip of the crack. Indents are spaced at least 4x the width of the indent plus radiating cracks.

3.7.2 Lap shear testing

Lap shear tests are preformed to rank the bond strength between aluminium and glass layers. In this test two crystalline Al plates are bonded with a metallic glass interlayer, processed as described above. The bond size for these tests is 25 mm x 75 mm. To perform the lap shear tests an Instron universal testing machine fitted with a 5000 N load cell is used. During testing a cross head speed of 1 cm/min is used. There are three failure modes that can occur during this test:

1) The bond between the metal and glass could fail at the interface.
2) The metal strip could yield.
3) The metallic glass layer may fracture.

In conjunction with the load value that causes the bond to break, the failure mechanism also is examined. A schematic of the lap shear test is shown in Figure 20.

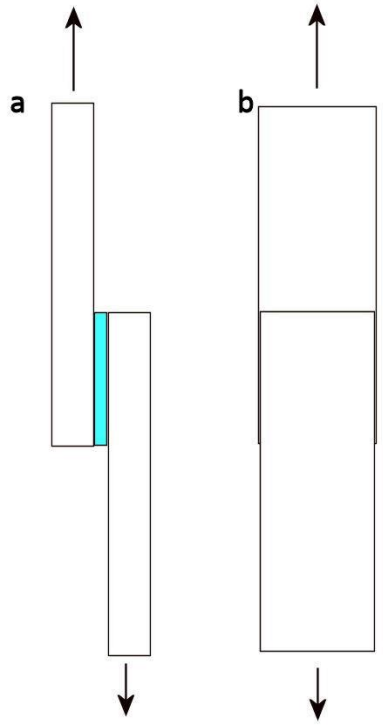

Figure 20 Schematic diagrams showing lap shear test. Arrows show direction of force during testing. White layers are aluminium and the blue layer is bulk metallic glass. (a) Side view showing the join between aluminium and BMG layer. (b) Front on view showing alignment of the two aluminium layers.

3.7.3 Three-point bend testing

Three-point bend tests are conducted to measure the flexural strength of the laminate samples. Testing is done on an Instron universal testing machine with a cross-head speed of 0.5 $mm.min^{-1}$. A 5000 N load cell is used to measure the load on the samples.

An ASTM standard D790 rig is used to conduct the tests. The test specimens for the laminates made from BMG strip are 2 mm thick 5 mm wide and 40 mm long, the span of the test is 30 mm. The samples for laminates made with melt spun ribbon measured 1 mm thick 10 mm wide and 40 mm long, the span of the test is 30 mm.

3.7.4 Charpy impact testing

Charpy impact tests area carried out using samples that measured 10 mm x 2 mm x 50 mm. A 900 g hammer weight is used for the impact test. Un-notched samples are used for testing. Impact testing is carried out on the roll bonded laminates using un-notched samples of non standard size due to the size limitations of the laminate test pieces produced. All samples produced have an aluminium outer layers, so a 3-layer laminate contains two aluminium layers and one BMG layer, a 5-layer laminate has three Al layers interspersed by two BMG layers and so forth.

3.8 MICROSTRUCTURE ANALYSIS

3.8.1 Differential thermal analysis

Differential thermal analysis (DTA) is conducted with a Setaram Setsys Evolution thermal Analyzer. Measurements are carried out with a Type B thermocouple and in 100 µl volume alumina crucibles using α-alumina as the reference material, analysing ~30mg of sample under a N_2 atmosphere.

3.8.2 X-ray diffraction

The XRD is carried out using a Bruker D8 Advance X-ray Diffractometer operating with CuK_α radiation (40 kV, 40 mA) and fitted with graphite monochromators. When testing plate samples, the test pieces are polished using diamond impregnated lapping pads to a 1 µm finish. On the occasions that powder XRD is used, the samples are hand ground using an agate mortar and pestle.

3.8.3 In-situ X-ray diffraction

Variable temperature XRD experiments are performed using an INEL diffractometer, which incorporates a CPS120 position sensitive detector allowing for simultaneous collection of up to 120° 2θ of diffraction data. The Co tube is operated at 40 kV and 35 mA. An Anton Paar model HTK 10 high temperature chamber, employing a platinum resistance strip heater inside it, is positioned on the instrument. The sample is placed into a sample well, measuring approximately 20 × 7 × 0.2 mm, on the platinum heater. The sample is heated at a rate of 10 K min^{-1} from 298 to 453 K, and held at this temperature for ~2 hr. The temperature is measured by a Pt/PtRh10% thermocouple connected to the underside of the platinum strip. XRD datasets are collected, for a period of 1 min, throughout both the heating and the isothermal stages. The data is collected in an asymmetrical diffraction geometry with an incident beam angle of 10°.

3.8.4 X-Ray absorption fine structure

To measure the atomic short-range order of the as-cast and rolled BMGs, XAFS measurements are carried out at the XAS beamline 12-ID of the Australian Synchrotron. The XAS beamline has a wiggler source and a cryogenically-cooled Si (111) monochromators, which is used for the experiment at the Cu *K*-edge (8.98 keV). The monochromatic beam is focused vertically and horizontally using a Rh coated bent toroidal mirror, whilst a set of high precision slits in front of the cryogenic (15 K) sample chamber are used to achieve the desired beam spot size on the sample. Samples for XAFS measurements are prepared by ball milling the BMG in to a fine powder. 15 mg of this fine powder is then further ball milled with ~ 100 mg of BN powder. The mixed, powdered samples are then pressed in to a 6 mm disc using a hydraulic press. XAFS measurements are carried out at 18 K to minimise any contributions from thermal disorder. Data is analysed using ARTEMIS, part of the IFEFFIT computer software [87, 88]. The XAFS data is Fourier transformed over a k-range of 3.2 – 9.8 $Å^{-1}$ to produce a non-phase corrected radial distribution around the Cu atoms.

3.8.5 Scanning electron microscopy

Scanning electron microscopy (SEM) will be be used to characterise the samples. Secondary electron imaging is used to study the fracture surfaces of impact, lap shear and three point bend test pieces. Back-scattered electron (BSE) imaging is used to study laminate structures as the large difference in atomic weight of the metallic and glass sections of the laminate provide excellent contrast for studying these structures. Energy dispersive X-ray analysis is used to identify particles that are found within an amorphous matrix.

Sample preparation for polished samples examined via SEM is done by mounting the sample in conductive mounting media. The samples are then ground using silicon carbide paper starting with 180 grit and then progressing through successively finer grades until 4000 grit paper. The samples are then polished using diamond polishing pads; 3 μm then 1 μm. The final polish is conducted using an OPS solution on a neoprene pad. Samples are ultrasonically cleaned in ethanol between each polishing stage.

SEM is conducted on a FEI Quanta 400 Field Emission ESEM with a working distance of 10 mm. For examination of fracture surfaces, the samples are cleaned using ultrasonic cleaning in ethanol solution to remove oil and other contaminates from the surface. The samples are then mounted on a stub with carbon tape and ProSciTech conductive silver liquid to ensure a conductive join between the sample and stage.

3.8.6 Transmission electron microscopy

Samples for transmission electron microscopy (TEM) analysis are prepared using the wedge preparation technique. Using this method, a sample is polished using a Model 590 tripod polisher form South Bay Technologies. Samples are polished to 60 μm thick using a parallel setting on the tripod polisher this is done on diamond impregnated lapping pads, starting at 3 μm and progressing to 1 μm particle size. Once the sample reaches 60 μm in thickness, a wedge is introduced into the sample by adjusting one leg of the tripod polisher to be 5 μm shorter than the other two legs. The wedge sample is then attached to a molybdenum ring with the thin edge of the wedge aligned with the diameter of the ring. The sample is then polished via ion milling to electron transparency on a liquid nitrogen cooled stage. A Gatan 691 Precision Ion Polishing System (PIPS) is used with a gun angle of 4° and current of 5 keV for 1 hour. The PIPS guns are then adjusted to a 2^{o} angle and a 2 keV current for a further 30 min polish. The wedge sample preparation technique is chosen as the BMG samples cannot be produced using a 3 mm punch due to the brittle nature of the BMG. Spark discharge machining cannot be used due to the heat generated by this technique, the heat would alter the structure of the glass being examined. Ion milling with an uncooled stage will alter the structure of the samples being examined. Therefore a liquid nitrogen cooled stage is required for sample preparation to eliminate the artefacts that form in samples produced in an uncooled stage.

TEM is used to determine the presence of crystalline particles within the structure of glass samples prior to and post rolling. The majority of the TEM is carried out on a JEOL JEM-2100F FEGTEM (Figure 21a). The elemental mapping system fitted to this microscope is a JEOL 50 mm2 Si(Li) EDX detector with Gatan EDX Digital Micrograph plug-in. Images are taken using a 20 kV acceleration voltage onto a Gatan UltraScan 1000 (2k x 2k) CCD camera.

The high angle annular dark field scanning transmission electron microscopy (HAADF-STEM) images are taken using a double abberation-corrected FEI Titan 3 80-300 FEGTEM (Figure 21b).

Figure 21 (a) JEOL JEM-2100F FEGTEM. (b) Double-corrected FEI Titan 3 80-300 FEGTEM.

4 PRODUCTION OF MG-CU-GD AND MG-CU-Y BMGS

4.1 INTRODUCTION

In this Chapter the establishment of a processing window for the successful production of high quality monolithic glass through various production processes will be described. Three different production processes are used, each one producing a different end product. The three production processes are:

1. Rotocasting: a casting method that uses an induction coil to heat and melt an alloy. When the alloy is molten the crucible is spun and the melt flows through centrifugal force into a copper mould. The crucible is protected by an argon shroud to reduce the oxidation of the melt. This process is used to produce samples up to 50 mm long and with profiles (typically circular or rectangular) that can fit within a 38 mm diameter cross-section. In this work the Rotocasting method is used to produce wedges and bars.
2. Planar flow casting: a casting method that produces ribbons of material that are 20 mm in width and up to 200 µm in thickness. In this process a charge is melted via an induction coil and then allowed to contact a rapidly spinning Cu-Be alloy wheel. The batch size for this production method is 20 grams of $Mg_{60}Cu_{29}Gd_{11}$ alloy.
3. Twin roll casting: a casting method where a melt is delivered into the roll gap of two counter rotating rolls. The melt solidifies on the roll surface and is rolled and cast in one production step. This process can produce material at thicknesses between 1 and 8 mm. For commercial aluminium alloys, sheet can be continuously cast at a width of 2 metres and a thickness of 5 mm using this technique. In this lab-scale work a furnace with a 5 kg capacity of $Mg_{60}Cu_{29}Gd_{11}$ is used.

4.1.1 Rotocasting

Few of the production variables in the Rotocasting process can be monitored or altered. The rotational speed is set and the temperature of the melt prior to casting is not monitored. When setting the heating time a viewing window allows the crucible to be monitored visually. When the charge becomes molten the heating is stopped and the start casting button pressed which drops the induction coil and spins the casting arm for the set amount of time.

4.1.2 Planar flow casting (PFC)

The processing variables, such as slot geometry, metallostatic melt head height and wheel speed, are varied and the resulting effect on ribbon quality is studied. The dominant variable in the production of amorphous ribbon is controlling the flow of metal onto the roll surface. Changing of the roll speed affected the ribbon thickness with slower speeds resulting in thicker ribbon.

4.1.3 Twin roll casting (TRC)

The relationship between alloy properties such as critical thickness, thermal diffusivity, glass transition temperature and crystallisation temperature on the casting process will be explained.

Variables in the casting process such as contact time between the rolls and the melt, the contact length from the mouth of the melt delivery nozzle to the roll bite and the roll bite separation distance are systematically varied to establish the operating window for the process.

With the variation of casting variables, the resultant microstructure of the as-cast sheets are characterised using XRD, SEM and optical microscopy.

The two most common types of casting defect are also characterised and the formation mechanisms of these defects described.

4.2 RESULTS AND DISCUSSION

4.2.1 Identification of glass transition, crystallisation and melting temperature of the alloys

Differential thermal analysis is undertaken to identify the critical temperatures that are required prior to casting. These temperatures are the T_g, T_x and the liquidus temperature (T_L) of the alloys. The T_L of the alloys is required to set the melt temperature in the melting crucible of both the TRC and PFC systems. A superheat of 50 K above the liquidus of the alloy being cast is used in both PFC and TRC. The T_g and T_x temperatures are required to establish the extent of the SCLR for the associated alloy.

The T_g temperature is the inflection point in the DSC curve where the curve deviates from its initial slope due to the mobilisation of atoms within the structure. The T_x temperature is the temperature at which the DSC curve spikes upwards from the normal slope due to the energy being released on the formation of crystals within the amorphous matrix. The values for the two alloys that are initially used in this study are indicated in Figure 22 and are given in Table 3.

Within the SCLR, a BMG can be plastically formed. At temperatures below T_g the BMG is a rigid brittle material, and above T_x the amorphous phase is unstable and will crystallise. The values of T_g and T_x are dependent on the heating rate at which the test is conducted. A lower heating rate will lead to a reduction in the T_g and T_x temperatures. This can be seen by comparing the DSC curve in Figure 23 that is obtained at 10 K·min^{-1}, results in the T_g and T_x temperatures increasing in magnitude by 20 K.

Table 3 Critical temperatures (K) for the alloys investigated, taken from DSC curve in Figure 22 measured at 5 K·min^{-1}.

Alloy	Glass transition, T_g	Crystallisation, T_x	Liquidus, T_L
$Mg_{60}Cu_{29}Gd_{11}$	405	451	720
$Mg_{66}Cu_{25}Y_9$	400	451	748

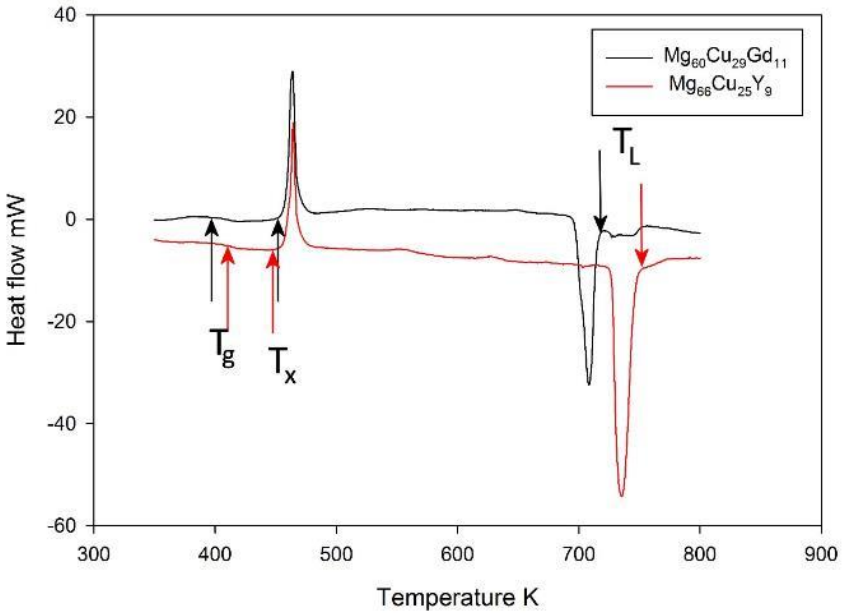

Figure 22 DSC curves for $Mg_{60}Cu_{29}Gd_{11}$ and $Mg_{66}Cu_{25}Y_9$ showing critical temperatures for casting amorphous samples. T_g = glass transition temperature, T_x = the onset of crystallisation temperature, T_L =liquidus temperature. Curves measured at 5 K·min^{-1}.

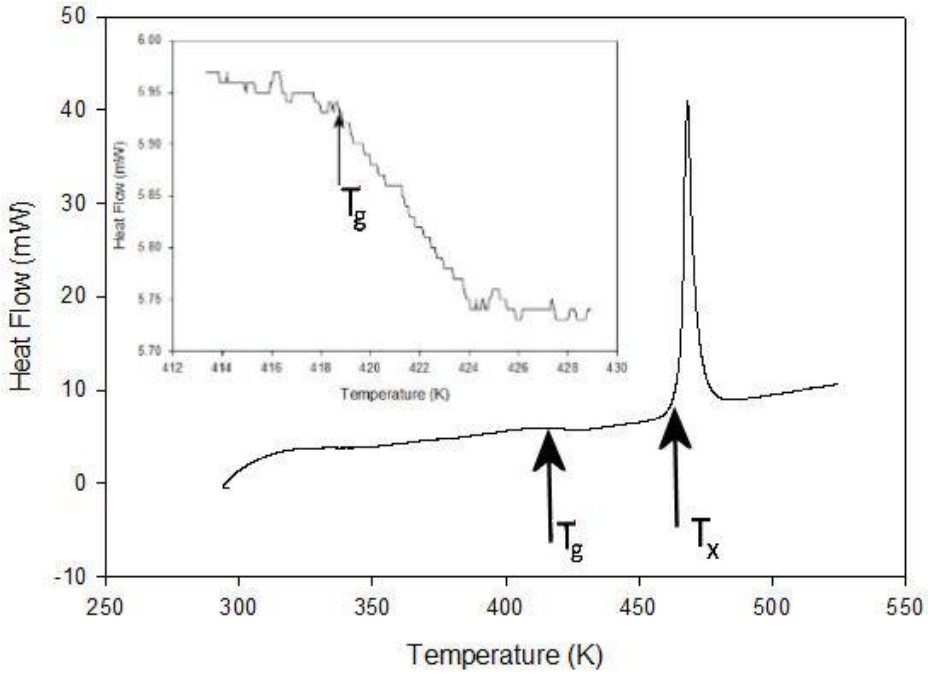

Figure 23 DSC curve of $Mg_{60}Cu_{29}Gd_{11}$ taken at 10 K·min^{-1}, note that T_g and T_x temperatures have increased by 20 K compared with those obtained from the trace obtained at 5 K·min^{-1} in Figure 22.

4.2.2 Thermal diffusivity curves for two Mg-based alloys

Thermal diffusivity values are a measure of how rapidly a material can change temperature, or alternatively, it is a measure of the thermal inertia of a material. The higher the thermal diffusivity the quicker a material will change its temperature. The thermal diffusivity of the two magnesium alloys is measured as a function of temperature and the trends are plotted in Figure 24, with the values listed in Table 4. These values were measured experimentally using laser flash calorimetry.

Thermal diffusivity is related to thermal conductivity, with the specific heat and the density used to calculate the conductivity of a material. As can be seen from Figure 24, the Y containing BMG forming alloy has a higher diffusivity value than the Gd containing alloy. This means that the Y containing alloy will cool faster than the Gd containing alloy under the same conditions. This will therefore result in a reduction in the contact time of the melt with the rolls that is required to cool the Y containing alloy to the targeted exit temperature during TRC.

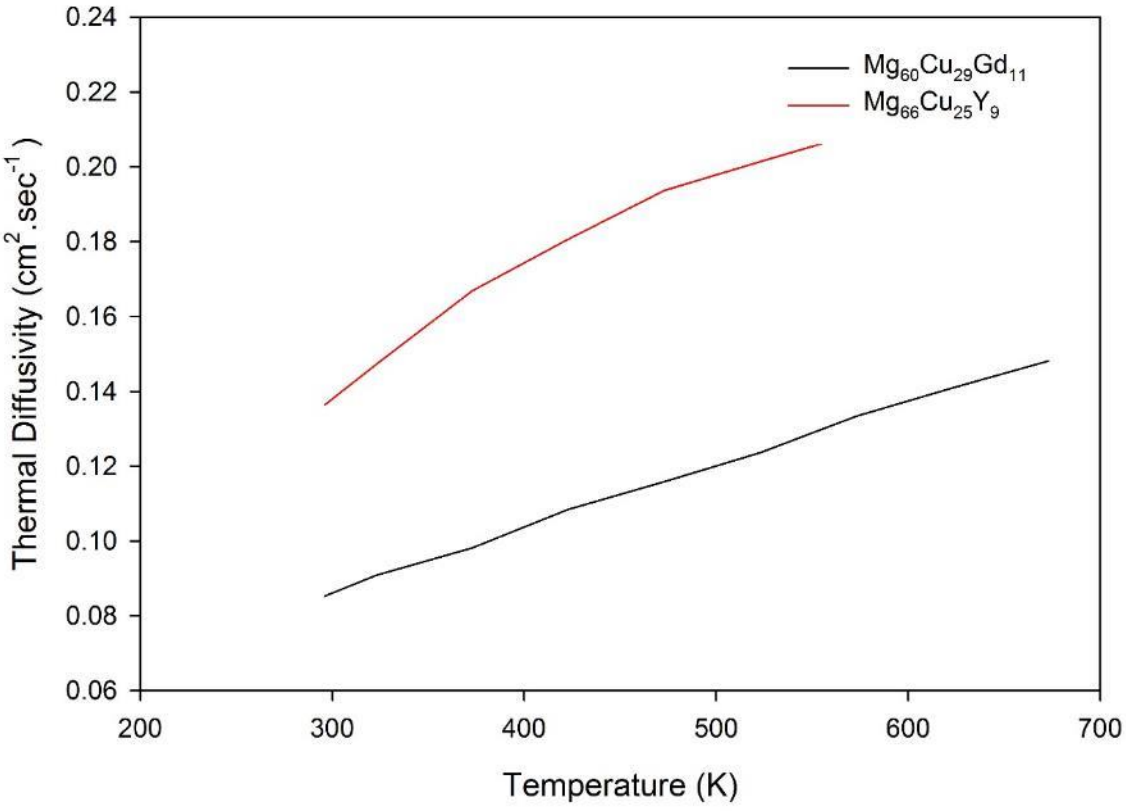

Figure 24 Thermal diffusivity values as a function of temperature for the two different BMGs.

Table 4 Thermal diffusivity values for $Mg_{60}Cu_{29}Gd_{11}$ and $Mg_{66}Cu_{25}Y_9$.

Temperature (K)	**Diffusivity ($cm^2 \cdot s^{-1}$) $Mg_{60}Cu_{29}Gd_{11}$**	**Diffusivity ($cm^2 \cdot s^{-1}$) $Mg_{66}Cu_{25}Y_9$**
298	0.08522	0.13629
323	0.09085	0.14723
373	0.09815	0.16689
423	0.10840	0.18067
473	0.11583	0.19367
523	0.12357	0.20142
573	0.13331	0.20890
623	0.14093	0.21705

4.2.3 Rotocasting

When using low pressure die-casting to produce samples from magnesium-based BMGs, it is found that the critical variables to be controlled are the injection pressure, injection velocity and melt temperature [32]. In the Rotocasting process the injection velocity and the injection pressure are controlled by the rotational velocity of the arm. This rotational velocity of the swing arm is held constant with the current machine. This leaves the melt temperature as a variable that can be controlled to obtain high quality samples. The melt temperature is controlled by setting the power level fed to the induction coil and the length of time that this power is applied.

Once the parameters are set, Rotocasting provides a repeatable method to produce multiple samples of consistent quality under the same casting conditions, see Figure 25.

Figure 25 Rotocast $Mg_{60}Cu_{29}Gd_{11}$ bars.

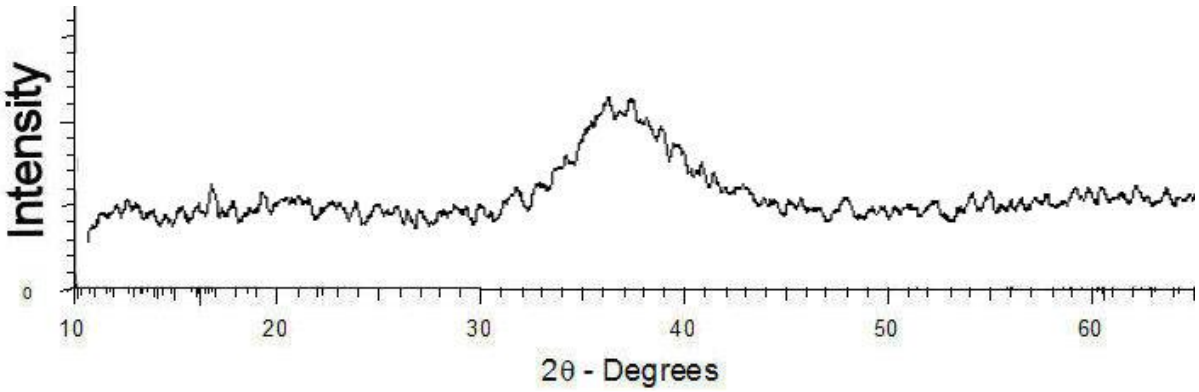

Figure 26 Typical XRD scan of an as-cast 4 mm thick bar.

The as-cast bars are tested via XRD to confirm that the resulting material is amorphous. A typical scan is shown in Figure 26 with a broad peak, typical of an amorphous phase, being present between 30° and 45°. No sharp crystalline peaks are evident.

4.2.4 Planar flow casting

Planar flow casting (PFC) is a production method that ejects a molten metal stream through a nozzle onto a rotating copper wheel, where the melt freezes and a ribbon is spun. A schematic diagram of the process is shown in Figure 27.

The slot in the base of the crucible / nozzle is permanently open and the melt is held within the crucible solely by surface tension. The standard charge size for the $Mg_{60}Cu_{29}Gd_{11}$ alloy is 20 grams. The slot length is held constant for all casting experiments at 25mm. The slot width is varied from 0.5 mm to 1.5 mm, all with a 20 gram charge. A 1 mm slot width is found to be the optimal slot geometry.

For all casting experiments the melt temperature is measured via an optical pyrometer and the casting temperature is held constant at 823 K. During melting the crucible is held within an induction coil. When the required temperature of the melt stabilised, the crucible is lowered to 1 mm from the rotating wheel. At a 1 mm slot width the melt is held within the crucible / nozzle through surface tension and with the application of a 50 kPa over pressure above the melt surface the melt will flow out in an even stream creating ribbon.

When using a 0.5 mm slot width, the slot is prone to blockages and uneven flow across the slot length. These blockages resulted in the formation of holes within the ribbon or failure of the full width of the ribbon to be cast. When the slot size is increased to 1.5 mm then surface tension is no longer sufficient to hold the melt within the crucible. This resulted in the melt exiting the nozzle prior to the nozzle being lowered to the correct position.

Once the slot geometry is set the gap between the wheel and the nozzle is varied. The correct gap distance influences the formation of both the upstream and downstream meniscuses. If the gap is too large then the downstream meniscus will become unstable and the surface of the ribbon will become uneven, and in the extreme case a stable melt pool may not be established resulting in splats or needles being formed during the casting process instead of a continuous ribbon.

Reducing the gap size can cause the upstream meniscus to move further upstream from the slot. This can cause the melt to solidify at a point where it contacts on the bottom of the nozzle and causes casting defects.

For a stable pool to develop the amount of melt entering the pool should be equal to the amount of material exiting the melt pool. The variables that influence the input of melt to the melt pool include the slot geometry and the over pressure applied to the melt. The factors that affect the output from the melt pool are the volume of cast material produced and this is controlled primarily by the wheel speed. The amount of melt that is solidified is a function of the contact time between the melt and the wheel. The controlling variables of the contact time are the wheel speed and the length between the upstream and downstream meniscuses. For this series of experiments the wheel speed is kept constant at 933 $m \cdot s^{-1}$ and the overpressure is held constant at 50 kPa. To vary the amount of material exiting the melt pool the gap size is varied, which will alter the contact length of the melt pool to the wheel.

Three different gap sizes are trialled for producing ribbon, i.e. 0.5 mm, 0.8 mm and 1.5 mm:

Condition 1: 0.5 mm gap, this gap produced unstable casting conditions, pieces of solidified metal adhered to the base of the crucible. This adhered metal causes the melt flow to be unstable and holes appeared in the ribbon or the ribbon would break into sections forming fine needles instead of ribbon.

Condition 2: 0.8 mm gap, this gap provided a stable melt pool with a stable downstream and upstream meniscus, allowing for full width ribbon to be cast.

Condition 3: 1.5 mm gap, this gap produced unstable casting conditions. The melt pool is not stable and in some regions holes appeared in the cast ribbon. In some regions the ribbon broke down to a level that multiple strands are cast.

In order to increase the length of ribbon cast length the charge size is increased to 50 grams. The casting is attempted using the same casting setup for the 20 gram charge, that being 1 mm slot and 0.8 mm gap. In doing this, the metallostatic head that is above the slot meniscus (shown as dotted line in Figure 27) increases such that the pressure applied is unable to be supported and the melt flows from the slot in an uncontrolled manner.

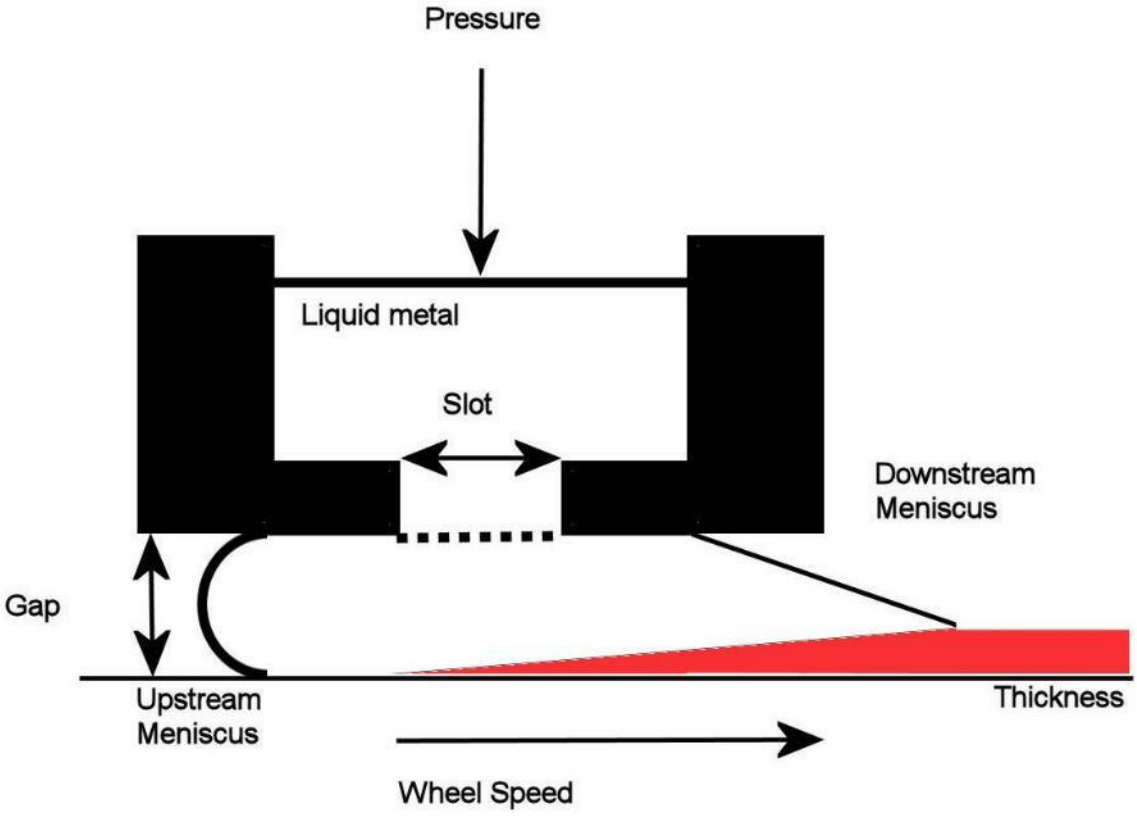

Figure 27 Schematic diagram showing the wheel / melt interaction zone in PFC. As the liquid metal solidifies the solid region forms which is shown in red [89].

From the thickness of a produced casting the cooling rate can be approximated by the formula [90]:

$$\frac{dT}{dt} = \frac{K(T_l - T_g)}{CR^2} \quad (4)$$

Where K is the thermal conductivity, T_L melting point of the alloy, T_g is the glass transition temperature, C is the heat capacity of the alloy and R is the distance from the mould surface in cm. For Mg-Cu-Gd alloys these values are K = 0.378 W/cm $s^{-1}K^{-1}$, C = 2.4 J/cm^3 K^{-1}, T_l = 710 K and T_g = 400 K. If the wheel surface is considered as continuously moving mould then equation 4 can be used to estimate the cooling rate of the ribbon. During planar flow casting the dominant heat flow is into the wheel surface. As the wheel speed increases the ribbon thickness decreases, this reduces the R value in equation 4 which increases the cooling rate at the free surface of the ribbon.

The casting conditions used and the resultant cooling rates based on ribbon thickness are given in Table 5.

Table 5 Effect of wheel speed on ribbon thickness for a slot width of 0.8 mm.

Wheel speed (RPM)	**Linear speed ($m \cdot min^{-1}$)**	**Ribbon thickness (µm)**	**Cooling rate for max. ribbon thickness ($K \cdot s^{-1}$)**
650	606	140-150	210000
1000	933	90-100	480000
1500	1400	70-90	600000
2200	2050	80-90	600000
2800	2600	45-60	1300000

The cooling rates achieved during planar flow casting are such that all alloys that are classed as BMG formers should form 100% amorphous ribbon. An XRD scan taken from a ribbon cast with a wheel speed of 933 $m \cdot s^{-1}$ and a slot width of 0.8 mm is shown in Figure 28, with a broad peak, typical of an amorphous phase, being present between 30° and 45°. No large sharp crystalline peaks are evident.

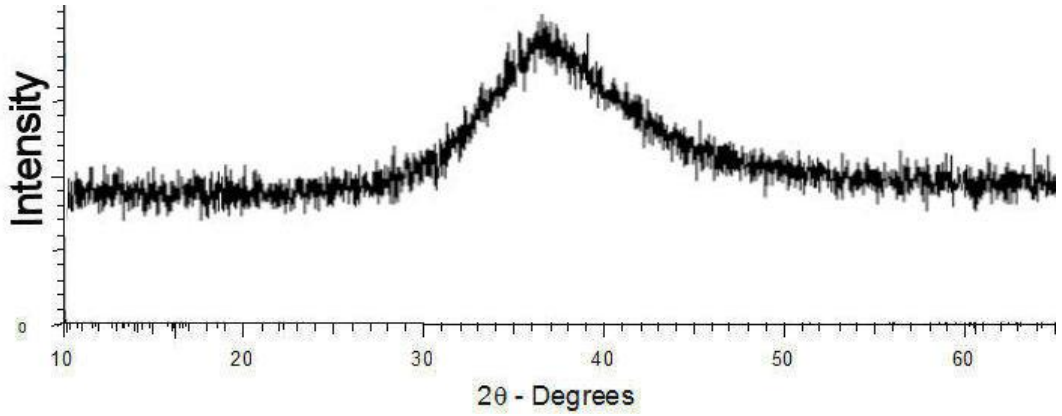

Figure 28 XRD of as-cast ribbon produced from $Mg_{60}Cu_{29}Gd_{11}$ alloy with a roll speed of 1000 RPM and a slot width of 0.8 mm.

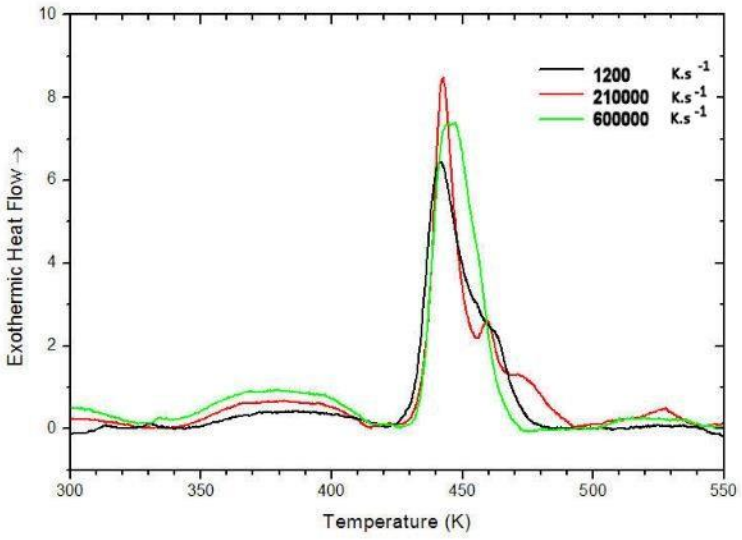

Figure 29 DSC scans of as-cast ribbons of $Mg_{60}Cu_{29}Gd_{11}$, all with a scan rate of 5 K·min^{-1}. All the samples show the same T_g and T_x temperatures. Samples with a cooling rate of 1200 K·s^{-1} were produced via rotocasting. However, the size of the relaxation hump before T_g and the energy associated with the crystallisation peak are different for different cooling rates.

The ribbons cast at three different cooling rates are examined via DSC, Figure 29. In these scans the T_g temperature is measured as 400 K for all three casting conditions and the T_x temperature is 430 K.

Before the T_g temperature there is an exothermic hump, which is caused by the destruction of free volume associated with relaxation processes within the amorphous structure [91]. The hump is larger for the samples cast at higher cooling rates, indicating that the higher cooling rate retains a larger amount of the free volume from the liquid state within the glass.

To further study the effect of cooling rate on the local atomic spacing XAFS are used. This technique provides a measure of the atomic spacing around a particular atom, for this work the Cu atom is selected. The large peak between 2-3 angstroms is the first nearest neighbour peak, Figure 30. As the height of this peak increases this is an indication there are more atoms located at this specific spacing. As the cooling rate applied to the melt increases the amount of order within the system decreases. This is evidenced by the decrease in the height of the first nearest neighbour peak with an increase in cooling rate. Due to the increase in cooling rate there is less time for the atoms to rearrange themselves prior to the melt falling below the T_g temperature where atomic rearrangement is kinetically hindered.

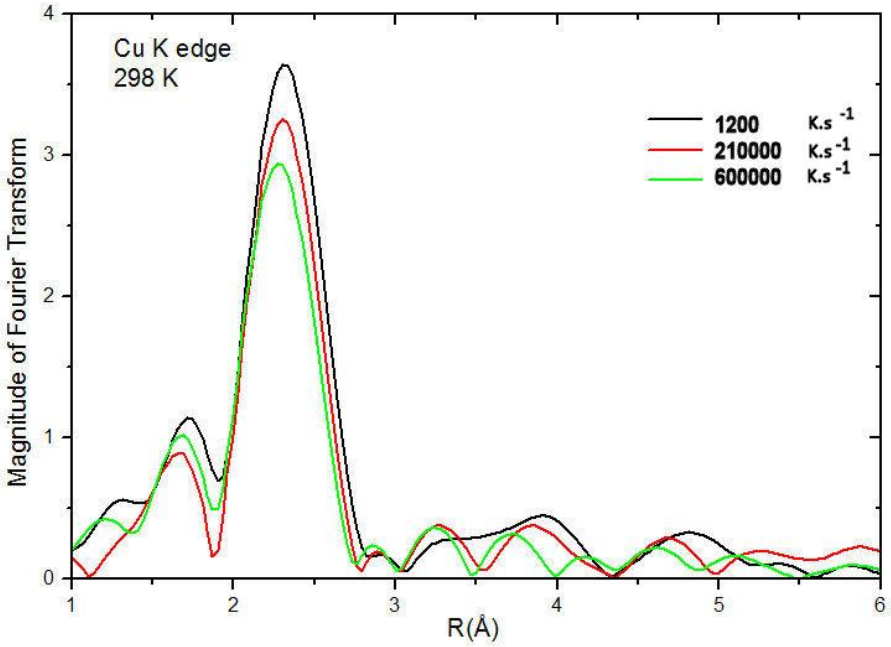

Figure 30 XAFS of BMG as-cast samples $Mg_{60}Cu_{29}Gd_{11}$ produced with three different cooling rates, 1200 $K{\cdot}s^{-1}$ sample 4 mm thick produced via rotocasting, 210000 $K{\cdot}s^{-1}$ 150 μm thick and 600000 $K{\cdot}s^{-1}$ 90 μm thick.

4.2.5 Twin roll casting

4.2.5.1 Design of melt delivery system

The melt delivery system is constructed of refractory fibre ceramics to reduce the heat loss from the melt delivery system. The melt delivery system for a horizontal TRC is required to deliver metal to the roll bite of two counter-rotating rolls in a controlled and consistent manner. Positioning the nozzle within the roll bite controls the point at which the liquid metal first contacts the rolls. The distance from the tip of the nozzle to the nip of the rolls is termed the contact length. The contact length, in combination with the roll speed, controls the amount of cooling that is applied to the melt. The nozzle must be positioned such that the outer edge of the nozzle touches the roll surface. This is to ensure the melt exiting the nozzle opening is prevented from flowing backwards, under the influence of gravity, between the nozzle and the roll surface. Backflow can occur because, although the production technique is generically known as horizontal TRC, the caster is configured such that the direction of casting is inclined at several degrees above the horizontal. If back flow occurs the melt will freeze between the nozzle and the roll and subsequently pull the ceramic nozzle through the roll bite causing catastrophic failure of the casting. Due to the requirement that the clearance between the nozzle and the rolls be minimised, when the contact length of the melt is changed the thickness of the nozzle walls that define the opening also need to be adjusted.

4.2.5.2 Critical thickness of the target alloy

Before proceeding with TRC, wedge castings are made from the targeted alloys using the Rotocaster. The protective argon shroud of the Rotocaster is used to attain an environment close to that which exists within the tundish of the TRC line. From the wedge casting, the critical thickness of the alloy can be readily determined. The critical thickness is the cross-sectional thickness at which the first crystals begin to appear in the microstructure of the wedge. The casting conditions for centrifugal casting give similar cooling rates and atmosphere to those achieved in twin roll casting. From the wedge castings the critical thicknesses of $Mg_{60}Cu_{29}Gd_{11}$ and $Mg_{66}Cu_{25}Y_9$ are measured and found to be 8 mm and 2 mm, respectively. The wedge produced from $Mg_{66}Cu_{25}Y_9$ alloy is shown in Figure 31(a). At the thick end of the wedge the microstructure of the wedge is 100% crystalline with a dendritic structure Figure 31(b). As the wedge reduces in thickness the cooling rate is increased, Figure 31(c) shows the transition area where the amorphous phase is starting to appear at the edge of the casting, but along the centreline of the wedge the structure remains crystalline. Moving further towards the tip of the wedge the cooling rate continues to increase. This increase in cooling rate causes the volume fraction of the amorphous phase to increase. Discrete dendrites in an amorphous matrix can be seen in Figure 31(d). The final image contained in Figure 31(e) displays a 100% amorphous structure, the white dots in this image are rare earth oxides that are formed during casting.

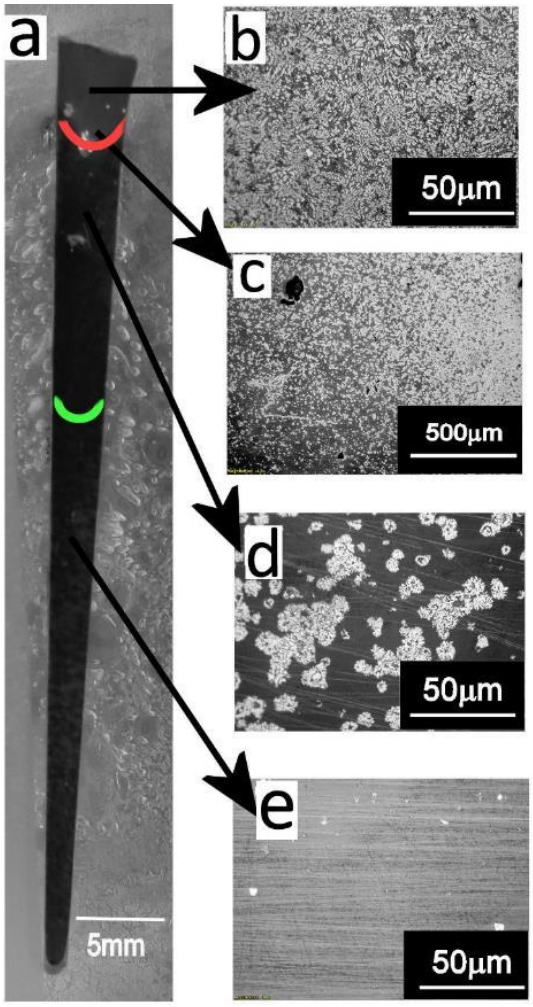

Figure 31 (a) Microstructure of wedge cast $Mg_{66}Cu_{25}Y_9$. As the thickness of the wedge decreases the cooling rate increases and this causes the microstructure to change form 100% crystalline at the widest point of the wedge to 100% amorphous at the midpoint of the wedge. The red line is where the cooling rate enters the transition zone. The green line is where the critical cooling rate lies and below this point the structure is 100% amorphous. (b) Crystalline microstructure (c) and (d) transition zone where a mixture of amorphous and crystalline microstructure produced. (e) Critical cooling rate has been reached and a 100% amorphous structure is produced.

4.2.5.3 *Identification of the critical variables of the casting process*

During a successful casting the rolls are stopped to freeze-off the metal within the roll bite. The optical microscopy image in Figure 32 shows the different microstructure regions and cooling rates that are applied to the melt as it passes through the roll bite. In region 'a', the cross-section is larger than the critical thickness, resulting in a low cooling rate, in this region a crystalline structure is produced. As the cross-sectional thickness reduces the cooling rate increases such that the microstructure changes to a composite amorphous crystalline structure, region 'b'. Region 'c' displays a further reduction in the cross-section thickness and a corresponding increase in the cooling rate and as such the material in this region is amorphous. This cross-sectional view demonstrates that the cooling rate within the roll bite can be below the critical cooling rate of the alloy and amorphous sheet can be produced. Figure 32 is a static representation of the dynamic

system that is occurring within the roll gap, with the melt continually being replenished from the nozzle in region ‘a’ and continually being removed from the system at region ‘c’ when the formed sheet exits the roll bite. The three cooling rate regions that are shown in Figure 32 are the same three regions that are observed in the wedge casting in Figure 31 that being, slow cooling resulting in crystalline microstructure, followed by a transition zone with a mixed microstructure and last a fully amorphous section.

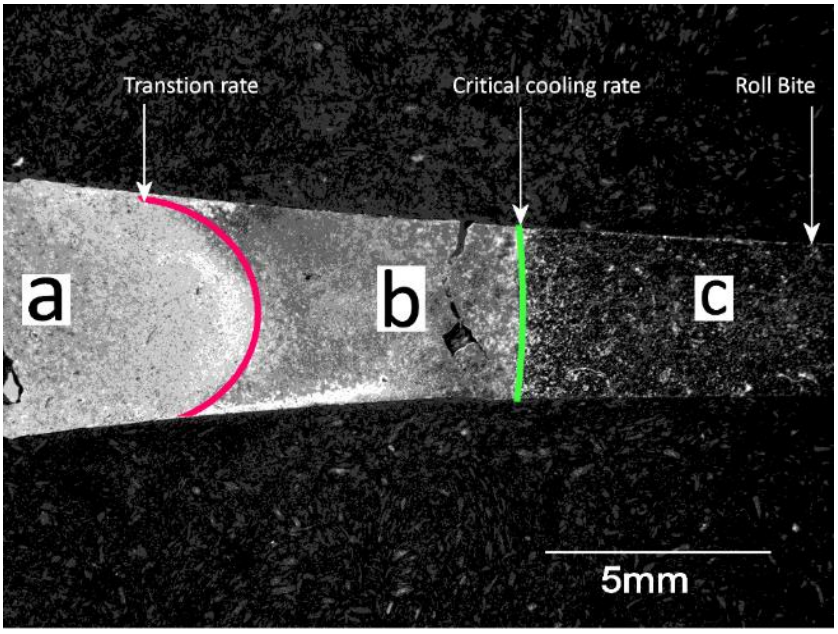

Figure 32 Optical micrograph showing the microstructure from the roll-bite region of a casting after the rolls are stopped suddenly during casting of $Mg_{60}Cu_{29}Gd_{11}$. Transition occurs from crystalline at nozzle opening (a), through composite structure (b), to 100% amorphous near roll bite (c).

The roll gap provides a graduated cooling to the melt as it passes through the roll bite, as well as understanding the different cooling regions, the temperature of the melt moving through the roll bite also effects the quality and structure of the sheet produced. To produce a fully amorphous structure the exit temperature of the sheet needs to be below the temperature of the nose of the CCT diagram (T_{nx}) of the alloy. This temperature is slightly higher but can be approximated by the T_x temperature identified with DSC (at a high heating rate). Below the T_g temperature the alloy is brittle with no ductility. The positions of the T_g, T_x and T_L are shown in Figure 22.

If the maximum amorphous sheet thickness is to be achieved, the T_x isotherm will be located at the roll gap (R), with a thickness that is equal to the critical thickness of the alloy. For a more robust production window, the roll gap Figure 33, of the caster must be set to a value smaller than the critical thickness for glass formation of the alloy under consideration. When the temperature of the melt crosses the T_x isotherm shown in Figure 33 it must be in the cooling rate region that can produce 100% amorphous structure which is labelled as region ‘c’ in Figure 32. Under the correct casting conditions the molten alloy enters the roll nip region and is cooled below the equilibrium liquidus temperature at a cooling rate that is above the critical cooling rate. As this metastable melt passes through the roll bite, avoiding crystallisation, the viscosity gradually increases to produce a continuous fully amorphous sheet.

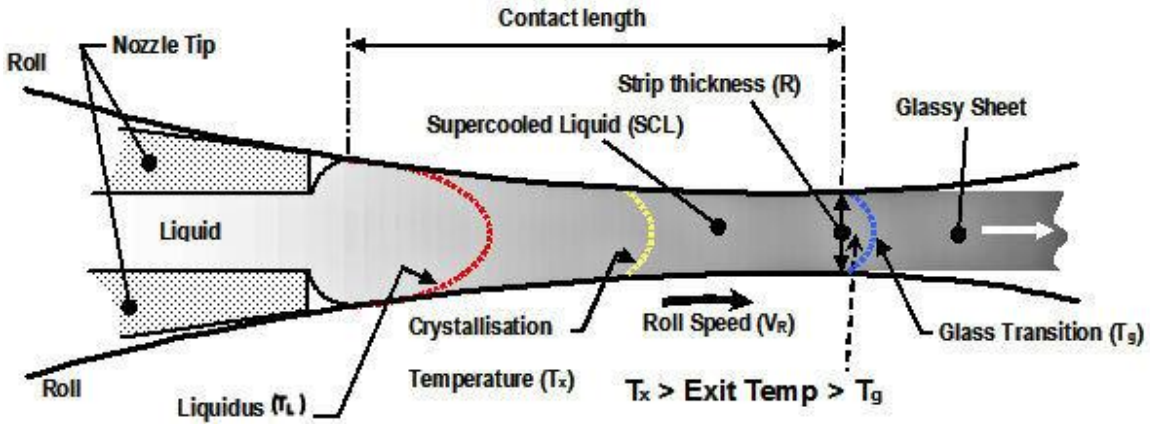

Figure 33 Schematic diagram showing the roll nip configuration to produce amorphous sheet.

By changing the roll speed (V_R), the position of the T_L isotherm, the T_x isotherm and the T_g isotherm within the roll nip region can be controlled, Figure 33. The values of T_L, T_x and T_g are the phase transformation temperatures of the $Mg_{60}Cu_{29}Gd_{11}$ alloy, and they are measured using DSC, Figure 22. Increasing the roll speed causes the isotherms to move towards the roll bite. While, conversely, slowing the roll speed results in the isotherms moving towards the nozzle opening. By altering the position of the liquidus isotherm, the degree of rolling reduction applied to the sheet can be controlled. The increased pressure during the rolling portion, results in good metal-to-metal contact between the cast material and the roll surface. This is where the greatest degree of heat transfer is achieved, as noted in the TRC of conventional crystalline alloys [50].

Under high roll speed conditions, the residence time of contact with the rolls is too short to cool the cast sheet to a temperature below T_x before it exits the caster. As a consequence, on exiting from the caster the sheet air cools slowly through the T_x isotherm, leading to the formation of a crystalline (or partially crystalline) microstructure in the as-cast sheet.

To successfully cast amorphous sheet in continuous lengths the temperature profile must be such that the exit temperature of the sheet is within the SCLR and when the T_x isotherm is reached it should be in an area of the roll gap that is producing a cooling rate that is above the critical cooling rate.

4.2.5.4 Casting window for monolithic glass sheet

Two different magnesium-based BMG forming alloys are cast successfully, i.e. $Mg_{60}Cu_{29}Gd_{11}$ and $Mg_{66}Cu_{25}Y_9$. During TRC, when the imposed cooling rate is sufficient to bypass crystallisation, an amorphous solid will be produced. By controlling the cooling dynamics so the T_{nx} nose on the CCT diagram is bypassed and the alloy exits the roll bite prior to the T_g then a continuous sheet of bulk metallic glass is produced. Figure 34 shows examples of sheet produced by twin roll casting. Three casting runs are shown with each one producing a strip of different thickness.

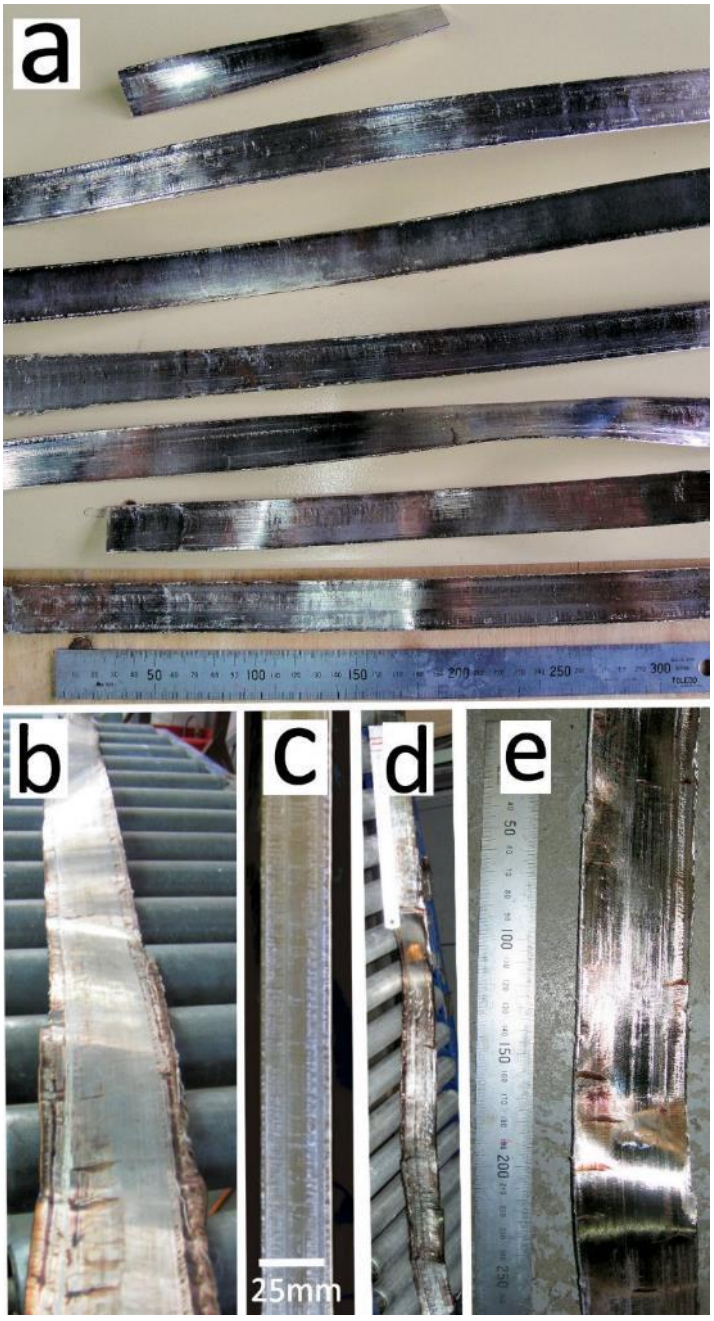

Figure 34 Sheet material produced by TRC from various casting experiments. (a) $Mg_{66}Cu_{25}Y_9$ sheet 1 mm thick produced from one cast run. (b) $Mg_{60}Cu_{29}Gd_{11}$ sheet 2 mm thick 75 mm wide. (c) $Mg_{66}Cu_{25}Y_9$ sheet 1 mm thick surface detail. (d) $Mg_{60}Cu_{29}Gd_{11}$ sheet 2 mm thick 75 mm wide. (e) 3 mm thick $Mg_{60}Cu_{29}Gd_{11}$ sheet 50 mm wide.

For good quality strip to be produced, with regard to dimensional stability and flatness, the exit temperature of the sheet has to be at the lower end of the SCLR. Strip that is produced close to the upper temperature limit of the SCLR is very soft and pliable and thus the as-cast sheet quality is susceptible to damage. Due to the low strength of the strip only a small amount of force is needed to deform and damage the strip, Figure 35 shows two examples of damage to sheets cast with high exit temperatures. In Figure 35(a) shows an edge defect where the strip is squeezed by the gloved hand of the casting operator resulting in the deformation of the strip. In Figure 35(b) the strip is pulled along the run out table and the material deformed and necked down to failure.

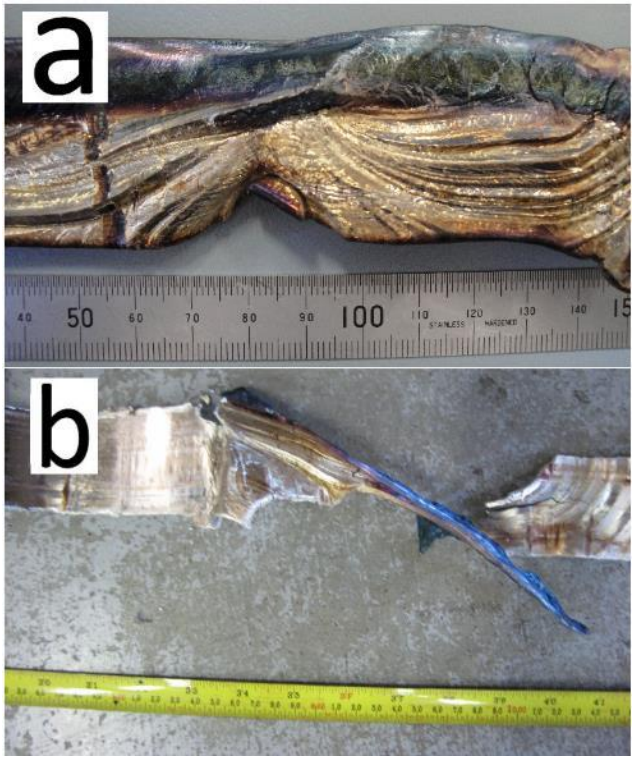

Figure 35 Strip produced from $Mg_{60}Cu_{29}Gd_{11}$ close to the upper limit of the supercooled liquid region is very soft and is easily pliable. (a) Strip that is compressed in the midsection causing flow lines to form on the surface. (b) Has had excessive tension applied and a large amount of necking has occurred before fracture.

Another issue caused by casting with exit temperatures at the higher end of the SCLR is the surface of the strip is susceptible to oxidation. Oxidation of the surface causes the strip to discolour to a blue-purple tarnish, in the current case. The strip in Figure 36 is produced at a high casting speed and the surface has extensive oxidation.

Figure 36 Strip produced from $Mg_{60}Cu_{29}Gd_{11}$ at high casting speed. The strip surface is multicoloured which is an indication of oxidation.

4.2.5.5 *Establishment of casting window for 3 mm thick sheet with constant contact length*

A summary of the casting conditions used for producing 3 mm thick sheet are given in Table 6. Calculating the time the melt is in contact with the rolls, shows that a contact time between 1.1 and 1.2 seconds produces amorphous sheet, when casting the $Mg_{60}Cu_{29}Gd_{11}$ alloy of 3 mm thickness.

Table 6 Production variables for 3 mm thick sheet produced from $Mg_{60}Cu_{29}Gd_{11}$ alloy**.**

Sheet thickness (mm)	**Roll speed ($mm \cdot s^{-1}$)**	**Contact length (mm)**	**Sheet type**	**Contact time (s)**
3	32	30	crystalline	0.94
3	28	30	SCLR on exit high quality strip, 100% glass	1.1
3	25	30	brittle sheet fractured, 100 % glass	1.2
3	18	30	100% crystalline	1.6

The microstructures of the sheet samples, produced with a higher than optimal roll speed and with an optimal roll speed, are examined by optical microscopy. The sheet produced with a higher than optimal roll speed resulted in a fully crystalline microstructure, as shown in Figure 37(a). Slowing the roll speed increased the contact time and allowed the melt to cool to within the SCLR, and produced sheet with a fully amorphous structure, as shown in Figure 37(b).

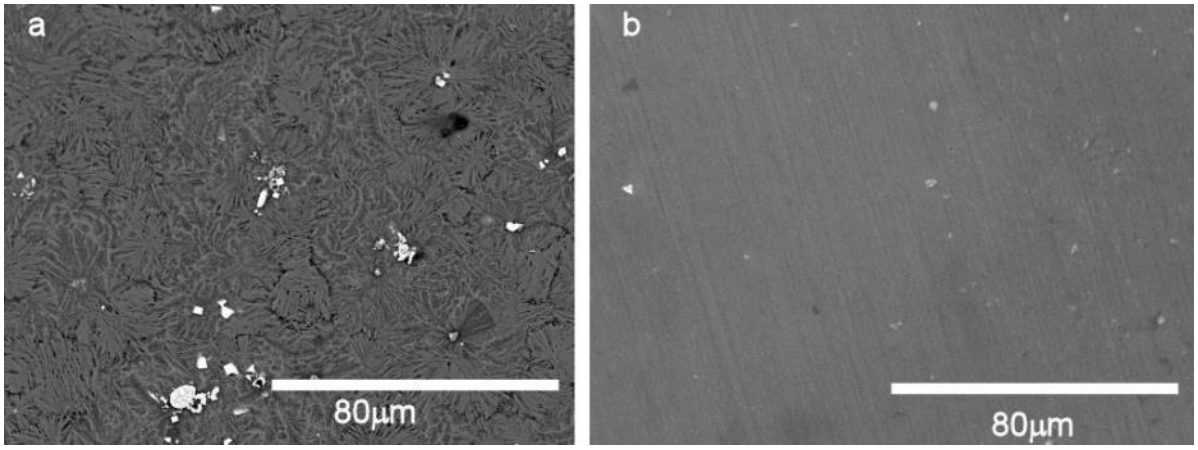

Figure 37 (a) Crystalline microstructure of an as-cast $Mg_{60}Cu_{29}Gd_{11}$ sheet produced with a higher than optimum roll speed of 32 $mm \cdot s^{-1}$ (b) Amorphous structure of an as-cast $Mg_{60}Cu_{29}Gd_{11}$ sheet produced with a roll speed of 28 $mm \cdot s^{-1}$ (the white dots are oxide particles present in the melt that have been entrained in the as-cast amorphous sheet).

To confirm the nature of the as-cast material XRD is used. It is possible to obtain samples from the castings at lower roll speeds as the shards produced could be examined by XRD whereas microscopy samples are unobtainable. The XRD scans confirm the samples cast at high and low roll speed produce a crystalline structure as can be seen in Figure 38. The samples produced with a high and low roll speed show a series of sharp diffraction peaks that indicate the sample is crystalline. The two samples produced in the midrange speed have an amorphous structure, Figure 38, this is confirmed by the diffuse hump in the diffraction pattern that indicates an amorphous structure.

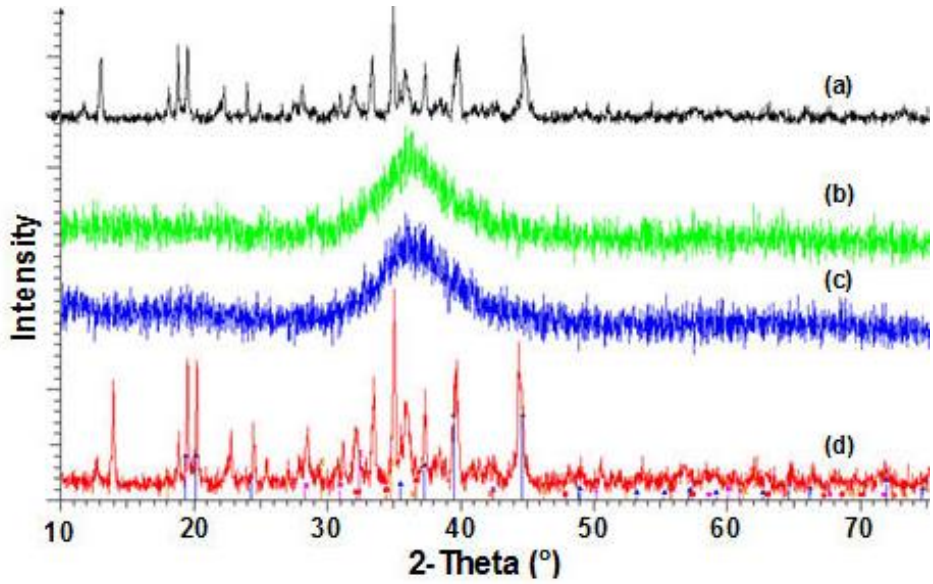

Figure 38 XRD scans showing the amorphous and crystalline nature of the sheet produced at different casting speeds. (a) Sheet produced with 30 mm contact length and 32 mm·s^{-1} roll speed. (b) Sheet produced with 30 mm contact length and 28 mm·s^{-1} roll speed. (c) Sheet produced with 30 mm contact length and 25 mm·s^{-1} roll speed. (d) Sheet produced with 30 mm contact length and 18 mm·s^{-1} roll speed.

During TRC the heat is removed from the melt through the roll surface. This causes the skin of the cast sheet to cool faster than the centre region of the sheet. To produce a 100% amorphous sheet the skin of the sheet as well as the centreline of the sheet must exit the roll bite within the SCLR. If the temperature of the centreline of the sheet is above the T_{nx} temperature of the alloy then a mixed amorphous and crystalline structure will be produced. This change in temperature from surface to centreline in twin roll cast sheet, has been identified as causing composite microstructures in Zr based BMGs [4].

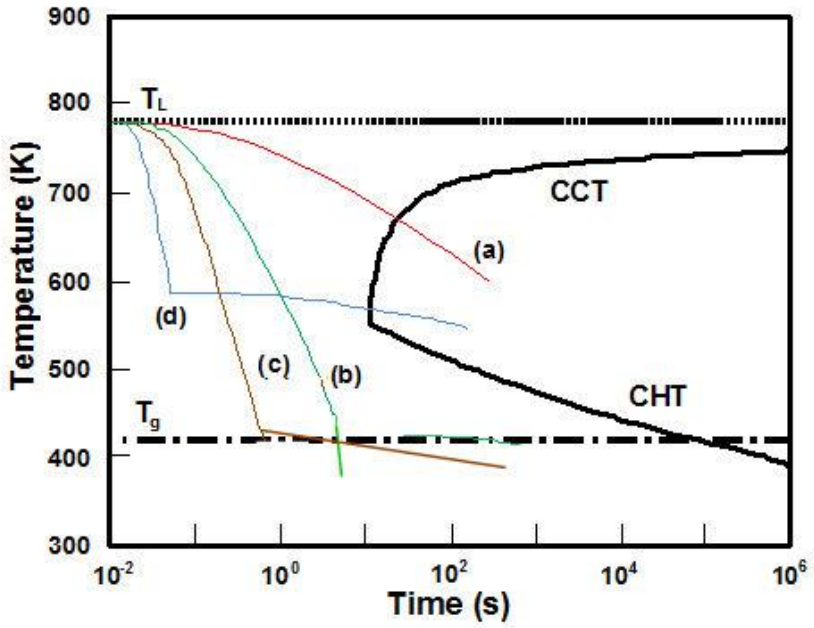

Figure 39 Schematic diagram of continuous cooling and heating transformation (CCT + CHT, based on [92] diagram showing the effect of changes in roll speed on cooling conditions. Roll speed (a) 1.1 $m \cdot min^{-1}$ thickness of the melt as it passes the T_{nx} isotherm is such that the critical cooling rate of the alloy is not achieved and a crystalline structure is formed, (b) 1.5 $m \cdot min^{-1}$ amorphous sheet formed but since it has been cooled to below the T_g temperature it fails in a brittle manner within the roll bite and no continuous strip is formed (c) 1.7 $m \cdot min^{-1}$ melt exits the roll bite within the supercooled liquid region and continuous amorphous sheet produced (d) 1.9 $m \cdot min^{-1}$ as the melt exits the roll bite the T_{nx} temperature has not yet been reached forming crystalline material.

When the roll speed is set at a level far below the optimal condition the resulting cooling of the melt is typified by the curve in Figure 39(a). With a low roll speed the cooling rate of the melt is low due to melt having a longer residence time in the thicker cross-section area of the roll gap, region 'a' in Figure 32. The cooling rate slows further when the strip exits the roll bite and the cooling changes from conduction to the roll surface to convection to the atmosphere. The slower cooling rate due to the larger cross-section results in the nose of the CCT diagram not being bypassed and a crystalline microstructure produced Figure 38(a).

An increase in the roll speed to a level that is still sub optimal will increase the initial cooling rate as the cross-section thickness of the melt will be reduced at a faster rate. This increasing cooling rate will allow the melt to bypass the crystallisation curve but due to the longer contact time the melt will cool to below the T_g temperature this will cause the strip to shatter as below T_g the BMG is brittle. This condition is shown in Figure 39(b) where the rapid cooling continues through the T_g line this condition is used to produce the material in Figure 38(b) which is amorphous.

The optimal casting condition is one that allows the alloy cooling curve to bypass the crystallisation line yet not pass T_g where the alloy becomes brittle. In curve 'c' on Figure 39 the nose of the CCT diagram is bypassed and the alloy has exited the rolls prior to T_g being reached. The rapid change in cooling rate that occurs on the exit of the roll bite is such that the strip which is soft above the T_g temperature can air cool to below T_g temperature without crystallisation occurring. Material that has been produced under this cooling regime is shown in Figure 38(c) to have an amorphous structure.

Increasing the roll speed further will increase the rate of change of the cooling rate Figure 39(d), however, under this condition the melt temperature has not fallen below the nose temperature (T_{nx})

of the CCT diagram. When the cooling rate lowers due to the strip exiting the roll bite the air cool rate is not sufficient to bypass the crystallisation line. This slow cooling at a high temperature allows the crystals to form within the cast sheet. This cooling regime is used to produce the material in Figure 38(d) which shows many crystalline peaks.

When the casting conditions are such the skin of the strip is under the T_{nx} of the CCT diagram Figure 39, but the central core of the strip is above the T_{nx} temperature then a microstructure forms that has an amorphous skin but a mixed (amorphous and crystalline) core, Figure 41. Higher magnification images in Figure 41(b) and 41(c) show dendrites forming within an amorphous matrix.

If the roll speed is not altered in accordance with changes in contact length then the structure of the sheet that is produced will also change. By varying the contact length and keeping roll speed constant, the time in contact with the rolls will change. The amount of time that the alloy is in contact with the roll changes the amount of heat that is removed from the alloy melt before exiting the roll bite. The different structures that are produced with a variance in the contact length at a constant roll speed are given in Table 7. Figure 39 shows the CCT diagram for $Mg_{60}Cu_{29}Gd_{11;}$ under solidification conditions typical of a low initial cooling rate (curve (a) in Figure 39) there is not sufficient time to cool the liquid to below the crystallisation temperature of the alloy. This allows a fully crystalline microstructure to be produced, as shown in Figure 40(a).

By increasing the contact length the alloy melt is cooled at a rate where the formation of crystals can occur but before they can grow to a 100% volume fraction the melt drops below the T_x temperature and crystal growth stops, this produces a mixed microstructure of amorphous and crystalline, as shown in Figure 40(b). The cooling conditions for this mixed microstructure would lay midway between curves (a) and (b) in Figure 39.

Further increasing the contact length increases the cooling time and allows the liquid to cool to within the SCLR. An exit temperature within the supercooled liquid region will produce fully amorphous strip. Figure 40(c) and Figure 39(b).

Table 7 Effect of contact time on microstructure of strip.

Thickness (mm)	**Speed ($mm \cdot s^{-1}$)**	**Contact length (mm)**	**Contact time (s)**	**Microstructure**
3	15	17	1.13	amorphous
3	15	14	0.95	amorphous/crystalline mixture
3	15	13	0.86	crystalline

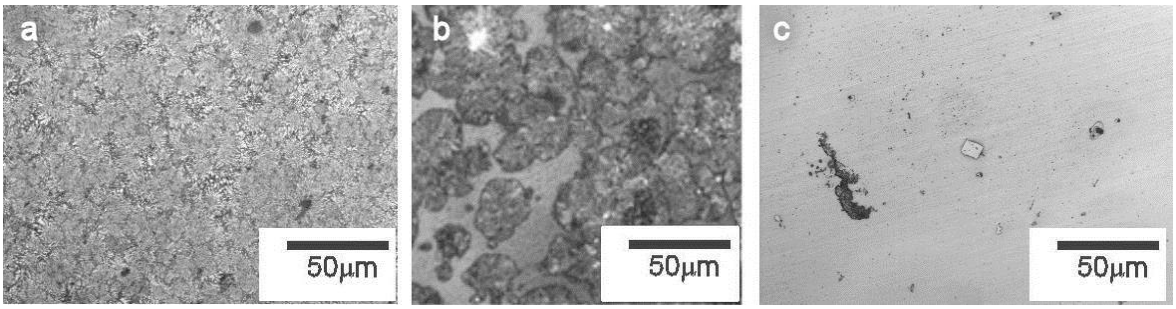

Figure 40 Optical micrographs showing microstructures of (a) crystalline, (b) a mixture of crystalline and amorphous, and (c) fully amorphous.

For thin gauge aluminium sheet, produced by TRC it has been shown that it is possible to produce sheet with a solid skin and a liquid core on exit from the roll bite. This casting condition results in a sheet with a fine surface microstructure and a coarser centreline microstructure [93]. The same temperature gradient across a twin roll cast strip is causing the composite core microstructure shown in Figure 41.

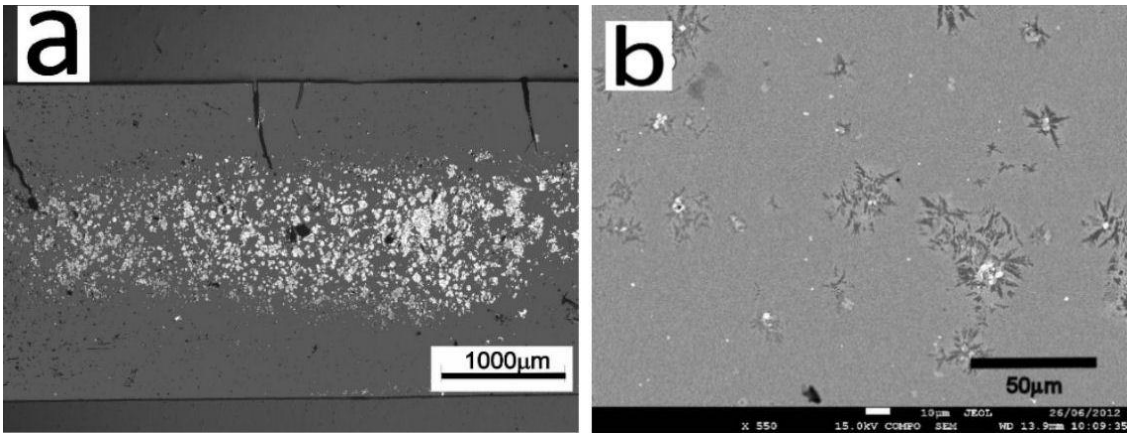

Figure 41 When the skin of the sheet is below the T_{nx} isotherm and the core of the sheet is above the T_x isotherm then the sheet has a core of amorphous and crystalline and a skin that is 100% amorphous. (a) Optical image of amorphous skin. Etching of the sample causes the crystalline particles to be visible in the core. (b) Back scattered electron image of crystalline dendrites in amorphous matrix within the core of the sheet.

4.2.5.6 Production of 3 mm sheet with variance in contact length and roll speed

Positioning of the nozzle within the roll gap is varied to explore the effect on microstructure. Contact lengths of 30, 25, 20 and 17 mm are chosen. Sheet thickness is kept constant at 3 mm. At all four contact lengths it is possible to produce sheet that is amorphous throughout the cross-section of the as-cast sheet. As the contact length increased the roll speed that is required to produce amorphous sheet also increased.

The time the alloy is in contact with the rolls has been calculated and is provided in Table **8**, the contact time for each contact length remains constant. The contact time needed for high quality amorphous sheet to be produced, at all contact lengths, between 1.1 and 1.2 seconds.

Table 8 Casting variables used to produce 3 mm thick $Mg_{60}Cu_{29}Gd_{11}$ amorphous sheet with various contact lengths.

Thickness (mm)	Speed ($mm \cdot s^{-1}$)	Contact length (mm)	Contact time (s)
3	25	30	1.2
3	21.6	25	1.15
3	16.6	20	1.2
3	15	17	1.13

4.2.5.7 Production of amorphous strip of different thicknesses

A decrease in sheet thickness requires the roll speed to produce amorphous sheet to increase, see Table 9 . This is due to the increased surface area to volume ratio of thinner gauge sheet. The relationship between roll speed and sheet thickness is an inverse linear relationship for the region between 3 and 1 mm thickness for alloy $Mg_{60}Cu_{29}Gd_{11}$. This would be expected as the volume of material needed to be cooled decreases the contact time required to cool the liquid also decreases. For this series of experiments all pre-set casting conditions are kept constant except for sheet thickness. The change in thickness results in a change in roll speed required to produce 100% amorphous sheet. Casting of amorphous sheet using $Mg_{66}Cu_{25}Y_9$, is trialled, but because of the small critical thickness of $Mg_{66}Cu_{25}Y_9$, the maximum thickness for 100% amorphous sheet is limited to 1 mm as such a roll speed to thickness relationship could not be developed.

Table 9 Casting variables used to produce $Mg_{60}Cu_{29}Gd_{11}$ and $Mg_{66}Cu_{25}Y_9$ amorphous sheet with various thicknesses.

Alloy	Sheet thickness (mm)	Roll speed ($mm \cdot s^{-1}$)	Contact length (mm)	Contact time (s)
$Mg_{60}Cu_{29}Gd_{11}$	3	17	20	1.2
$Mg_{60}Cu_{29}Gd_{11}$	2	35	20	0.57
$Mg_{60}Cu_{29}Gd_{11}$	1	47	20	0.42
$Mg_{66}Cu_{25}Y_9$	1	70	10	0.14

4.2.5.8 The effect of conductivity and glass forming ability on casting conditions

The percentage difference in contact time for a 1 mm thick sheet of $Mg_{60}Cu_{29}Gd_{11}$ compared with that for $Mg_{66}Cu_{25}Y_9$ is 300%. The thermal diffusivity values for these two alloys show that $Mg_{66}Cu_{25}Y_9$ has a diffusivity value higher than $Mg_{60}Cu_{29}Gd_{11}$ (Figure 24). The thermal diffusivity value is a measure of the thermal inertia of a material the higher the diffusivity value the faster a material can change temperature.

The contact length employed to cast $Mg_{66}Cu_{25}Y_9$ is 10 mm, compared with 20 mm for $Mg_{60}Cu_{29}Gd_{11}$, and the decrease in the contact length requires that the cross-sectional thickness is reduced at the nozzle opening. When the roll gap is set to 1 mm at the roll bite, a contact length of 20 mm gives a thickness at the nozzle opening of 5 mm, whereas at a contact length of 10 mm the cross-sectional thickness of the nozzle opening is 2 mm. A decrease in thickness increases the surface area to volume ratio of the material within the roll bite causing the cooling rate to increase. By reducing the contact length the alloy melt is within a higher cooling rate regime for the entire cooling time.

Combining a higher thermal diffusivity value and a lower cross-sectional thickness during the cooling process explains the decrease in contact time required to cast $Mg_{66}Cu_{25}Y_9$ when compared with $Mg_{60}Cu_{29}Gd_{11}$ at the same thickness.

4.2.6 Surface cracking defects

After the strip has exited the roll bite, surface cracks can appear in the strip due to the application of stress levels above the yield point of the BMG being cast. Cracks form in two ways; the first results when the temperature of the sheet skin falls below T_g (the lower limit of the SCLR) and then undergoes deformation before exiting the roll bite of the casting machine. Second, the sheet is bent or pulled on the run out table of the caster.

The cracking defects do not cause catastrophic failure when some portion of the strip cross-section remains within the SCLR. When a BMG is within the SCLR it is a soft and malleable material which acts to blunt the crack tip and stop the propagation of the crack.

A crack is shown in Figure 42(a), the crack is above the critical crack size for Mg-based metallic glasses yet this crack has not propagated through the entire sheet thickness. Crack propagation stops when the crack reaches the midsection of the sheet. This is due to the crack entering a region that is within the SCLR of the alloy. This soft region blunts the crack tip, as shown in Figure 42(b), stopping catastrophic failure. Without this soft area to stop the crack propagation the cracks would travel through the sheet causing complete fracture. Fatal brittle fracture occurs when the roll speed is such that the T_g isotherm along the centreline of the strip moves to the nozzle side of the roll bite. This condition of brittle failure is observed in casting trials described in Section 4.2.5.5.

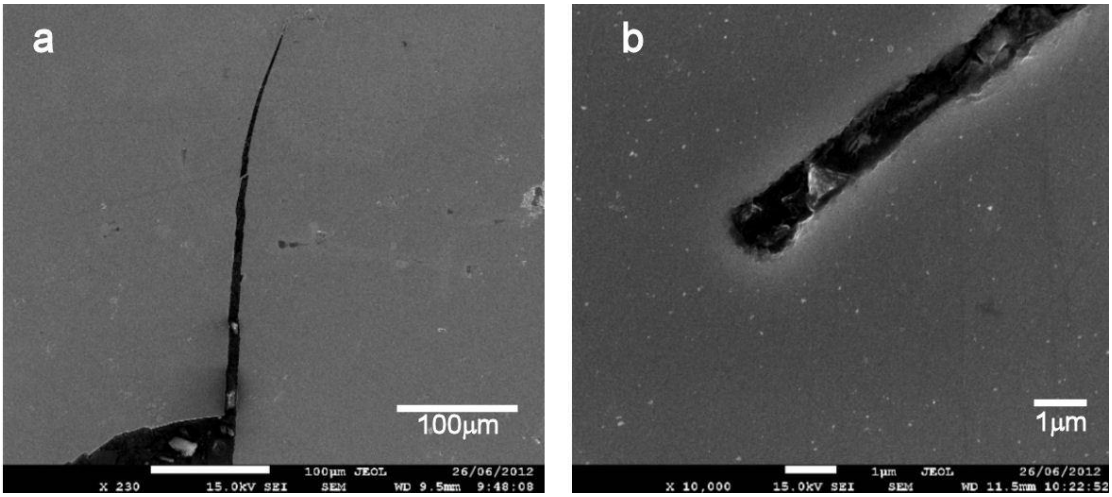

Figure 42 Brittle crack caused during twin roll casting when the strip surface is under the T_g temperature of the alloy $Mg_{60}Cu_{29}Gd_{11}$ and the core of the strip is above the T_g temperature. (a) Crack starting at the strip surface. (b) Higher magnification image of the crack tip shown in a, the rounded point indicates the crack has entered a soft region within the centre of the strip this is stopping the propagation of the crack. The centre region of the sheet is soft due to a higher temperature within the core of the sheet than at the surface due to an increase in distance from the heat sink of the rolls.

If excessive force is applied to the strip and the skin of the sheet is outside the SCLR then this can cause the surface of the sheet to form cracks. The tensile force can come from an applied load pulling the sheet from the roll bite or from tension applied to the strip through bending. In Figure 43 a piece of BMG strip that is unsupported on exit from the roll bite is shown. Because of the lack of support the sheet bent and cooled to below the T_g temperature locking in the curved shape. The outer curve of this sheet has been placed under tension and this is enough to form brittle cracks on the outer radius. A micrograph cross-section of the tensile skin crack is shown in Figure 44. The opening of the crack is large approximately 80 microns and the tip of the defect has a blunt tip indicating the material is soft when deformed.

Another condition that could result in tension being applied to the strip is coiling or directional control pinch rolls, these are not used for this work. However, the use of directional pinch rolls and coiling has been shown to cause defect formation in other alloys [94].

On exit of the roll bite, BMG strip must be handled with care, if regions of the strip remain within the SCLR then the strip can be easily bent and deformed. For brittle BMGs such as the Mg systems used in this work care must also be taken when the strip cools to below the T_g temperature as the lack of ductility can cause shattering to occur easily.

Figure 43 As-cast twin roll cast sheet of $Mg_{60}Cu_{29}Gd_{11.}$ This section is unsupported on the run out table causing a large bend in strip. The tensile stress in the outer surface can cause hot tear defects.

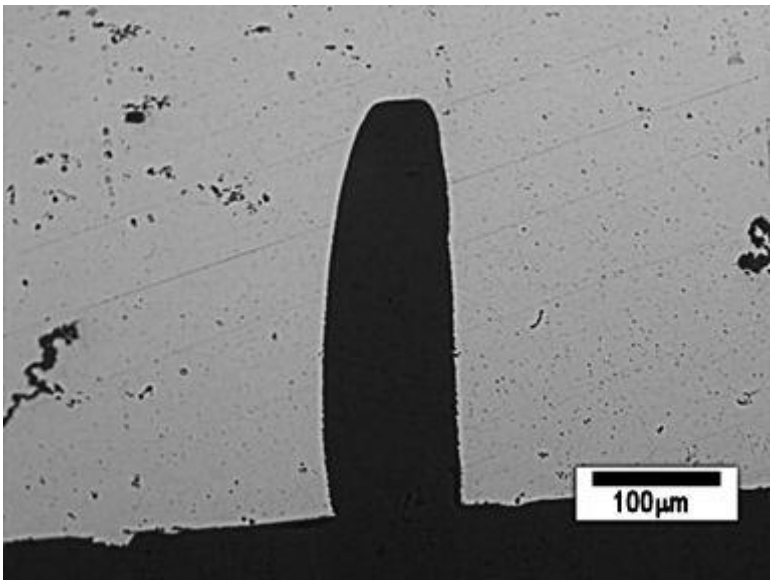

Figure 44 Optical micrograph of outer radius of cast sheet of $Mg_{60}Cu_{29}Gd_{11}$ the black area at the bottom of the image is the outer radius of the curved sheet shown in figure 43. The defect is a hot tear caused by applying tension to the strip while the material is within the supercooled liquid region of the alloy.

4.3 CONCLUSIONS

In order to produce bulk metallic glass various casting methods are trialled. In order to produce amorphous samples the operational parameters of the casting process need to be controlled in order to maintain the required temperature regime and cooling rates. This chapter investigated BMG production via Rotocasting, planar flow casting and twin roll casting. The following conclusions can be made:

1. **The effect of cooling rate on the formation of BMGs is that with an increase in cooling rate the amount of order within the glass reduces**.

   This is due to the reduction in time taken to reduce the temperature of the melt from above T_L to below T_g. X-ray absorption fine structure analysis is used to measure the amount of order within a glasses cast at various cooling rates between 1200 $K \cdot sec^{-1}$ and 6000000 $K \cdot sec^{-1}$ (Figure 30). This analysis shows that as the solidification rate increase the atomic spacing around the copper atom becomes more varied.

2. **Various casting methods can be used to produce amorphous material from $Mg_{60}Cu_{29}Gd_{11}$ alloy.**

   Planar flow casting can be used to produce continuous ribbons in batches of 20 g at 100 μm thick using a wheel speed of 933 $m \cdot min^{-1}$ and a slot width of 0.8 mm.

   Rotocasting can be used to cast parts with a 100% amorphous structure, as long as the casting is below the critical thickness of the alloy being cast.

   Twin Roll casting is explored for producing continuous BMG sheet from two Mg-Cu-RE systems. It is found that twin roll casting can be used to successfully produce continuous sheet of BMG at thicknesses between 1 and 3 mm.

3. **It is found that to produce high quality BMG sheet by TRC the following criteria must be met:**

   - The temperature of the sheet exiting the rolls must be within the SCLR of the alloy.
   - The thickness of the sheet must be below the critical thickness of the alloy being cast when the melt temperature passes the T_x isotherm.
   - The contact time of the melt with the rolls is the rate controlling step. The required contact time can be achieved by varying the contact length and the roll speed as long as criteria 1 and 2 are not violated.

4.4 FUTURE WORK

Transferring the technologies to other BMG systems: In this work the Mg-based systems are selected due to their glass forming ability and their oxygen tolerance. Systems that are based on zirconium and titanium have superior mechanical properties than those of the Mg systems and have GFAs acceptable for TRC. However these systems have a low oxygen tolerance and need to be processed within a vacuum chamber. The ability to produce in-situ BMG composites from alloys such as DH1 ($Zr_{36.6}Ti_{31.4}Nb_7Cu_{5.9}Be_{19}$ [5]) in sheet form would also be another area of research this would require not only the processing in a vacuum chamber but also semi-solid processing.

Increasing the instrumentation on the twin roll casting system: To accurately measure the heat transfer occurring within the roll bite of the twin roll caster, a roll shell with thermocouples embedded just below the roll surface will need to be built. This equipment will allow the study of the casting process to confirm if during the casting of BMGs the same heat transfer profile exists as for that of crystalline metals. Crystalline metals show a reduction in cooling due to shrinkage followed by a sharp increase due to improved contact under load during the twin roll casting process. It will be interesting to see if these same phenomena occur with BMG systems due to the low to non existent shrinkage and the lower loads applied within the supercooled liquid region of the BMG.

5 STRUCTURAL EVOLUTION OF $Mg_{60}Cu_{29}Gd_{11}$ BMG DURING ISOTHERMAL ROLLING

5.1 INTRODUCTION

In this Chapter the results presented detail the rolling procedure developed for a BMG and the structural changes that this rolling imparts to the glass.

The stability range of the amorphous phase for the $Mg_{60}Cu_{29}Gd_{11}$ BMG as a function of time and temperature is determined by XRD on heat treated samples to locate the time at which the first signs of crystal formation occurred at a specific temperature. This data is determined to provide an estimation of the residence time at temperature that can be tolerated without crystallisation being initiated prior to rolling taking place.

The effects of temperature, strain and strain rate on the quality of the rolled product are investigated and processing maps are constructed. The effects of convective, conductive and adiabatic heat transfer are related to the imposed strain and strain rate of the rolling process and these are correlated with the resulting quality of the strip produced. The temperature that is experienced by the work piece during rolling is measured and this is explained through considering the differing contributions of conductive and adiabatic heating.

The effect of rolling on the structure of the glass is investigated by the use of XRD, DSC, TEM and EXAFS. Rolling of the samples within the specified processing window did not result in crystallisation at a level that is detectable by XRD. However, rolling of the samples is observed to have an effect on the T_g, T_x and peak energy of crystallisation values measured by means of DSC.

XAFS spectra are taken around the Cu edge to measure the atomic spacing around the copper atom and give a measure of the degree of order within the structure. XAFS spectra are taken for samples in the as-cast and crystallised states and for samples rolled with a 0.97 and 1.67 s^{-1} rolling strain rate. The XAFS show that by increasing the strain applied to the sample the order within the structure increases.

Imaging of the rolled samples via TEM found no signs of crystallisation for all samples except the sample rolled with a rolling strain of 1.67 and a strain rate of 13.63 s^{-1}. The sample rolled under these conditions had dynamically formed quasicrystals within the amorphous matrix.

In-situ heat treatment XRD experiments are conducted and it is found that applying 1.67 rolling strain at a strain rate of 0.7 or 13.63 s^{-1} resulted in a change of the crystallised phases when compared with the as-cast sample.

Changes to the crystallised phase in samples that are rolled at both high and low strain rates suggest the cause of this change is occurring in both samples and is independent of strain rate. The amount of order within the samples increases with amount of strain added. This change is measured by using EXAFs. In samples rolled at high strain rate the presence of dynamically formed quasicrystals is noted. The formation of quasicrystals from the amorphous structure support the theory that the underlying structure of the $Mg_{60}Cu_{29}Gd_{11}$ BMG is that of icosahedral short range order. When rolling at a high strain rate a temperature spike is measured, this allowed the icosahedra to grow to a size detectable by TEM. Whereas the lack of a temperature spike experienced by the samples rolled at a lower strain rate does not provide sufficient energy to grow quasicrystals from these icosahedra.

5.2 RESULTS AND DISCUSSION

5.2.1 Thermal stability of $Mg_{60}Cu_{29}Gd_{11}$ BMG

The XRD trace from an as-cast sample of $Mg_{60}Cu_{29}Gd_{11}$, with a cross-section of 4 mm x 4 mm, is shown in Figure 45 the presence of a broad peak in the XRD scan is commonly regarded as an indication of the formation of a single amorphous phase. Such a broad single peak is observed between the 2θ diffraction angles of 30° to 45° and therefore the as-cast sample is considered to be fully amorphous. This result is consistent with those found by other researchers working on similar magnesium-based alloy systems [15-17].

To measure the stability of the amorphous phase and to construct a time-temperature-transformation (TTT) diagram, isothermal heat treatments are undertaken at various temperatures. The samples are heat-treated in a circulating hot oil bath and the samples are quenched into water when removed from the oil. The XRD results from the heat treatment trials for the temperatures tested are shown in Figures 45 - 50. For example, after 5 minutes at 450 K (Figure 48, scan (b)) the alloy remains in the amorphous state, as indicated by a single amorphous hump in the XRD scan, which is identical with that for the as-cast sample. However, after 10 minutes at 450 K (scan (c)) the beginning of crystallisation can be seen in the development of diffraction peaks at 37 and 44 degrees. Therefore, a time of 10 minutes is determined as the beginning of crystallisation at 450 K. Similarly, the times for the onset of crystallisation are determined for each annealing temperature and these are contained in Figures 45-49. These times are plotted in Figure 50 to construct a portion of the T-T-T curve, the partial error bars on the curve show the time between the last sample with an amorphous structure and the sample with the first sign of crystallisation.

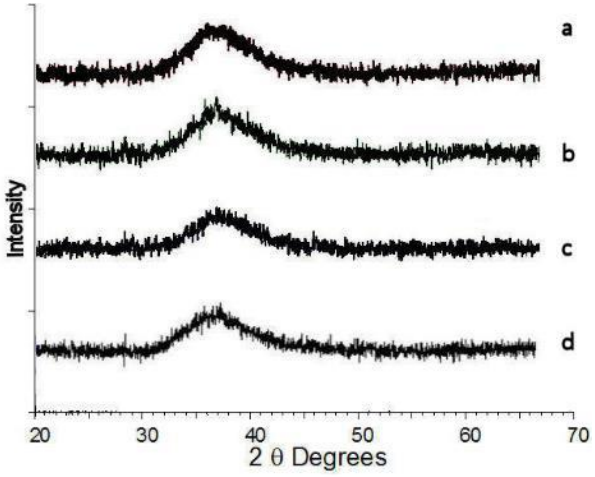

Figure 45 XRD of samples heat treated at 393 K for (a) 1 hour, (b) 16 hours, (c) 24 hours and (d) 48 hours. All samples remain fully amorphous after the heat treatments.

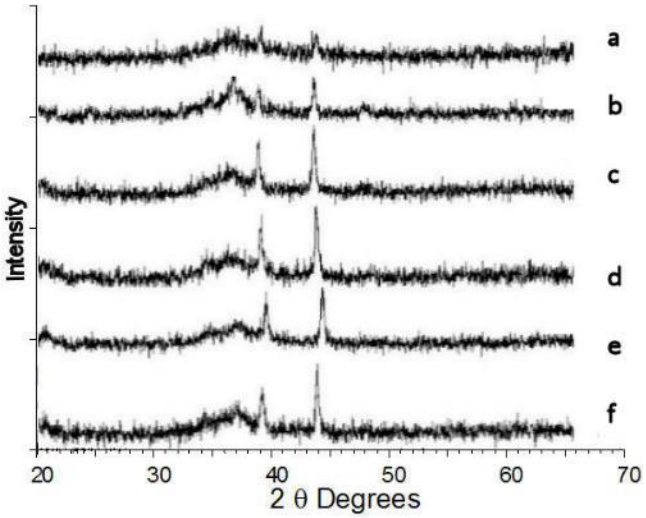

Figure 46 XRD of samples heat treated at 428 K for (a) 1 hour, (b) 2 hours, (c) 4 hours, (d) 8 hours, (e) 16 hours and (f) 24 hours.

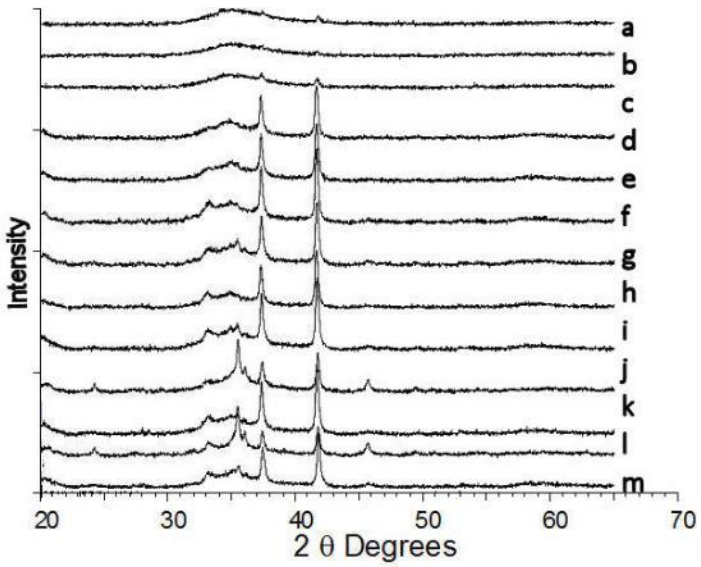

Figure 47 XRD of samples heat treated at 438 K for (a) 10 minutes, (b) 20 minutes, (c) 30 minutes, (d) 40 minutes, (e) 50 minutes, (f) 60 minutes, (g) 120 minutes, (h) 180 minutes, (i) 240 minutes, (j) 300 minutes, (k) 480 minutes, (l) 960 minutes, and (m) 1440 minutes.

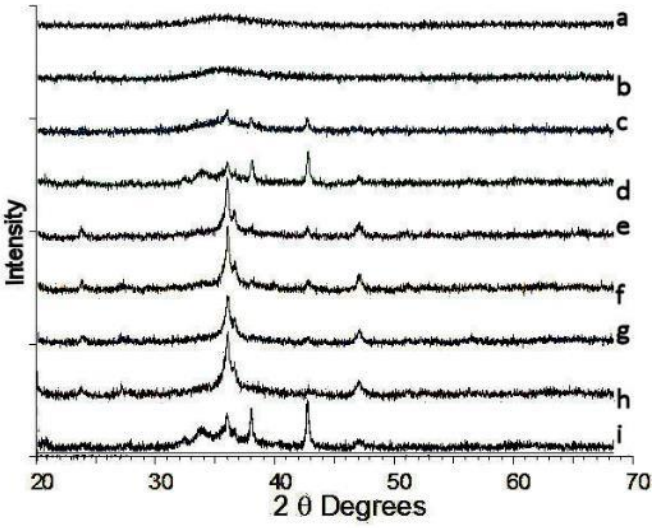

Figure 48 XRD patterns obtained from samples that are heat treated at 450 K for (a) 0 minutes (as-cast), (b) 5 minutes, (c) 10 minutes, (d) 15 minutes, (e) 20 minutes, (f) 30 minutes, (g) 40 minutes, (g) 50 minutes, and (i) 60 minutes.

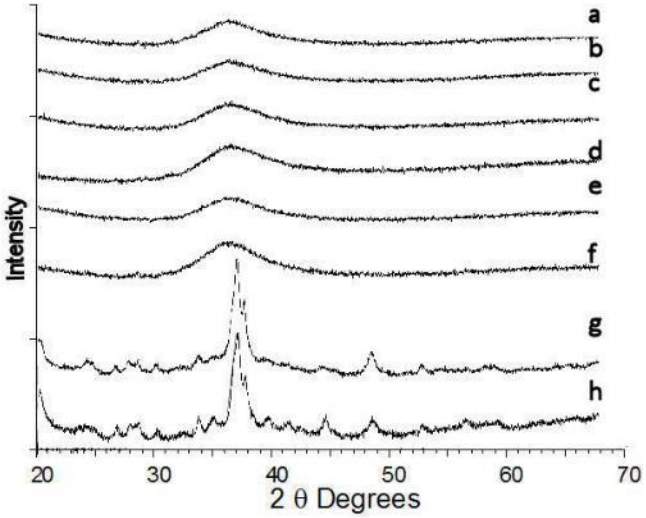

Figure 49 XRD scans obtained from samples heat treated at 473 K for various times. (a) As-cast, (b) 10 seconds, (c) 20 seconds, (d) 30 seconds, (e) 60 seconds, (f) 90 seconds, (g) 120 seconds, and (h) 150 seconds.

Table 10 Time at first indication of crystallisation, as measured by XRD.

Temperature (K)	Time at appearance of first crystallisation peak
393	No peaks after 48 hours
428	1 hour
438	40 minutes
450	10 minutes
473	2 minutes

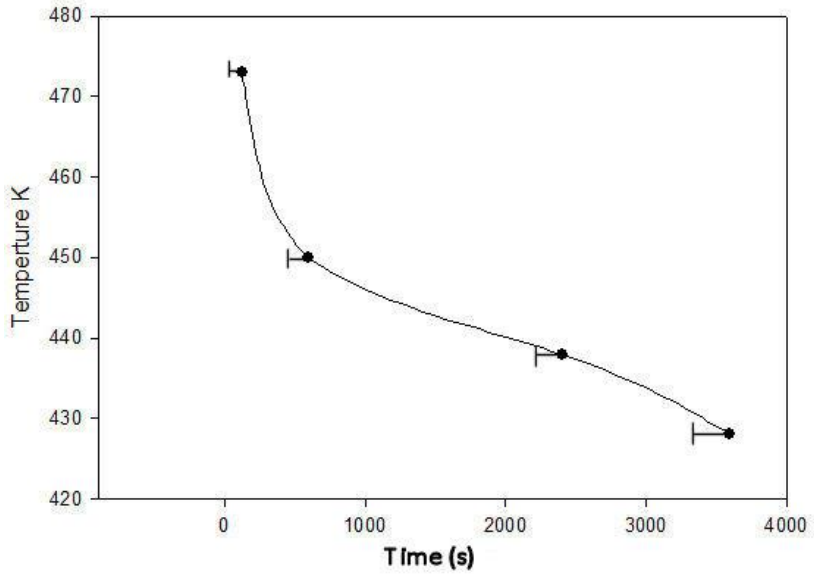

Figure 50 Time required for the onset of crystallisation at temperatures within the supercooled liquid region. Bars on the dots indicate the error in measurement. Error bar indicates the time between sample taken with 100% amorphous structure and the sample with the first sign of crystalline peak.

5.2.2 Processing tables

Isothermal rolling trials are conducted with various combinations of temperature, strain and strain rate. As is shown in chapter 3, Figure 22 the SCLR for $Mg_{60}Cu_{29}Gd_{11}$ lies between 420 K and 470 K and rolling trials are conducted within this range at 10 K intervals. The rolled samples are divided into three categories, which are defined as: a, rolled with no visible defects; b, rolled with surface defects; and c, did not roll— shattered. Examples of the three types of rolled sample are shown in Figure 51, a, deforms plastically with no visible defects or cracks In sample rated as, b, the sample remains in one piece but surface cracks are visible, sample rated c, the sample shatters and fails catastrophically when it passes through the roll bite.

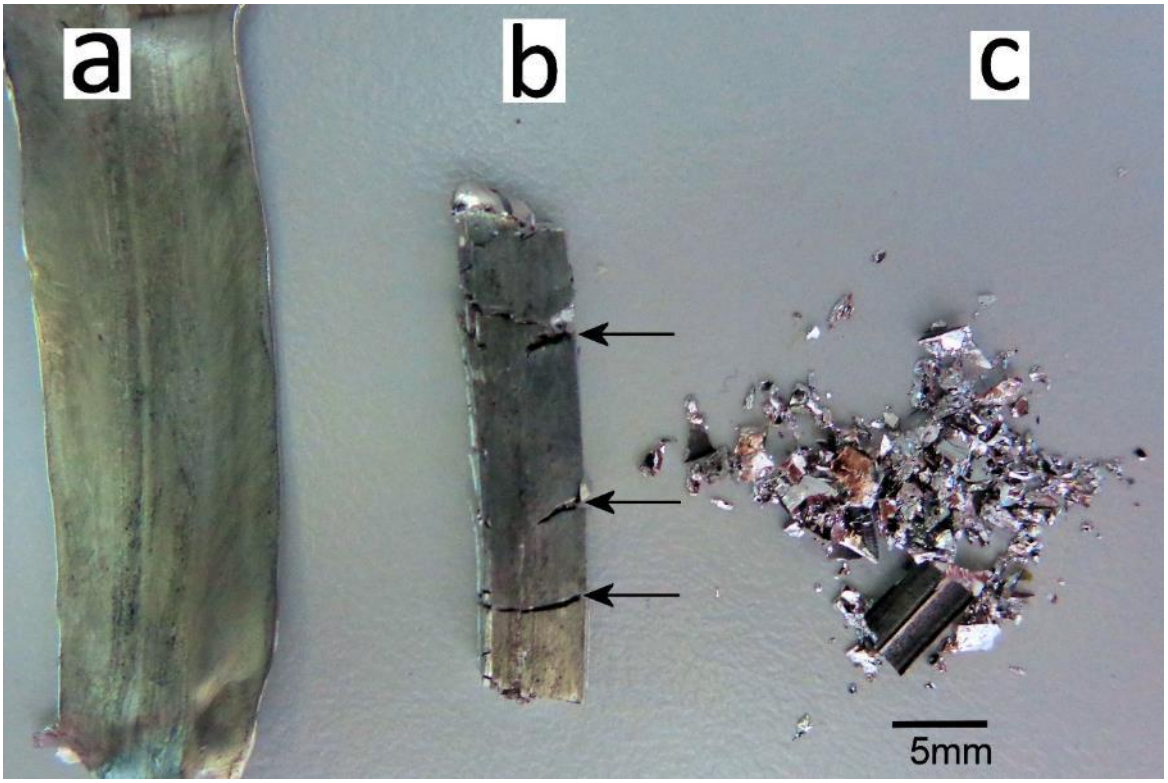

Figure 51 Rolled samples that are used as the standards for rating rolled samples, (a) rolled with no visible defects (463 K, 1.67 strain, 13.63 strain rate), (b) rolled with some surface and edge cracking but sample remained in one piece edge and surface cracks highlighted with arrow (453 K, 1.67 strain, 4.19 strain rate), (c) shattered sample did not roll. (433 K, 1.67 strain, 4.19 strain rate).

The rolling strain applied to a rolled sample is calculated using the formula given in Eqn. (5):

$$\varepsilon = ln\,(t_o/t_f) \quad (5).$$

Where t_o = original part thickness and t_f = final part thickness.

The average strain rate is calculated by using Eqn. (6)

$$\dot{\varepsilon}_{ave} = \frac{v_r}{L}\, ln\frac{t_o}{t_f} \quad (6)$$

Where L = the contact length of the work piece to the roller surface and is calculated by $L = (R * d)^{0.5}$. R = radius of the work rolls. The term d is the draft of the work piece. The draft is defined as the change in thickness of the work piece during rolling, calculated by $d = t_o - t_f$. When calculating d, t_o = original thickness of work piece and t_f = final thickness of the work piece. v_r= linear velocity of the roll in $m \cdot s^{-1}$

Rolling trails are conducted using four different roll speeds and five different total strains. When rolling at both 423 K and 433 K all the samples shattered and are therefore given a rating of C. The results of the rolling trials for rolling temperatures of 443 K and 453 K are given in Table 11 and Table 12, respectively. The corresponding average strain rate value, $\dot{\varepsilon}_{ave}$, is given in the brackets for each combination of processing parameters in the tables; $\dot{\varepsilon}_{ave}$ is dependent on the contact length (L) of the work piece with the rolls, as the amount of strain is reduced, the strain rate does not decrease in a linear manner due to the effect of reducing the contact length. The roll speed is given as a linear speed whereas the average strain rate is the deformation per unit time measure. The use of strain rate allows for the use of roll mills with differing roll diameters to give equivalent results. At both 463 K and 473 K all the samples rolled with a rolling quality rating of A at all strain rates using the same test matrix as for the rolling trials at 453 K.

Table 11 Rolling results for samples rolled at 443 K. The corresponding average strain rate value, $\dot{\varepsilon}_{ave}$, is given in the brackets.

Linear Roll Speed ($mm \cdot min^{-1}$) / **Rolling Strain**	**280**	**530**	**1650**	**5360**
2.59	C (1.03)	C (1.95)	C (6.08)	C (19.77)
1.67	C (0.71)	C (1.34)	C (4.19)	C (13.63)
0.98	C (0.47)	C (0.9)	C (2.8)	C (9.11)
0.28	A (0.22)	B (0.41)	B (1.3)	C (4.22)
0.13	B (0.144)	B (0.27)	B (0.85)	A (2.77)

Key A = rolled with no visible defects, B = rolled with surface defects, C = shattered did not roll.

Table 12 Rolling results for samples rolled at 453 K. Numbers in brackets are the calculated rolling strain rates for each condition.

Linear Roll Speed ($mm \cdot min^{-1}$) / **Rolling Strain**	**280**	**530**	**1650**	**5360**
2.59	A (1.03)	A (1.95)	C (6.08)	A (19.77)
1.67	A (0.71)	A (1.34)	B (4.19)	A (13.63)
0.98	A (0.47)	A (0.90)	B (2.80)	C (6.11)
0.28	A (0.22)	A (0.41)	A (1.30)	A (4.22)
0.13	A (0.14)	A (0.27)	A (0.85)	A (2.77)

Key A = rolled with no visible defect, B = rolled with surface defects, C = shattered did not roll.

The use of the upper region of the SCLR for successful rolling has also been shown previously by Martinez *et al.* [59] who used a pack rolling approach to roll a $Zr_{44}Ti_{11}Cu_{10}Ni_{10}Be_{25}$ BMG. However, when holding a BMG within the SCLR the stability of the glass decreases with an increase in temperature, as shown in Figure 50. For a sample to be rolled at 463 K, to ensure high quality rolling, the sample needs to be heated to 463 K and rolled in under 5 minutes to prevent the onset of crystallisation. When selecting a suitable rolling temperature a combination of the stability at the temperature in question and the quality of rolled part are the variables that need to be optimised.

Between 443 K and 453 K the formability of the alloy is influenced substantially by the combination of strain and strain rate employed. At 443 K the alloy could be rolled as long as the strain rate did not exceed 4 s^{-1}. As the temperature increased to 453 K, the parameter range available for successful rolling increased. At 453 K the regions that resulted in successful rolling to high levels of strain, are those at a low strain rate, below 4 s^{-1}, and at a high strain rate, above 13 s^{-1}, as shown in red in Figure 52. There is a high amount of uncertainty around the construction of the graph with their only being two data points above a rolling strain rate above 10 s^{-1}. Because of this limitation the bottom right quadrant of the map has been blacked out and the exact position of the contours in the upper right quadrant are also unclear.

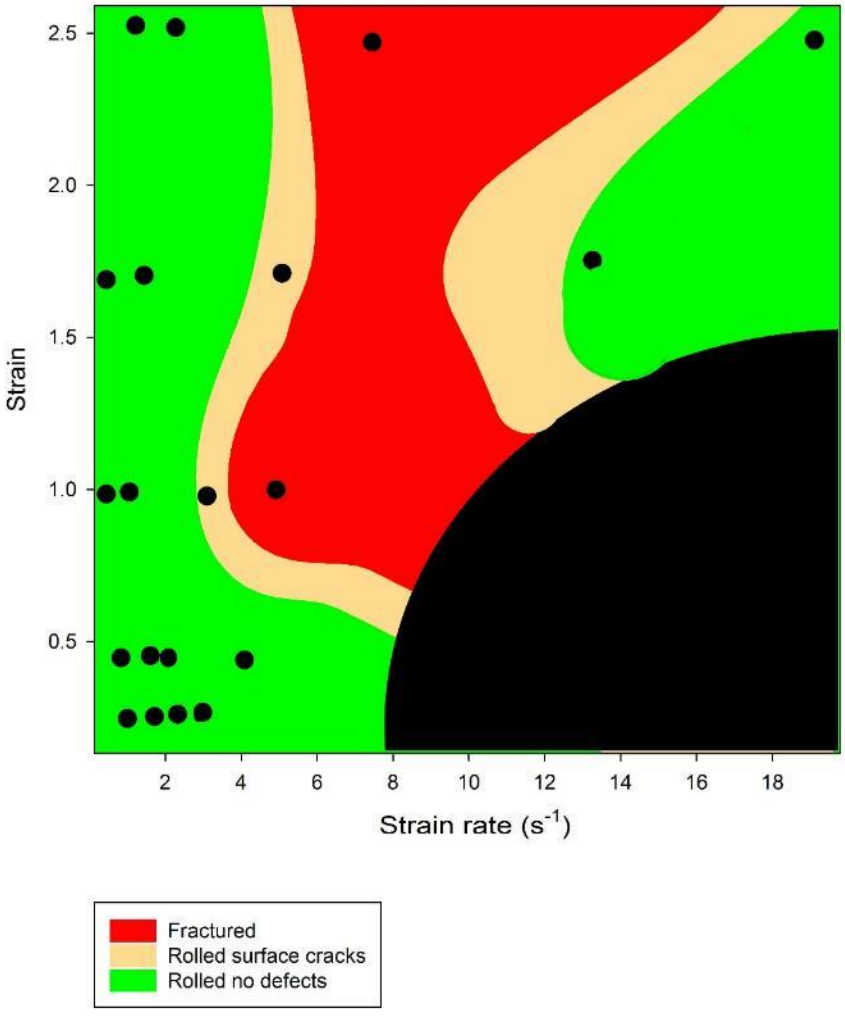

Figure 52 Processing map for $Mg_{60}Cu_{29}Gd_{11}$ BMG rolled at 453 K. Black dots are the data points for the graph, blacked out region at high strain rate and low strain is a region where data could not be gathered due to the limit of the rolling mill speed.

5.2.3 Heat transfer during hot rolling

During the rolling trials isothermal rolling conditions are attempted. To achieve isothermal conditions the samples are heated in an air circulation furnace to the rolling temperature. The rolling mill had heated rolls that are set to the same temperature as the preheat furnace. The temperature profiles of samples are measured with embedded thermocouples. Samples are cast with a 0.1 mm thermocouple embedded in the centre of the bar. These samples are then rolled to obtain a thermal profile for the work piece as it passed through the roll gap.

During rolling, the control of the work piece temperature is critical for a successful result. The heat flow during rolling can be split into three separate heat transfer regions:

1. The heat loss that occurs between the preheat furnace and the preheat rolls.
2. The conductive heat transfer from the rolls to the work piece.
3. The adiabatic heating produced from plastic deformation.

An example of the change in work piece temperature as it passes through the various stages of rolling is illustrated in Figure 53 for two different strain rates. Within the plateau region the samples are inside the preheat furnace. The following downward slope is where the samples are transferred from the preheat furnace to the roll bite, here the samples lose temperature through radiation and convective heat transfer to the environment. For the differing strain rates the temperature profiles now change. The sample rolled at a strain rate of 13.63 s^{-1} shows a domination of adiabatic heating during deformation, as indicated by the temperature spike after material transfer. The sample rolled at a strain rate of 0.7 s^{-1} takes longer to pass through the roll bite and therefore conductive heat transfer is becoming the more influential mechanism, as indicated by the slower increase in temperature as the piece passes through the roll bite.

Although isothermal rolling has been attempted, during the transfer of the sample from the furnace to the roll bite, convective heat loss occurs. This heat loss can be described by Newton's law of cooling, Eqn. 7, defined as [95]

$$mC_p \frac{dT}{dt}T = -hA(T - T_\infty) \quad (7)$$

Where T = temperature of work piece, $\frac{dT}{dt}$T = temperature of work piece after time t, T_∞= ambient room temperature, A = surface area of work piece, h = convective heat transfer coefficient m = work piece mass and C_p = specific heat of work piece.

Samples are preheated in an air circulation furnace where they are heated to the target rolling temperature. Once the rolling temperature has been reached the samples are removed from the furnace and transferred to the roll bite. During transfer from the furnace to the roll bite the work pieces lose temperature, due to convective heat loss. This heat loss has been measured by a thermocouple cast into the work piece, a 20 K drop in temperature is recorded (Figure 53).

For all the temperatures trialled the sequence of convective heat loss followed by a temperature increase dominated by conductive or adiabatic heat transfer persisted. In a traditional crystalline alloy the preheat temperature of the work piece would be increased to compensate for such a heat loss on transfer. However, for a BMG, the application of extra heat to the work piece is limited by the T_x temperature. The T_x temperature cannot be exceeded during preheating since the glass will begin to crystallize above this temperature.

During rolling of metallic glass samples, temperature changes occur throughout the nip region. The change in temperature within the roll bite can be calculated by:

$$\Delta T_{Total} = \Delta T_{gain} - \Delta T_{loss} \quad (8)$$

With ΔT_{gain} being the rise in temperature as a result of adiabatic heating within the work piece due to the work of deformation. Conduction to the roll surface is given by the, ΔT_{loss} term in Eqn. 8. However, in the present case, are the rolls are preheated, they can act as a heat source not a heat sink as is normally the case in rolling [96].

$$\Delta T_{Total} = \left[\frac{P_r\, L/R}{\rho C_p h_{ave}}\right] - \left[60\alpha \sqrt{\frac{r}{h_{entry}R}}\left(T_{strip} - T_{roll}\right)\left[(1-r)\pi\rho C_p N\right]^{-1}\right] \quad (9)$$

Where P_r = roll pressure, L = contact length, R = roll radius, ρ = density of sample, C_p = specific heat, h_{ave} = average strip thickness, α = heat transfer co efficient strip – roll interface, N = roll rpm, r = reduction expressed as a fraction of initial thickness, h_{entry} = strip entry thickness, T_{strip} = temperature of strip and T_{roll} = temperature of roll.

The conductive heating portion is affected by the strain rate, given by the term N in Eqn. (9. This indicates the change in the temperature profile of the work piece is not due to the increase in adiabatic heating but rather to the decrease in the effect of conductive heat transfer.

The portion of Equation 9 that accounts for conductive heat transfer, ΔT_{loss}, is given by Eqn. 10. For the experimental setup used for this work the rolls are heated to the target work piece temperature. Due to the loss of heat in the transfer of the sample to the roll bite, the temperature of the work piece is now lower than that of the rolls, meaning the conductive heat flow is now from the rolls to the work piece. Slower roll speeds, by term N, enable the work piece to be heated back to the desired deformation temperature before the deformation is complete.

$$\Delta T_{loss} = -60\alpha \sqrt{\frac{r}{h_{entry}R}}\left(T_{strip} - T_{roll}\right)\left[(1-r)\pi\rho c_p N\right]^{-1} \quad (10)$$

The temperature profile of the BMG is measured during rolling (Figure 53). During low strain rates, the conductive heating from the roll surfaces to the work piece is the dominant heating mechanism. During low strain rate, rolling conductive heating increases the sample temperature to 453 K. Due to the low roll speed there is sufficient time for the work piece to equilibrate with the roll surface temperature. Adiabatic heating raises the work piece temperature to 463 K this temperature rise is smaller than that measured experimentally during rolling with a high roll speed. When the work piece temperature exceeds the roll surface temperature, the rolls then act as a heat sink. At higher strain rates, the contact time with the roll surfaces is reduced and as a consequence the effect of conductive heat transfer becomes less influential.

In high strain rate rolling, adiabatic heating dominates, causing a rapid increase in temperature of the work piece. The portion of Equation 9 that accounts for adiabatic heating is given by Eqn. 11. The work piece temperature, as it passes through the roll bite, is 508 K. The level of temperature increase during rolling at 13.36s^{-1} is 100 K. The use of rapid heating rates and strain rates have been shown to make large amounts of total strain possible without crystallisation [51].

At temperatures between 453 K and 463 K, the strain rate affects the quality of the samples produced. The viscosity of the sample controls the strain that can be applied to the sample without failure occurring. For BMGs, the viscosity value of the super cooled liquid is strongly dependent on the temperature of the sample. As the temperature increases towards the T_x temperature, the viscosity of the glass decreases until the T_x point is reached then the viscosity of the sample begins to increase once more as crystallization starts to occur [24]. The drop in viscosity in $Mg_{60}Cu_{30}Gd_{10}$ has

been shown to be four orders of magnitude throughout the SCLR [97]. This drop in viscosity with increasing temperature causes the shear strength to drop and therefore the heat produced through adiabatic heating to be reduced. Martinez et al. [59] reported the heat produced through deformation is overestimated by using the average viscosity values because as heat is produced, the viscosity of the sample drops. Within the adiabatic heating calculation the τ value is dependent on the viscosity of the material being rolled, Eqn. 13, for crystalline metals this value does not change dramatically with temperature. However, for magnesium BMGs the change can be up to 4 orders of magnitude [97]). For a more accurate prediction of the temperature increase when rolling dη/ dT should be introduced to the formula to account for the change in viscosity with change in temperature. The change in viscosity with temperature formula will be different for each BMG.

$$\Delta T_{gain} = \left[\frac{P_r\, L/R}{\rho C_p h_{ave}}\right] \quad (11)$$

Rewriting to use stress and strain values instead of the reduction values, as stress and strain values are used to replace the length of contact value which are roll mill configuration dependant.

$$\Delta T_{gain} = \propto \left[\frac{\varepsilon\tau}{\rho C_p}\right] \quad (12)$$

Where $\tau = \text{shear stress}$, $\rho = \text{density}$, and $C_p = \text{specfic heat capacity}$

Assuming Newtonian flow and all work is translated to heat α = 1

$$\tau = \eta \frac{3}{2} \dot{\varepsilon} \quad (13)$$

Where $\eta = \text{viscosity}$ and $\dot{\varepsilon} = \text{average strain rate.}$

If the calculation is done for rolling at 463 K using Eqn. 11, without allowing for the change in viscosity the calculated temperature rise is 443 K. The amount of heat generated through the roll bite at high strain rates has been measured as 70 K (Figure 53). As can be seen from the difference between the measured and calculated temperature increases the adiabatic heating calculations overestimate the heat produced through rolling in BMGs. Equation 13 shows that the viscosity value of the supercooled liquid is proportional to the shear stress applied. Feeding this result back to Eqn. 12 the shear stress and therefore the viscosity of the supercooled liquid is proportional to the temperature gain induced by adiabatic heat transfer. The temperature trace for samples rolled at three different temperatures 443, 453 and 463 K are recorded these are shown in Figure 53. At each temperature two different strain rates are used, i.e. 0.7 s^{-1} and 13.63 s^{-1}. It can be seen that similar trends with strain rate are observed for each rolling temperature.

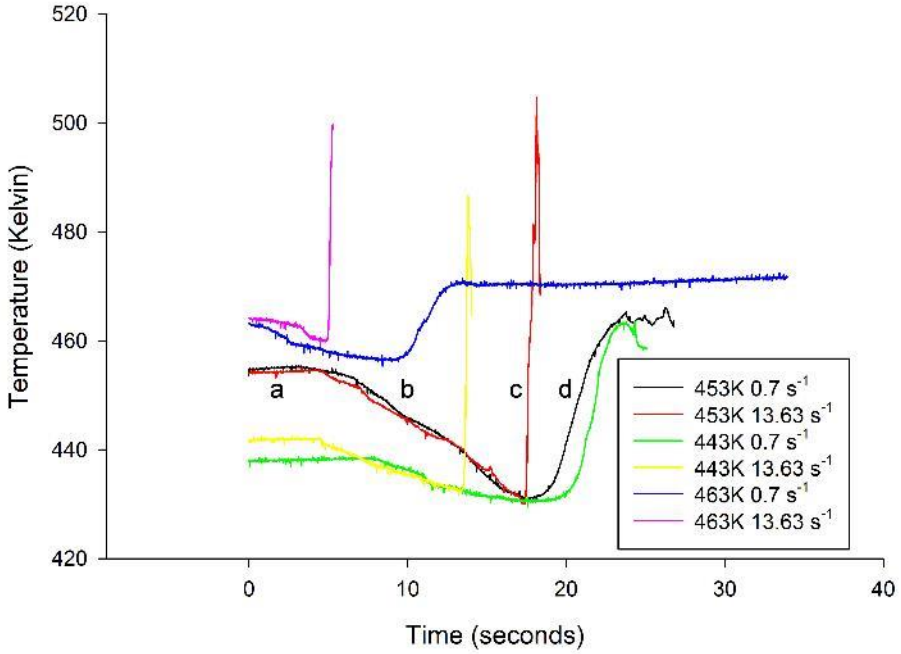

Figure 53 Embedded thermocouple temperature measurement traces from rolled samples. Samples are rolled with a rolling strain of 1.62 at two strain rates 0.7 and 13.63 s^{-1}. Samples are rolled at three different temperatures within the SCLR of the BMG. Heat transfer regions during rolling process. a) Pre-heat plateau in furnace. b) Followed by convective heat transfer between furnace and rolls. c) Rolling process at 13.63 s^{-1} strain rate, adiabatic heating dominant resulting in a temperature spike. d) Rolling at 0.7 s^{-1} conductive heat transfer dominant resulting in slower rate of temperature increase.

5.2.4 Characterisation of structural evolution during rolling

Prior to, and after rolling, the BMG samples are characterised by XRD. To the detectable limit of XRD, the samples remained amorphous for all rolling conditions investigated the conditions are list in Figure 54. The XRD traces in Figure 54 are all devoid of sharp peaks that indicate the presence of a significant volume fraction of crystalline phases. The traces all show a broad amorphous peak between 30° and 40° 2θ, Figure 54.

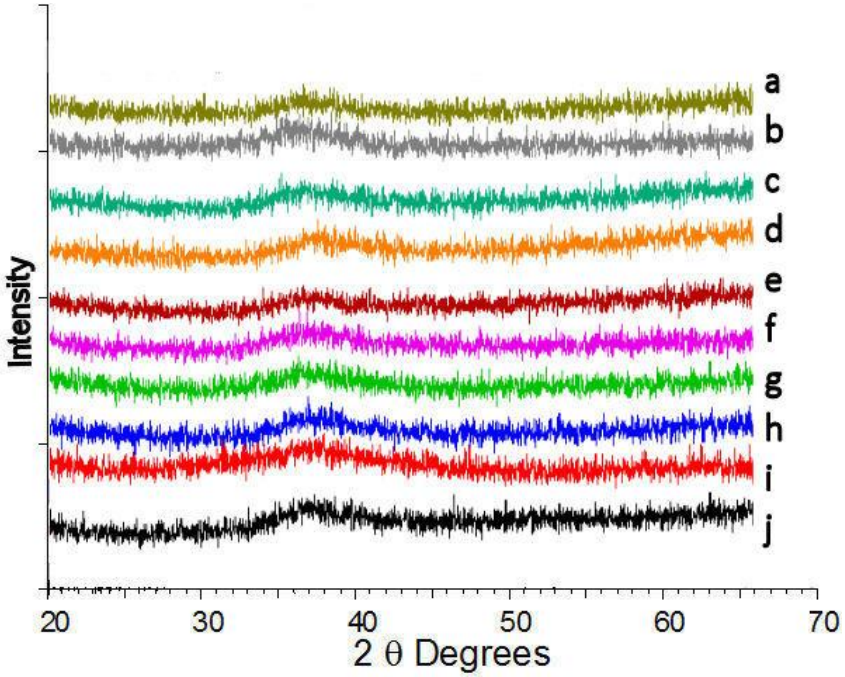

Figure 54 XRD scans of samples that have been rolled under various rolling conditions, all samples show no signs of crystallisation. The following samples have a strain rate of 0.7 s^{-1} with a strain of (a) 0.133, (b) 0.98, (c) 1.62 rolled at 453 K. (d) rolled at 443 K, 1.62 ε and 13.63 s^{-1}. (e) rolled at 443 K, 1.62 ε and 13.63 s^{-1}. f) rolled at 453 K, 1.62 ε and 0.7 s^{-1}. (g) rolled at 453 K, 0.7 ε and 13.63 s^{-1}. (h) rolled at 46 3K, 1.62 ε and 0.7 s^{-1}. (i) rolled at 473 K 1.62 ε and 0.7 $s^{-.1}$ (j) rolled at 473 K, 0.7 ε and 13.63 s^{-1}.

DSC of the rolled samples revealed the ΔH of crystallisation is lower and the point at which crystallisation takes place is decreased (Figure 55). This indicates a structural change taking place within the BMG. When a metallic glass passes through the T_g point, the changes to the structure of the material should be erased. As the temperature increases, the mobility of the atoms increases, creating new free volume and returning the structure to its relaxed state. The lowering of the T_x point and lowering the exothermic peak of crystallisation signal is the result of a change in structure that survives the glass transition. The presence of crystalline particles or a change in atomic arrangement would explain the change in T_x and ΔH.

The noted effects of rolling are a reduction in the peak energy at crystallisation and a reduction in the T_x are listed in Table 13.

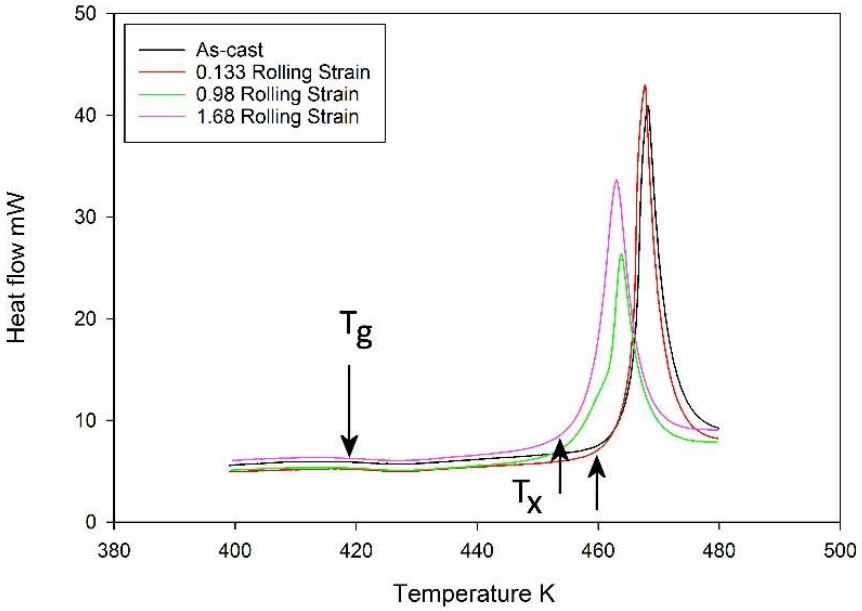

Figure 55 DSC of samples as-cast, 0.133, 0.98, and 1.68 rolling strain with a strain rate of 0.7 s^{-1}. Scan rate for the experiments is 5 degrees per minute.

Table 13 Glass transition (T_g) and crystallisation temperature (T_x) of samples rolled at various strains with strain rate of 0.7 s^{-1}.

Sample	T_g (K)	T_x (K)	Peak crystallisation energy (mW)
As-cast	429	460	40.7
0.133 rolling strain	429	460	42
0.98 rolling strain	429	452	33
1.68 rolling strain	427	452	26

After rolling, samples are heat treated at 453 K for 120 minutes in an Inel in-situ XRD machine using cobalt radiation to examine if rolling has an effect on the crystallisation of the alloy. It is found the rolled samples (Figure 56(b) and (c)), began to crystallise 5 minutes earlier than the as-cast sample Figure 56(a). The in-situ XRD experiments also show that by subjecting a sample to an imposed strain the proportion of the crystallised phases can be changed. When comparing the as-cast to the rolled samples no new peaks are observed, but the intensity of the peaks do change.

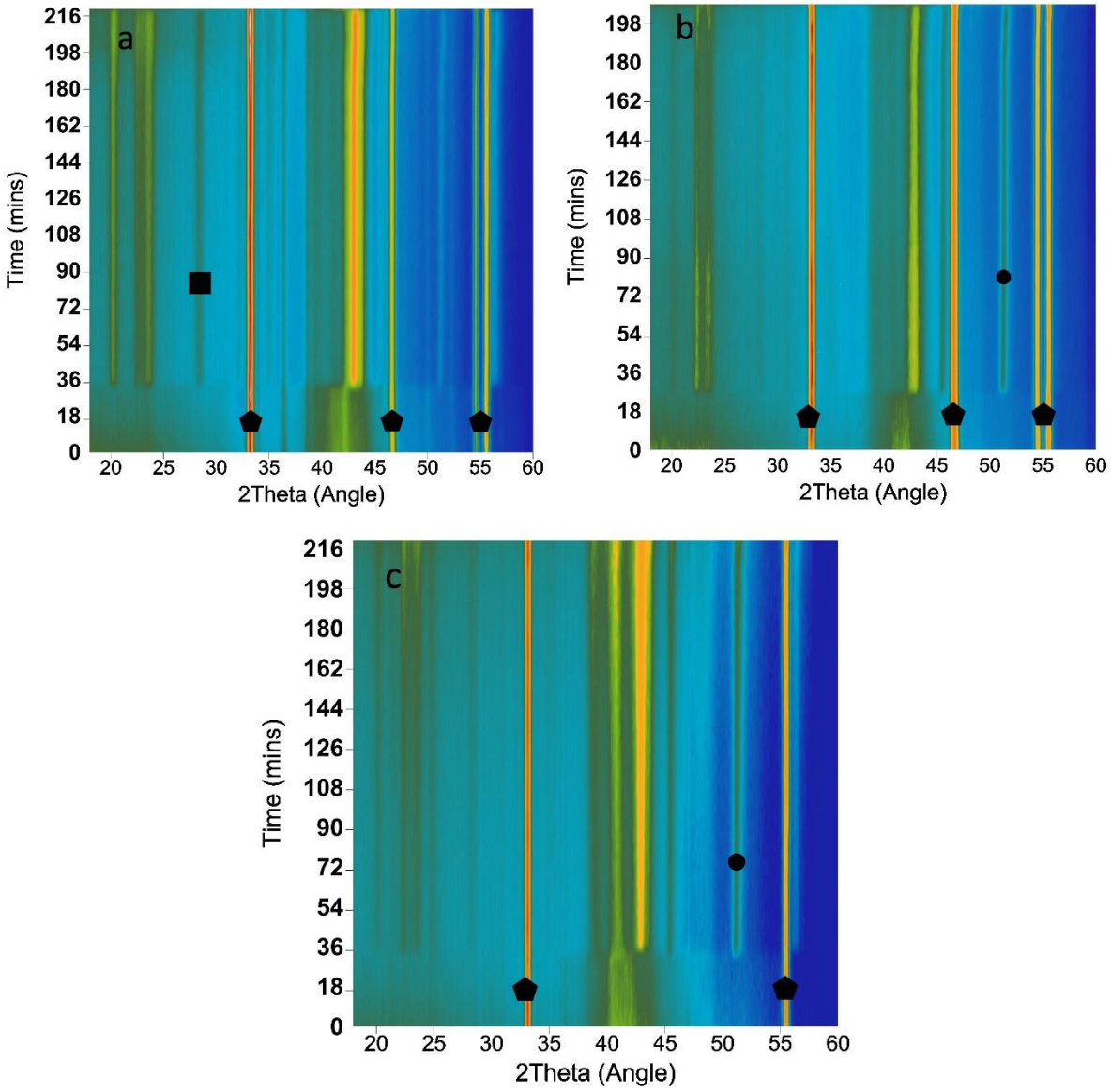

Figure 56 Plan view of multiple XRD scans taken during an in-situ heat treatment of 453 K for 120 minutes this technique is used to investigate if any changes occur as a function of time at temperature. (a) Data taken from an as-cast sample, once the samples have crystallised there are no subsequent phase changes in two hours of data collection, as there are no new peaks formed after the initial transformation. (b) Data taken from samples that is rolled at 453 K at 1.68 rolling strain and 13.63 s^{-1} strain rate. (c) Data taken from sample that is rolled at 453 K with a rolling strain of 1.68 and a strain rate of 0.7 s^{-1}. The lines that continue into the amorphous region of the scan below 30 minute mark in (a), (b) and (c) are peaks from Si (33 and 55 degrees) which is mixed with the samples to reference the stage location. In scan (a) and (b) peaks from the Pt heating stage (47 and 54 degrees) can be seen. These reference peaks are marked with a Pentagon.

The scans in Figure 56(b) and (c), contain reference lines that are from Si, which is used to locate the stage within the XRD unit, and Pt lines, which are artefacts from the heating stage. The Pt lines are not present in scan (c) as the heating stage must have been 100% covered by the sample.

In Figure 57, XRD scans are shown that come from the samples that have undergone a heat treatment and an as-cast sample but contains some reference lines. If the lines at 33, 46 54 and 56

degrees are discarded, then the XRD scans from the samples at high and low strain rate are similar The only difference in the scans from specimens rolled at high and low strain rates is the high strain rate sample has a minor peak at 41 degrees that is not present in the low strain rate sample.

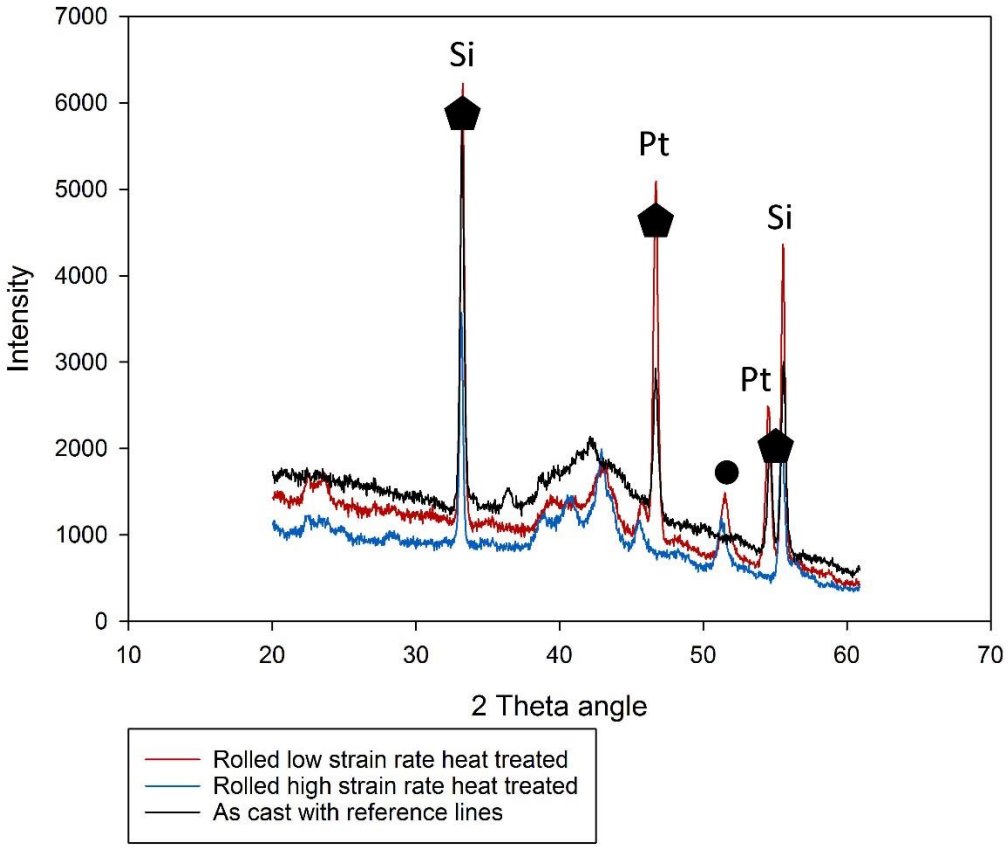

Figure 57 XRD scans taken with Co radiation from samples rolled at high and low strain rates. Black scan is the as-rolled sample containing the reference material used to locate the detector. The lines at 33, 46, 54 and 56 degrees are reference lines from the Pt (111) and Pt (200) and Si (111) and (220) added to the sample to locate the sample within the XRD detector.

A difference in the phases present after crystallisation can be seen in Figure 58, this shows a sample that has been heat treated only and a sample that has been rolled before heat treatment, both samples are heat treated for 120 minutes at 453 K. The d-spacing of the peaks at 48 degrees and 25 degrees are present in the sample that is heat treated without rolling marked with a square. The sample that is rolled prior to heat treatment does not show the peaks at 25 and 48 degrees but does show peaks at 39 and 44 degrees marked with a circle.

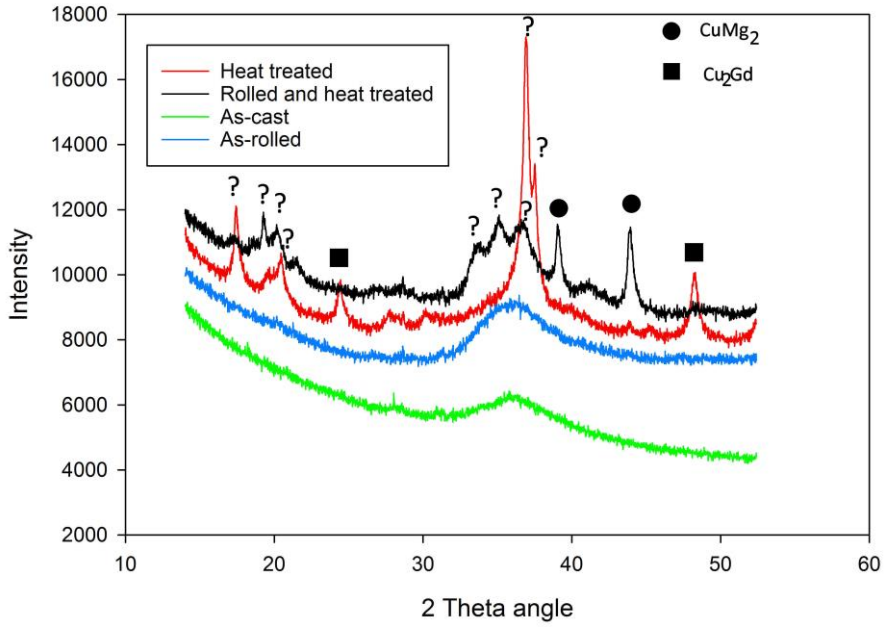

Figure 58 XRD scans taken with Cu radiation from a sample rolled at 453 K, rolling strain 1.68, strain rate of 13.63 s^{-1} and an unrolled sample. Scans are taken in the as-rolled and as-cast state and again after a heat treatment of 120 minutes and 453 K. The heat treated sample has peaks at 25 and 48 degrees Cu_2Gd (orthorhombic a = 0.4320 nm, b = 0.6858 nm, c = 0.528 nm) (marked with a square). The sample that is rolled prior to heat treatment has peaks present at 38 and 44 degrees $CuMg_2$ (orthorhombic a = 0.907 nm, b = 1.824 nm, c = 0.528 nm) (marked with circles). There are several peaks present that cannot be indexed to a known phase (marked with a ?), it is likely that there are unknown metastable phases present in this sample.

Analyses are performed on the collected XRD data using the Bruker XRD search match program EVA™. The peak positions of the rolled and heat treated sample approximately match that of $CuMg_2$, this binary phase is reported as the initial phase to from by soubyoux *et al*. [26]. The scans in Figure 58 show different peak locations to that of the standard $CuMg_2$ (orthorhombic a = 0.907 nm, b = 1.824 nm, c = 0.528 nm) the standard peak position should be 39 and 45 degrees compared to 38 and 44 in the rolled and heat treated sample. This deviation could be caused by a substitution of Gd into the $CuMg_2$ lattice. The phase is possibly the same space group as $CuMg_2$ (orthorhombic-Fddd). When collecting this data crushed powders are used as the sample preparation method, this removes texturing and sample size as possible causes of the peak position difference from the reference position. Further analysis of the chemical composition of the phases will be needed to confirm the chemical substitution within the crystal. For the unindexed peaks in this sample there are unknown phases these could be either a metastable quasicrystalline phase, unknown crystalline phases or a combination of both.

Throughout the remainder of the in-situ XRD experiment the d spacing's do not change after the initial crystallisation event. The XRD traces contained in Figure 59 show that the d spacing's between 120 minutes and 16 hours of heat treatment after rolling.

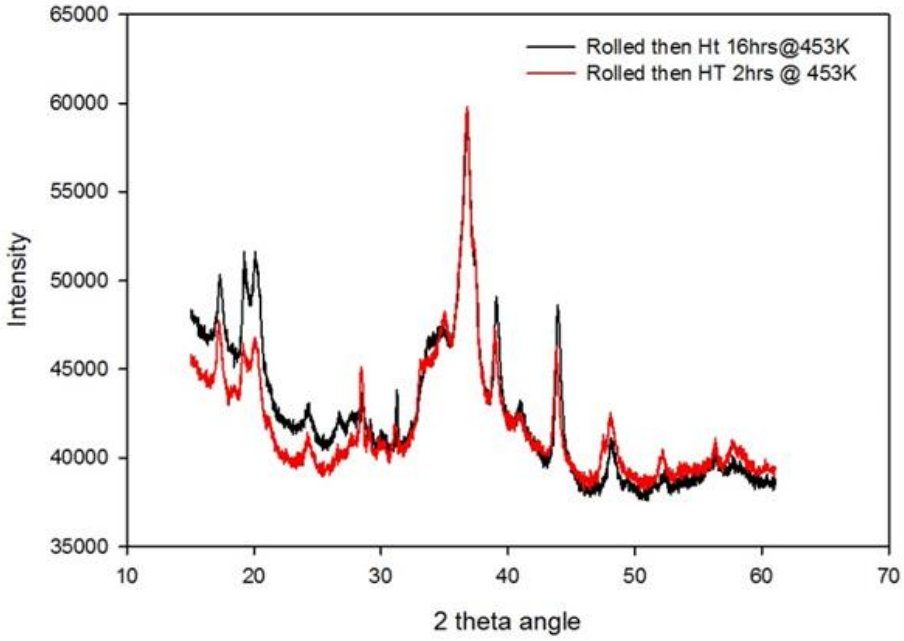

Figure 59 XRD scans of cast sample after 2 hours and 16 hours heat treatment at 453 K.

5.2.5 Increase in order due to strain

In order to characterise the samples in further detail than what is possible by XRD scans XAFS measurements are under taken to identify differences between the rolled and as-cast samples. XAFS measurements are taken from samples in the as-cast state, the annealed to crystalline state (no external imposed strain) and samples strained to 0.98 and 1.69 rolling strain. XAFS probes a specific atom and provides a measurement of the atomic spacing around the targeted atom. Again, for this work the probed atom is the Cu atom. The higher the peak of the Fourier transform the greater the number of atomic spacings that are of that length. An increase in the height of the Fourier transform with an increase in the rolling strain indicates that there is an increase in short-range atomic order. The degree of order within the $Mg_{60}Cu_{29}Gd_{11}$ BMG is determined to increase with an increase in strain, with the values given in Table 14 and shown graphically in Figure 60.

The XAFS analysis also shows a change in the bond length, as strain is accumulated within the material. The peak of the graph is the mean average bond length value. The average bond length of the Cu atom changes with the application of strain, the change in bond length is also given in Table 14. The change in bond length is not a linear relationship with deformation.

Table 14 Average nearest neighbour bond length around Cu atom.

Condition	Mean average bond length around Cu atom (Å)	Magnitude of Fourier transform
As-Cast	2.393	3.40
0.98 Rolling strain	2.331	3.84
1.68 rolling strain	2.362	4.15
Annealed to crystalline 16 hours at 453 K	2.331	4.28

XAFS measure many bond lengths with each scan, giving a good average bond length value centred on the probed atom. The average bond length value determined is an average value with Cu-Cu bonds, Cu-Mg bonds and Cu-Gd bonds all contributing to the value.

The formation of crystalline particles with their periodic atomic spacing would cause the height of the Fourier transform to increase, due to the higher number of spacings at a set distance.

The application of a strain to the sample leads to a decrease in mean bond length. However the change in bond length is not a linear progression. The application of 0.98 rolling strain causes a reduction in the mean bond length of 0.062 Å, a larger amount of strain 1.68 rolling strain results in a reduction in mean bond length of 0.031 Å. This nonlinear trend with the application of strain is also noted in the DSC scans of the rolled material (Figure 55) where the peak crystallisation energy also is reduced to a greater degree in the sample rolled to 0.98 strain compared with that rolled to 1.68.

XAFS is unable to detect if the change in bond length is due to crystals forming or changes in atomic clusters. In order to confirm if the change in bond length is due to the formation of crystals TEM imaging has been used.

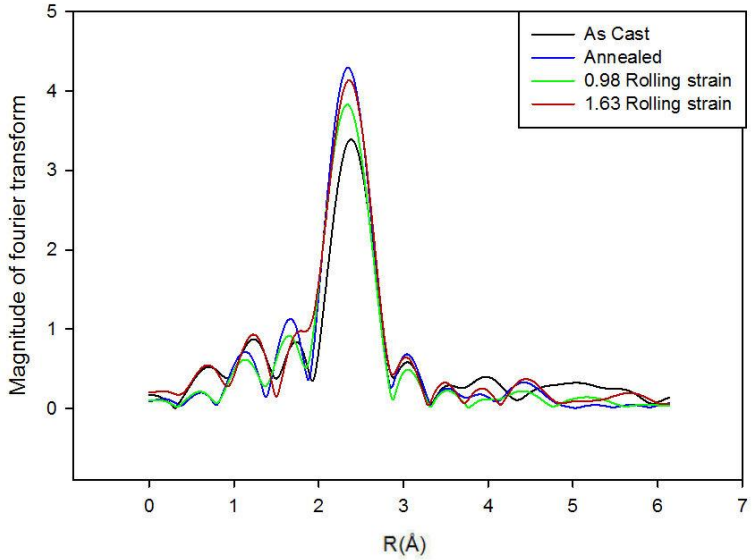

Figure 60 XAFS spectra showing the increase in order brought on by rolling. The sample with the least amount of order is the as-cast sample, order increases through 0.98 rolling strain, 1.68 rolling strain samples with the annealed for 16 hours at 453 K to crystalline sample showing the highest amount of order.

5.2.6 Crystallite formation due to strain

TEM analysis is able to detect any crystal formation that falls below the detectable limit of XRD. To quantify the effect of strain, a sample is isothermally annealed without the application of strain. The annealed (2 min and 453 K in an air furnace to give the same thermal history as the strained sample,) sample maintained its amorphous structure as can be seen in Figure 61, which shows both the as-cast and as-annealed structures to be 100% amorphous.

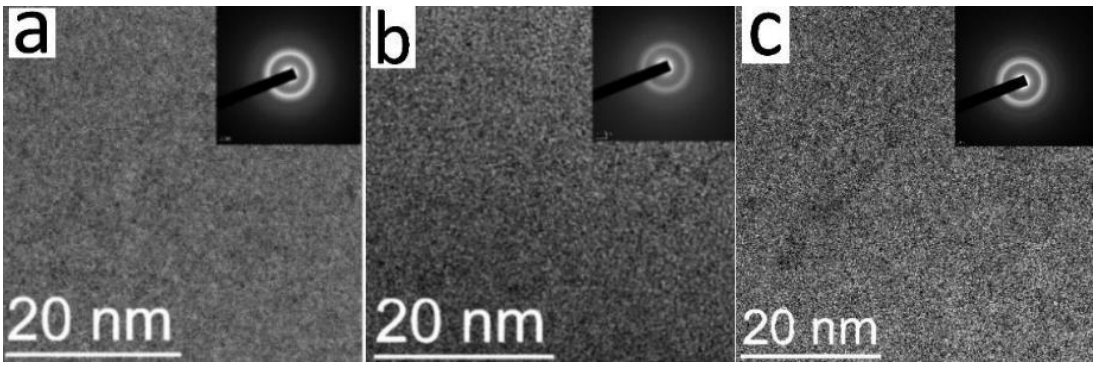

Figure 61 Transmission electron micrographs showing (a) as-cast sample with amorphous ring and no crystallites, (b) annealed 2 min at 453 K sample that is 100% amorphous, and (c) sample rolled with a strain of 0.98 and a strain rate of 13.63 s^{-1}. The sample in (c) is also 100% amorphous.

In addition, for a rolling strain of 0.98 at 453 K the sample remains full amorphous with no signs of crystallite formation, as shown in Figure 61(c).

In the samples rolled to a strain of 1.68, a difference in structure is observed between the samples rolled with a high strain rate as opposed to with a low strain rate. In the specimen deformed with a strain rate of 0.7 s^{-1}, the structure remains 100% amorphous with no signs of crystals forming within the amorphous matrix (Figure 62(a)). However, in the sample rolled at a high strain rate, crystals are observed to have formed within the amorphous matrix (Figure 62(b)). The crystals in Figure 62(b) are the lighter regions spread throughout the darker amorphous matrix, as marked by the circles in Figure 62(b).

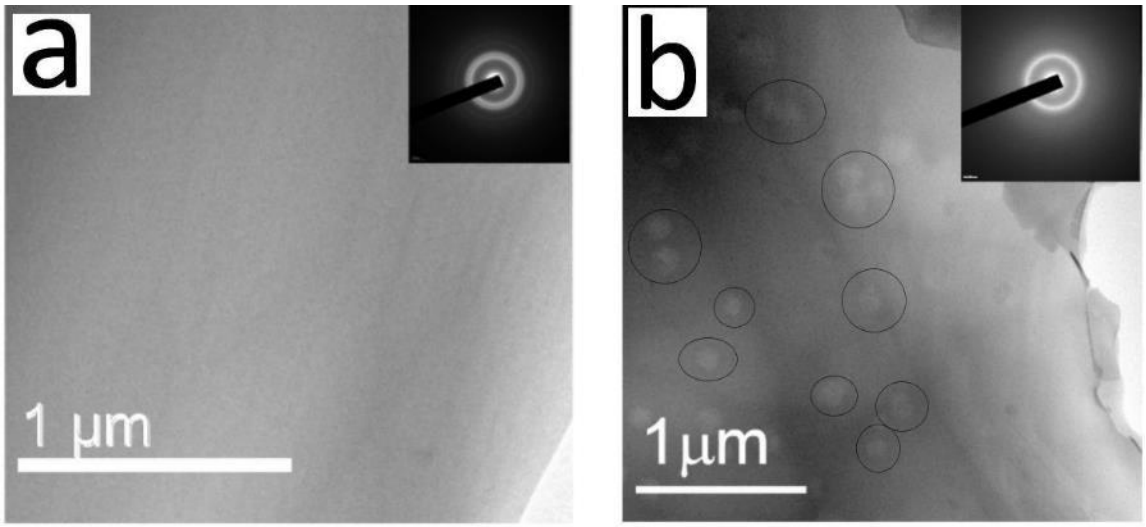

Figure 62 Transmission electron micrographs showing (a) sample rolled with a rolling strain of 1.68 and a strain rate of 0.7 s^{-1}, and (b) sample rolled with a rolling strain of 1.68 at a strain rate of 13.63 s^{-1}. Sample in (a) is 100% amorphous. Second phase particles are visible in the amorphous matrix in (b). Inset in each micrograph is a selected area diffraction pattern from the matrix showing an amorphous ring.

Higher magnification images of the particles are shown in Figure 63, in this image the particle size is approximately 30 nm. The HAADF-STEM image of the particle shows a low contrast between the particle and the matrix. This is an indication that the compositions of the particle and the composition of the matrix are similar.

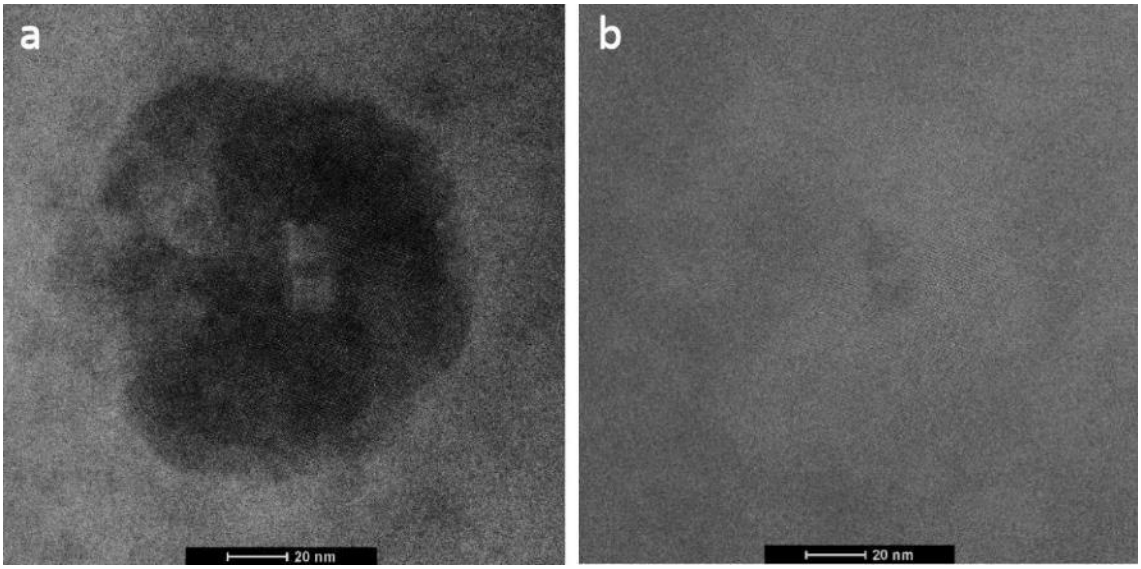

Figure 63 (a) Bright field image and (b) HAADF-STEM image of a particle in an amorphous matrix. The lack of contrast in (b) indicates that the composition difference between the particle and the matrix is minimal.

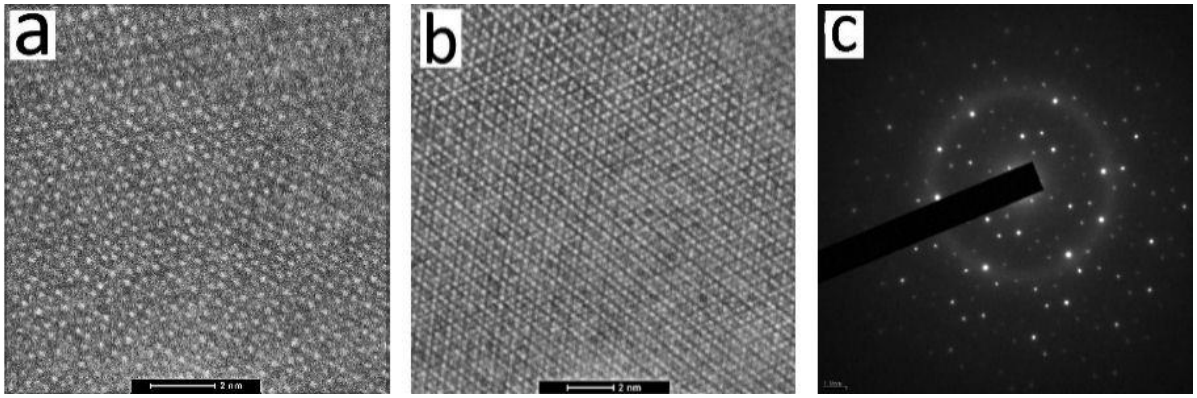

Figure 64 High-resolution HAADF-STEM images showing (a) 5-fold and (b) 3-fold distribution of atomic columns. (c) Selected area electron diffraction pattern displaying 2-fold axis of symmetry. The sample is subjected to a 1.68 rolling strain, with a strain rate of 13.63 s^{-1}.

In order to examine the spherical particles in greater detail HAADF-STEM imaging is performed, this technique can produce atomic level resolution in imaging. Figure 64(a) and (b), shows the five-fold and three-fold distribution of atomic columns, respectively, with each dot on the image being an atomic column. Figure 64(c) is a selected area electron diffraction pattern showing the two-fold axis of symmetry. The presence of two-, three- and five-fold axes of symmetry within the structure indicates that the spherical particles are quasicrystals. Energy-dispersive X-ray spectroscopy (EDS) chemical composition mapping of the quasicrystals shows that the copper content of the quasicrystal is lower than that of the matrix (Figure 65(d)). Samples that have been subjected to a 2-minute anneal and a 0.98 rolling strain do not show any detectable sign of chemical segregation.

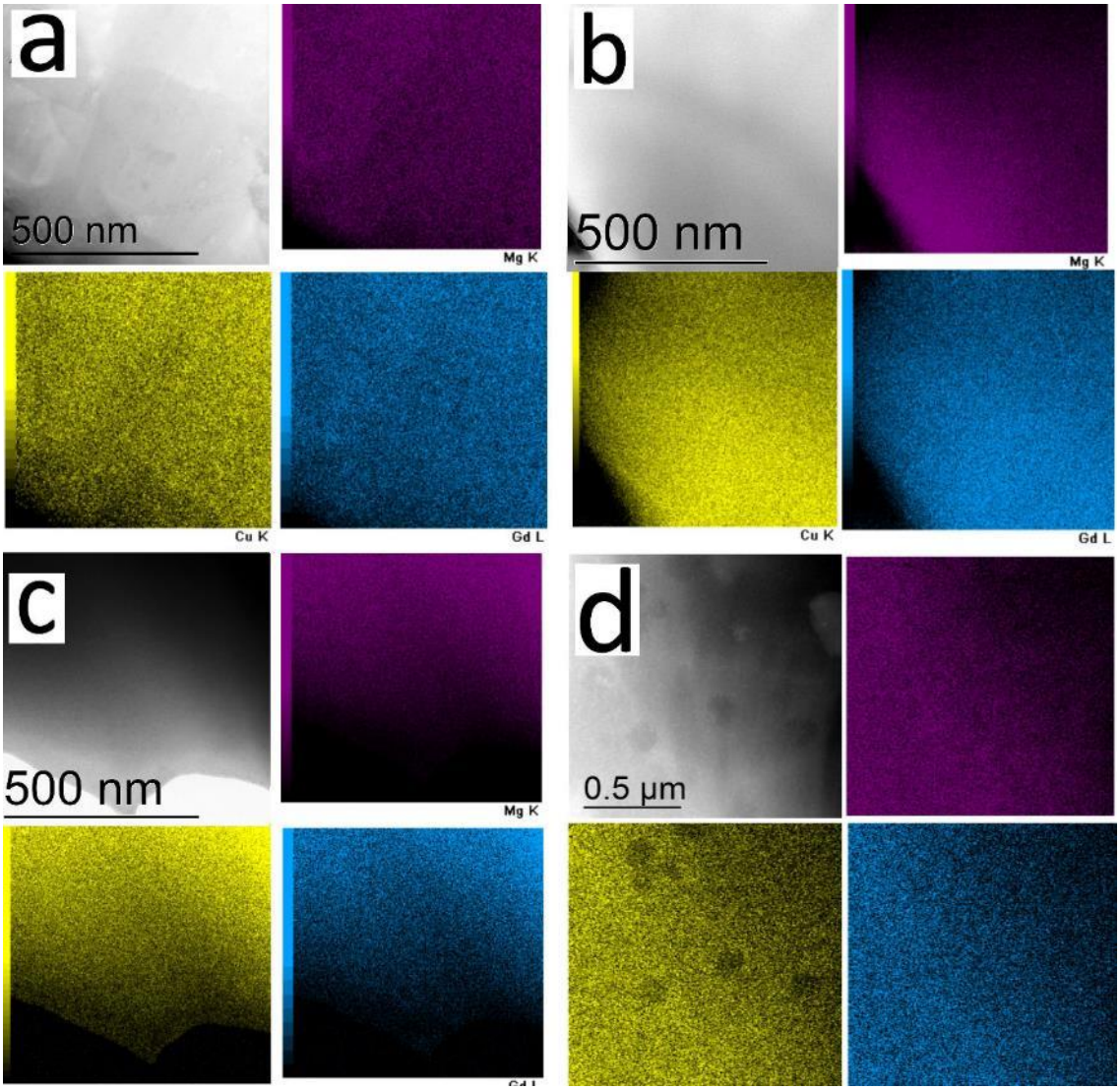

Figure 65 HAADF-STEM images and corresponding EDS maps showing elemental distribution in samples of different conditions. (a) As-cast, (b) 2 minutes at 453 K, (c) 0.98 rolling strain, and (d) 1.68 rolling strain. Maps in (d) indicate that the quasicrystals are slightly low in Cu and that no chemical segregation occurs before quasicrystal formation. Chemical maps are colour coded Pink = Mg, Yellow = Cu and Blue=Gd.

The change in devitrified phase formation through the application of strain in the SCLR has been noted previously in Cu-based glasses by Tan *et al.* [98]. They suggested that the change in crystallisation behaviour is due to the formation of nanocrystalites during deformation.

The in-situ XRD experiments indicated the application of 1.68 rolling strain to a sample will change the phases formed on devitrification (Figure 56). This observed change is independent of strain rate, indicating the source of the change in phase ratio on decomposition is occurring in both samples. The formation of quasicrytaline particles in the sample deformed at 13.63 s^{-1} is due to the temperature spike caused by rolling at a high strain rate, allowing the crystallites to grow to a detectable size. Due to the rapid heat rise and subsequent rapid cooling the time frame is such that the quasicrystals do not have time to decompose.

5.2.7 Formation of metastable quasicrystals

The only sample that shows crystallization is the sample that has undergone a 1.68 rolling strain at a strain rate of 13.63 s^{-1}. The initial phases that form in Mg-Cu-Gd based glass when subjected to heat treatment have been previously identified as Mg_2Cu. To characterise the initially formed phase HAADF-STEM imaging is performed, the HAADF-STEM images in Figure 64 show the three-fold and five-fold axis of symmetry. Both diffraction patterns and HAADF-STEM images confirm that the phase forming in the BMG is a quasicrystalline phase; this phase has not previously been reported in the Mg-Cu-Gd BMG system. The formation of icoshedral I phase in Mg–Zn–RE systems is well known and has been report extensively [99-101]. An icosahedral phase has been reported in the Mg-Zn-Cu-Gd system [102]. The reported alloy is of $Mg_{94.4}Zn_{3.5}Cu_{1.5}Gd_{0.6}$ composition, the icosahedral phase formed in this system has a composition of $Mg_{53.6}Zn_{26.98}Cu_{12.85}Gd_{6.57}$. This alloy system shows that copper can be incorporated into the icosahedral phase.

Embedded thermocouples within the deformed BMG showed that at high strain rate the temperature within the glass peaks rapidly and is then quenched back down to below the T_x temperature (Figure 53) - whereas at low strain rates the temperature of the glass is kept below the T_x point at all times. This rapid heating followed by rapid cooling allows the formation of quasicrystals. The energy barrier to formation of crystalline phases has not been exceeded in the rapid heating then quenching that takes place in high strain rate rolling.

To investigate the stability of the quasicrystals, the rolled sample is heat treated for 16 hours in oil bath at 453 K. The diffraction pattern shown in Figure 66 has no amorphous ring present. Measurements of the ring d-spacings in the diffraction pattern revealed that none of the d-spacings matched those characteristic of the quasicrystalline phase. The lack of matched d spacings with those of the quasicrystal indicates that the quasicrystals have transformed into other phases. After heat treatment the sample is fully crystalline and the quasicrystals are no longer present within the microstructure, indicating that the quasicrystals are metastable and not an equilibrium phase. The phases that are present in the TEM images are the same as the phases that are present within the sample after heat treatment, as Figure 59 shows, the XRD trace does not change for samples heat treated for up to 16 hours.

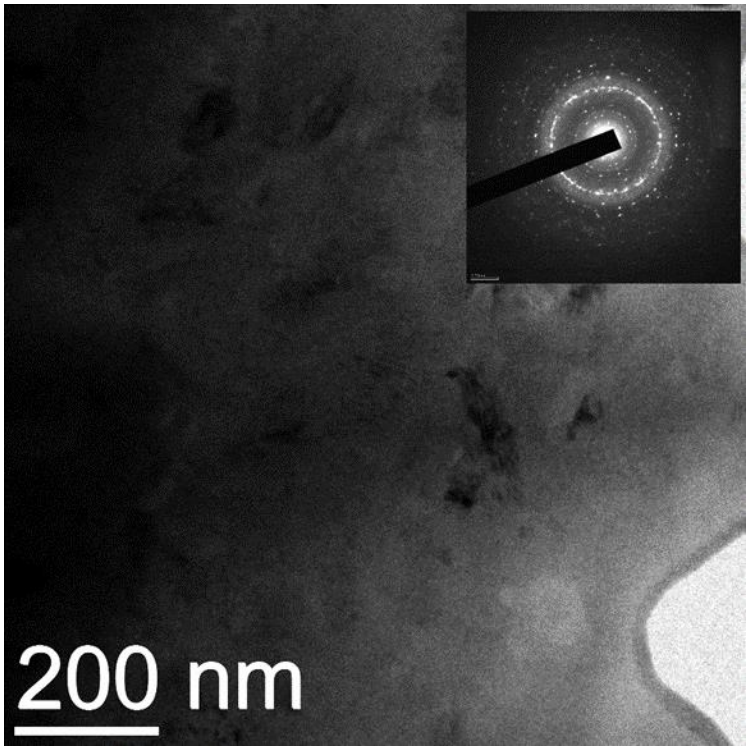

Figure 66 Transmission electron micrograph and corresponding SAED pattern (insert) showing microstructure of a sample after rolling at 453 K at strain rate of 13.63 s^{-1} and total rolling strain of 1.68, followed by heat treatment at 453 K for 16 hours. None of the d-spacings on the diffraction pattern could be attributed to quasicrystals.

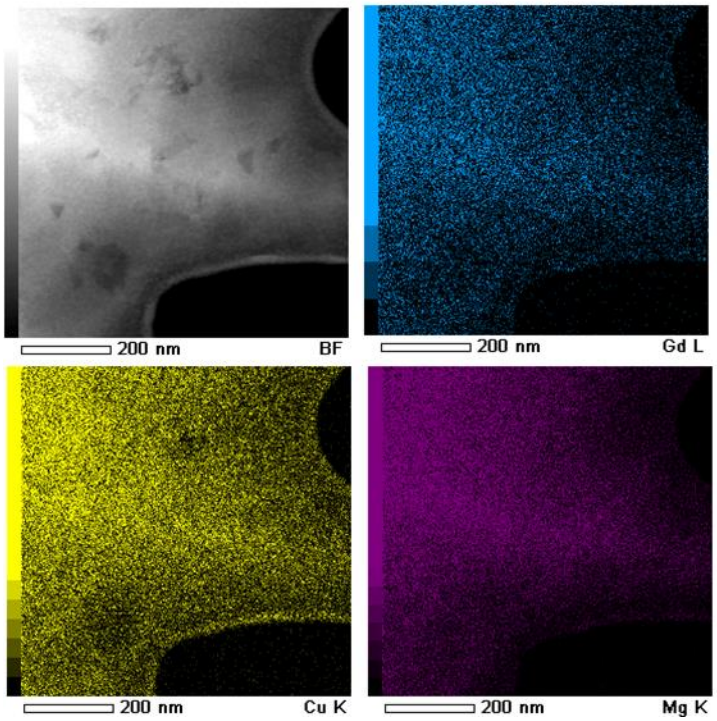

Figure 67 HAADF-STEM and EDS maps of samples heat treated for 16 hours at 453 K. Maps showing the distribution of elements throughout the sample. The elemental maps indicate that the ternary phases formed through heat treatment have a composition close to that of the bulk alloy.

Identification of the equilibrium phases in the ternary Mg-Cu-Gd system has been conducted by Zheng [103]. In that work the phases are identified based on EDS measurements of their chemical compositions. The ternary phase identified by Zheng as Mg_4CuGd (τ_5), the crystal structure of this phase has not been identified. The EDS measurements of composition of the phase are 66 at.% Mg, 17 at.% Cu and 17 at.% Gd, with an error of $\pm$1 at.%. The compositional mapping in Figure 67 shows no sign of compositional segregation after heat treatment. The τ_5 phase is of a similar composition to the alloy of this study ($Mg_{60}Cu_{29}Gd_{11}$) if the majority of the sample has transformed to the τ_5 phase this would explain the homogeneous nature of the elemental maps in Figure 67. Rizzi *et al.* [27] have also investigated ternary phases in the Mg, Cu, Gd system by EDS. They found Mg_2Cu_9Gd and $MgCu_2Gd_2$ to be the equilibrium phases, but the structures of these phases have not been fully characterised, with only the chemical compositions identified. It is unlikely that these are the phases forming in this study due to the lack of segregation of Cu and Gd that would be evident if Mg_2Cu_9Gd and $MgCu_2Gd_2$ are to form [27].

5.2.8 Quenched-in nuclei

In Zr-, Ni- and Fe-based metallic glasses, the formation of quasicrystals with similar composition to the matrix has been linked to icosohedral short-range order within the glass. The stability of the icosahedra made the likely formation of quasicrystals preferable to the formation of crystalline phases. This mechanism is supported by reverse Monte Carlo modelling and EXAF studies [81]. The quasicrystals found in this study have similar composition to that of the matrix, with a slight decrease in the amount of copper in the quasicrystal when compared with the matrix (Figure 65). The short-range order of Mg-Cu-RE type glasses is reported as Cu-centred tricapped trigonal prisms and bicapped square antiprisms [83]. The work that investigated the atomic structure of Mg-Cu-RE alloys used Y as the rare earth whereas the alloy in this study is Gd. Molecular dynamic simulations conducted by Gao *et al.* [84] on a $Mg_{60}Cu_{30}Gd_{10}$ BMG determined the atomic structure of the glass is icoshedral in nature. The formation of quasicrystals from the amorphous matrix in the present work supports this finding.

The change in rare earth may cause a change in local atomic ordering. Further investigation of the atomic structure of the Mg-Cu-Y glass will be needed to confirm this. The formation of icosohedral quasicrystals from the glass matrix indicates that the energy barrier to the formation of quasicrystal is likely to be lower than that required to form either Mg_2Cu or Cu_2Gd phase, which are reported previously as the primary crystalline phases. Based on the mechanism of metastable quasicrystal formation put forward by Kelton and Gangopadhyay *et al.* [81, 82] and the prediction of an icosahedral ordering by molecular dynamic modelling [84], the formation of metastable quasicrystals under the application of strain indicates that the atomic clustering of Mg-Cu-Gd is likely to be icosahedral.

The stability of the quasicrystals is investigated by subjecting the rolled samples to a heat treatment at 453 K for 16 hours. After the heat treatment, the glass had completely crystallised. A diffraction pattern taken over a large area (Figure 66) shows no amorphous rings remaining. The diffraction pattern in Figure 66 contained no diffraction spots that correspond to any of the quasicrystalline phase. There are several different crystalline phases present within the heat treated samples and their identities are a potential area of future work.

5.2.9 Multiple roll passes

As the deformation given to the sample increases, the temperature at which the crystallisation occurs (T_x) drops. The size of the SCLR and the size of the exothermic peak of crystallisation change with changes in strain through rolling. With an increase in total strain applied to the sample, the size of the crystallisation peak decreases and the T_x also decreases. The change in the DSC curves suggests a change in the structure of the amorphous material.

During plastic deformation of BMGs, it has been shown that dynamic crystallisation can occur [74]. When partial crystallisation is observed to occur, then the formability of the BMG decreased. If the volume fraction of the crystalline particles remained below 25% then the effect on formability is small [104]. Nano-crystals may be forming within the glass below the detectable limit of XRD.

Deformation of BMGs has been shown to cause embrittlement due to the loss of free volume [105]. The loss of free volume can also occur when heat treatment is below the T_g point and for Mg-based glasses embrittlement can occur at room temperature [91, 106, 107]. The free volume within a BMG can be measured by the size of the deflection in the DSC curve that occurs just before T_g. This deflection of the curve is caused by the annihilation of free volume within the glass. When a BMG has its temperature raised to within the SCLR, the free volume returns due to thermal activation. The free volume that has been created by heating the BMG to within the SCLR can be retained if the cooling rate back down through T_g is sufficiently high. If the cooling rate from the SCLR is slow, all free volume is lost from the amorphous structure [91]. The cooling rate used to return the BMG to below T_g, then controls the free volume remaining within the structure. Due to the thin cross-sections of the rolled samples, the cooling rate after rolling is sufficient to preserve the free volume within the amorphous structure. This can be seen Figure 68, the extent of the deflection in the DSC curve remains relatively constant for all levels of reduction. This shows that rolling can be used without the resulting embrittlement caused by loss of free volume. Retention of free volume and the slight lowering of the T_x point suggest that it should be possible to undertake a second forming operation after rolling, as long as the new T_x is not exceeded. This is found to be the case (as can be seen in Figure 69) where a second roll pass has been performed on a sample that has been rolled previously.

Due to the large strains that are possible when rolling BMGs, it would be unlikely that two roll passes would be required to achieve the needed gauge. However, the ability to perform a second shape-forming operation after rolling may be required. The use of blow forming of a BMG has been investigated by Schroers *et al.* [108], in which blow forming is shown to be a viable production method for producing shapes from a thin sheet precursor, preferably sub 1 mm. It is difficult to produce large pieces with a sub 1 mm thickness through conventional casting. The ability to roll BMGs will allow sheet to be formed at sub 1 mm thicknesses, which can be then fed to a second forming process such as blow moulding.

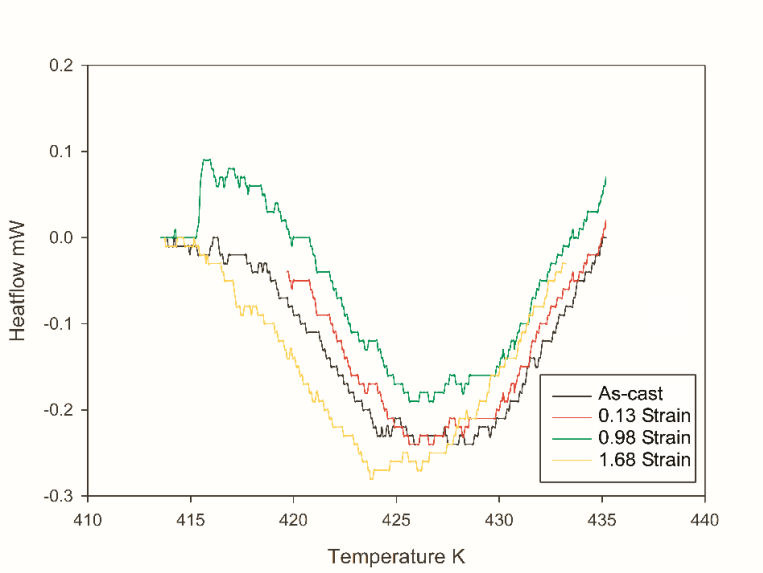

Figure 68 DSC of rolled samples in region prior to the T_g point figure showing that free volume remains relatively constant in samples with up to 1.68 rolling strain. The T_g point is between 425 and 430 K.

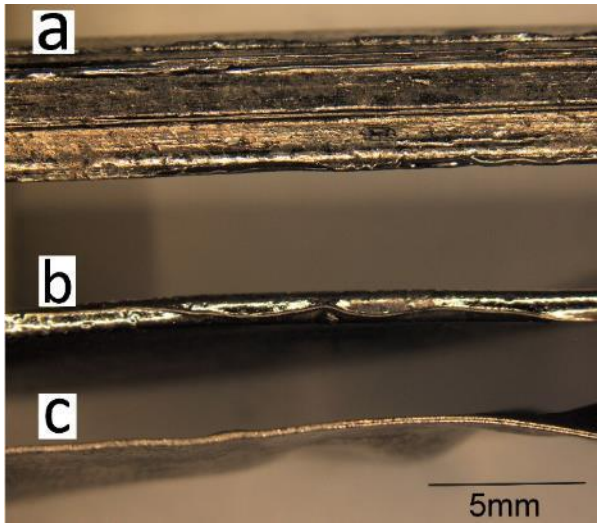

Figure 69 Photographs of the side-on view of (a) an as-cast bar 4mm thick from the Rotocaster, (b) first roll pass of sample at 453 K reduced to 1 mm thick, and (c) second roll pass of sample at 453 K reduced to 0.5 mm thickness.

5.3 CONCLUSIONS

Rolling is an industrial scale process that is used to produce large amounts of sheet material. This chapter describes the effect of rolling conditions on the resultant structure of $Mg_{60}Cu_{29}Gd_{11}$ bulk metallic glass. The effects of strain, strain rate and temperature are studied. The following conclusions can be made:

1. **The application of strain to a bulk metallic glass causes the amount of order within the system to increase**.

   In this work XAFS has been used to study the change in short-range order prior to the beginning of crystallisation. The amount of order within the glass increases with an increase in strain. During rolling at high strain rate a temperature spike occurs, allowing a metastable quasicrystalline phase to form. The devitrified structure of the glass is the same in both high and low strain rate samples. This indicates that the structural change occurring is similar in both samples. The structural change that is occurring is likely to be the formation of nano-scale quasicrystals. The temperature spike that occurs during rolling at high strain rate allows these quasicrystals to grow to a detectable size. The rapidity of the heating and cooling spike during deformation does not provide sufficient time for the quasicrystals to transform to other phases. XAFS indicates that the amount of order within an amorphous sample increases with an increase in the amount of strain.

2. **When the alloy is subjected to strain, a change in the crystallising phases occurred. The cause of this change is the formation of icosahedral clusters within the amorphous matrix. The formation of quasicrystals within an amorphous matrix suggests that the atomic structure of the BMG is likely an icosahedral cluster type.**

   Under conditions of high strain and high strain rate, the quasicrystals form, which is observed by TEM. The presence of quasicrystalline particles in an amorphous matrix indicates that the formation of quasicrystalline phase has a lower energy barrier than the primary crystalline phases reported previously. The formation of quasicrystals of similar composition to the amorphous matrix has been shown to be an indication of icosahedral type ordering within glass. The experimental results obtained from this project supports the model developed from first principles calculations [84] that the atomic structure of Mg-Cu-Gd type BMG is an icosahedral cluster type.

3. **When rolling BMGs at a particular temperature within the SCLR, the amount of strain introduced and the strain rate imposed during the rolling process should both be minimised to reduce the amount of ordering and to prevent dynamic crystallization.**

   If the BMG is rolled in a manner that preserves its amorphous structure then second forming operation can be carried out on the rolled sample. This two stage forming operation will allow a cast block to be rolled to the desired thickness and then fabricated into the final part via a subsequent second forming process, such as blow or press forming.

5.4 FUTURE WORK

Detailed study on the effect of strain on crystallised phases: In this work it is found that the phases that form upon heat treatment of strained samples are different to those of unstrained samples. A more detailed study of this phenomenon would provide interesting results on the effect of the state of the amorphous matrix and the crystallisation mechanism. The practical outcome of a study into the effect of strain on phase formation could be that, if the change in phases causes an improvement in mechanical properties, then the production of parts within the SCLR, followed by a crystallisation heat treatment to improve mechanical properties, may result in a new pathway for BMG alloys to reach the market place.

6 PRODUCTION AND FRACTURE OF $Mg_{60}Cu_{29}Gd_{11}$ BMG/ ALUMINIUM LAMINATES

6.1 INTRODUCTION

In this Chapter the design and mechanical properties of laminate structures will be described. To gain a property baseline the constituent material properties are measured.

As the nature of this work is to develop scalable processing, roll bonding will be used as a manufacturing method to produce BMG / aluminium laminates. The bond between the aluminium and the BMG will be characterised and the strength of the bond measured. The mechanical properties of the laminates will be measured via three-point bending and Charpy impact testing. The effect of hybrid material make up on the mechanical properties will be explained.

The failure mechanisms of the hybrid material are characterised using SEM to image the fracture faces of both the aluminium and BMG after three-point bending tests. The interface between the aluminium and the BMG is also characterised, and the failure through delamination, tearing of the aluminium and fracture of the BMG is observed.

6.2 RESULTS AND DISCUSSION

The following section details specific physical properties of the constituent glass are measured. From this data the target design for the laminate can be developed. For a laminate of a brittle material and a ductile material to be stable in bending the layer thickness of the brittle material should be less than twice the plastic zone size (R_p) of the material.

6.2.1 Plastic zone size of $Mg_{60}Cu_{29}Gd_{11}$ bulk metallic glass

One method of estimating the R_p value in a brittle material is the overloaded Vickers hardness indenter method [109]. In this method a Vickers hardness test indent is conducted at a load that causes the test material to crack. The length of the crack is measured, from the centre of the indent to the tip of the crack, from which the plastic zone size R_p of the material can be calculated. In Figure 70 cracks can be seen that have developed at the edge of the Vickers indent. Figure 71 shows the overloaded Vickers hardness indent with radial cracks developed from each corner of the hardness indent. The primary radial crack is labelled ‘a’ and a secondary radial crack has developed on the top left hand corner of the indent and is labelled ‘b’. The secondary radial cracks release additional stress from the system that would otherwise be used to propagate the primary crack, other sources of error in this technique are the development of subsurface and edge cracks around the indent. This method of determining the R_p size gives an indicative size measurement suitable for use in this application. The development of secondary cracks, such as those highlighted in Figure 70 (edge cracks) and Figure 71 (secondary radial cracks), can result in an under estimation of approximately 10% when calculating the toughness values of brittle materials. The development of secondary radial

cracks can be easily seen and when measuring the crack lengths for calculation of the R_p size the primary cracks with a secondary crack associated with it can be removed from calculations. The presence of subsurface cracks cannot be detected prior to measurement of the crack length, as such the limitations of this technique should be noted and not used to give high precision measurement of R_p size.

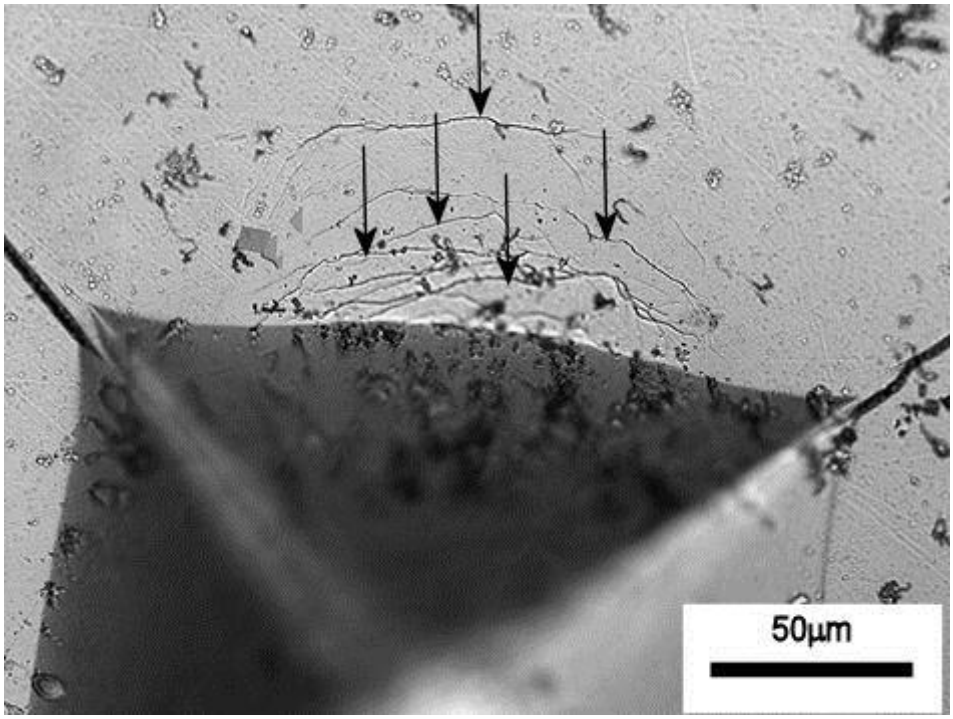

Figure 70 Reflected light micrograph showing secondary cracks, marked with arrows, at the edge of an overloaded Vickers hardness test on $Mg_{60}Cu_{29}Gd_{11}$ BMG.

An overloaded hardness test indent is shown in Figure 71. The crack length is measured from the centre of the indent to the tip of the crack, an average value is taken from 12 indents, the larger the crack length the lower the toughness of the material. The Young's modulus value of the glass is measured in a separate test by an UMIS nano-indenter. The measurements from the Vickers hardness tests are given in Table 15, from each of these data sets a K_c value of the glass is calculated using the relationship given by [109].

$$K_c = X\left(\frac{E}{H}\right)^{1/2}\frac{P}{a^{3/2}} \quad (14)$$

Where X = calibration constant, E = Young's modulus, H = Vickers hardness, P = applied load, a = radial crack length. The calculated K_c values are given in Table 16. The resulting effective K_c is obtained by averaging these values, and this is determined to be 0.56 MPa·$m^{0.5}$ with a standard deviation value of 0.081. From this average K_c value one can calculate the plastic zone size of the material, using Eqn. 15, with a yield strength of 800 MPa which can be obtained from a conversion from the Vickers hardness value [110], the plastic zone size is calculated to be 80 nm. This value is in agreement with reported values for the plastic zone size in other Mg-based glasses that are between 80 and 100 nm [111, 112]. If the 10% error in calculating the K_c value is taken into account the R_p size falls between 60 and 90 nm.

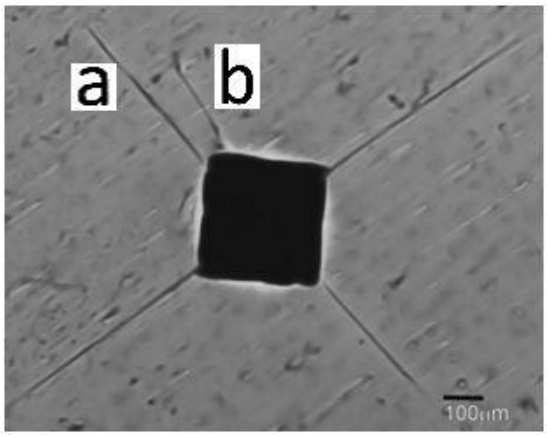

Figure 71 Optical image of an overloaded Vickers hardness indent. By measuring the crack length the plastic zone size of the material can be calculated. (a) Main crack measured for toughness calculation. (b) Secondary radial crack that causes errors in this method, by providing an additional release of stress. The conditions for this indent are (P) 10 kg for load, (E) Young's modulus 50 GPa (H) Vickers hardness 250 H_V measured from the indents preformed on the samples and (a) the radial crack length of 400-500 μm.

Table 15 Crack length and hardness measurements taken from overloaded Vickers hardness test.

Diagonal length of indent for H_V (μm)				**Crack length, from centre of indent to crack tip (μm)**	
Diagonal 1	**Diagonal 2**	**Average**	**Vickers hardness number H_V**	**Crack 1**	**Crack 2**
283	267	275	245	500	463
271	264	267.5	260	476	436
272	272	272	250	398	438
281	275	278	239	404	432
270	274	272	250	480	466
267	275	271	250	410	427
269	276	272.5	250	504	418
273	272	272.5	250	425	459
276	276	276	243	452	403
269	267	268	258	442	392
275	278	276.5	243	474	415
269	280	274.5	247	477	440

Table 16 Calculated K_c values using values given in Table 15.

0.297805505	0.334207538	0.485430349
0.302113432	0.344628135	0.296489902
0.410950199	0.35596118	
0.420323685	0.380128376	0.349366783
0.310278688	0.324365703	0.498323923
0.393041146	0.369804329	0.414067385
0.2883819	0.38181183	0.30268024
0.372417781	0.331814053	0.313210443
0.296914316	0.284889789	
0.349333219	0.414944458	0.3564062
0.340252012	0.407384973	0.355834594
0.325296976	0.397077604	0.328409852
0.317014619	0.357830902	0.379617572
0.356454313	Mpa/m	
0.051218488		

$$R_p = \frac{1}{2\pi}\left(\frac{K_c}{\sigma_y}\right)^2 \quad (15)$$

To construct a plate, of thickness D, that is stable in bending the plastic zone size must exceed D/2 [113, 114].

$$R_p > \frac{D}{2} \quad (16)$$

A laminate can be considered a collection of individual plates and as such in order to produce a material that is stable in bending the lamellar spacing for the BMG layer would need to be in the order of 65 nm in thickness, maximum.

6.2.2 Flexural bending properties of $Mg_{60}Cu_{29}Gd_{11}$ monolithic bulk metallic glass

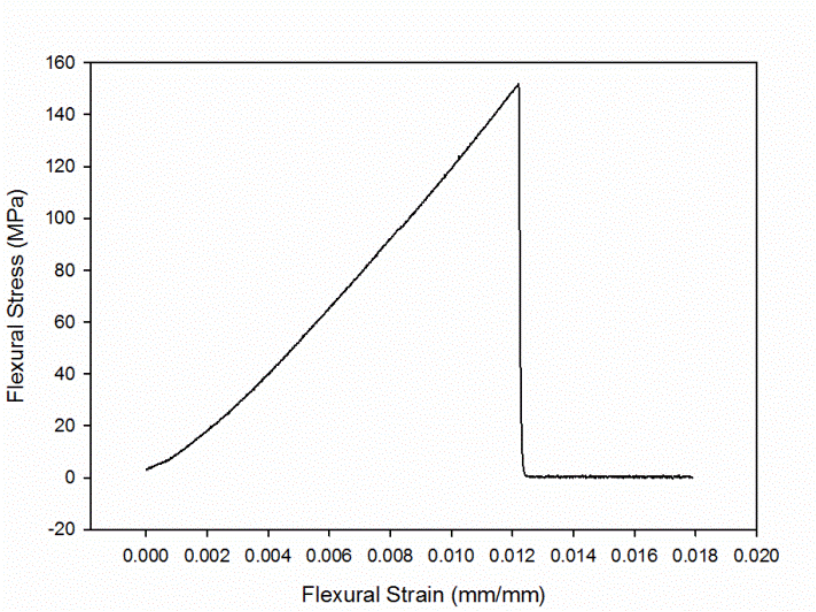

Figure 72 Flexural stress strain graph for monolithic glass sample failed catastrophically at a stress of 152 MPa and 0.012 strain.

Magnesium BMGs are a brittle material with a limited plastic elongation and a minimal toughness. In three-point loading a monolithic bar of $Mg_{60}Cu_{29}Gd_{11}$ failed after a flexural strain of 0.012 at a flexural stress of 150 MPa when measured with a 2 mm thick plate. In Figure 72 the three-point bend for a monolithic glass test is shown. During testing the stress builds rapidly and ends with a sudden catastrophic failure.

In addition, to measure the impact energy absorption of the glass Charpy impact tests are conducted. The energy absorption of the monolithic glass is also low, with an energy absorption value of 0.02 joules.

6.2.3 Bonding of Al and BMG through isothermal rolling

To improve the properties of the glass in bending and impact barriers to shear band movement need to be introduced to the structure of the material. The chosen method to introduce second phases is the construction of laminates by bonding BMG to aluminium. Roll bonding is selected as the most suitable production method to fabricate the laminated composites, the primary reason for this is that roll bonding is a scalable process that will facilitate large sheets of material to be formed. The need for a scalable process is one criteria used throughout this work, with the use of twin roll casting and planar flow casting to produce the amorphous material. For successful bonding the surfaces of both materials are required to be cleaned thoroughly before rolling to remove any surface contamination and this is done mechanically by linishing. Before roll forming, sandwich preforms are made by stacking alternating layers of aluminium and BMG foils, with the stacks being held with aluminium fasteners before bonding to prevent twisting and/ or translation movement of the layers relative to each other. Isothermal rolling, at a temperature within the SCLR of the metallic glass being bonded, is conducted to prevent fracture of the metallic glass interlayers.

For a laminate to be produced, the rolling of Al and BMG has to be performed within the limits set for the successful rolling of BMG. In addition to operating within the rolling processing window a reduction of at least 40% is needed to achieve bonding between BMG and Al foil.

A SEM image of the interface region between the metallic glass (upper) crystalline metal substrate (lower) can be seen in Figure 73(a). The interface between the BMG and the Al layer shows no sign of the formation of intermetallic phases or of diffusion of Al into the BMG layer, the composition line scan taken across the interface, shown in Figure 73(b), indicates a sharp transition with little diffusion. The transition occurs over 2 μm with a volume interaction zone of approximately 1.3 μm this transition is as sharp as can be measured by this technique. The lack of diffusion suggests that it is the interlocking associated with the conforming of the BMG onto the Al surface that is the major bonding mechanism in this case. In Figure 73(a) the lighter contrast BMG layer is shown keying into an irregular feature on the Al surface, as indicated by the arrows. Co-extrusion has been used to bond a $Mg_{65}Cu_{25}Gd_{10}$ BMG to an aluminium alloy and the bonding mechanism reported in that work is the same as found in this study [115].

The BMG is evaluated after rolling and after bonding to determine if either the rolling or the bonding process had resulted in the formation of any crystalline phase fraction. The work shown in Chapter 5 highlighted the change in structure that occurs during rolling and under the conditions used in the roll bonding trials the BMG should remain fully amorphous. The XRD scans in Figure 74 show that the glass remains fully amorphous after both the rolling and the bonding to the aluminium.

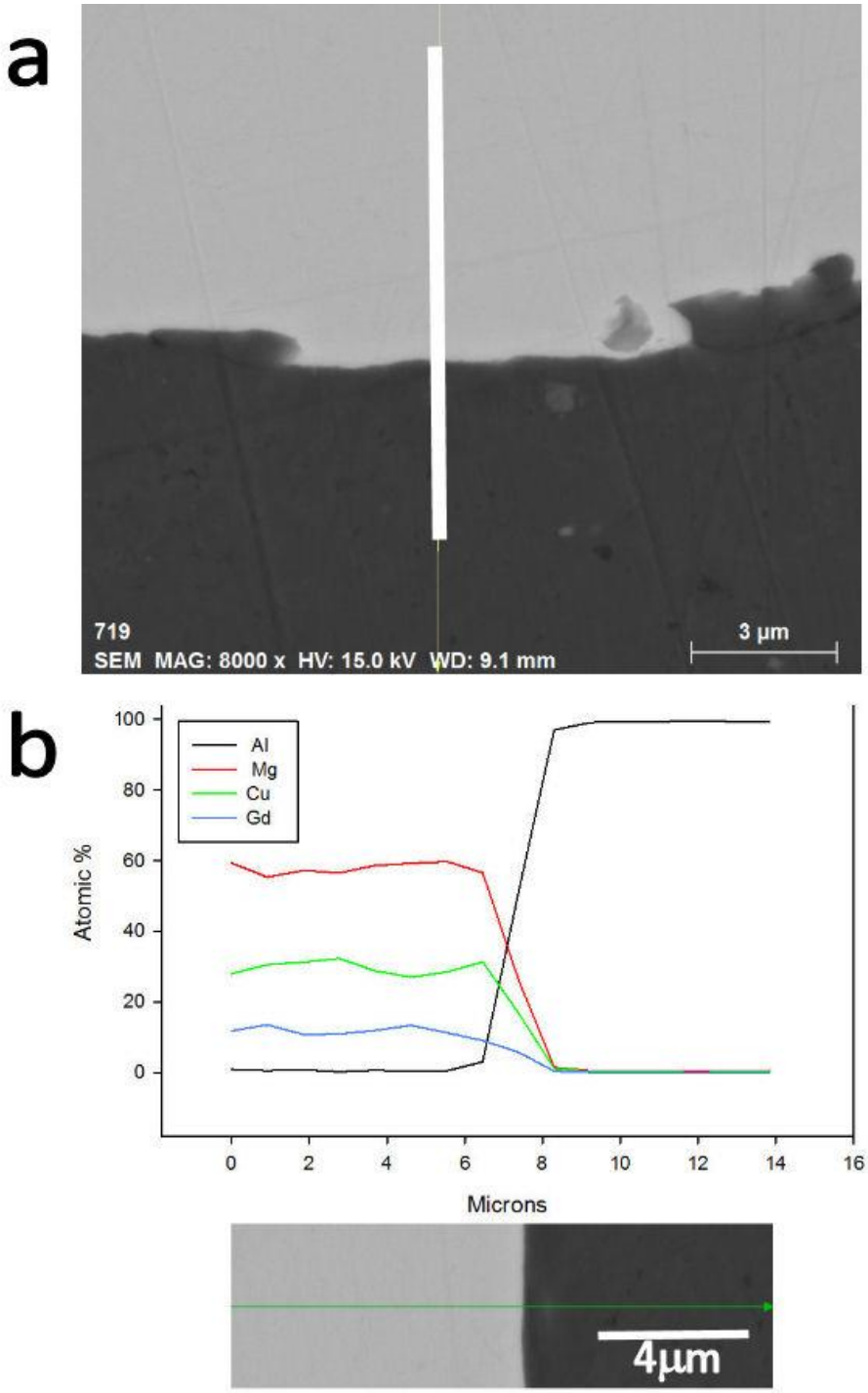

Figure 73 (a) Backscattered electron SEM image showing a portion of the BMG (upper) -Al (lower) interface after rolling. The presence of intermetallic phases, or signs of diffusion in and across the interface, is not visible; the white line is the location of the SEM composition scan. (b) Composition line scan across the interface there is no sign of diffusion across the interface. Spot size of the scan is 1.3 µm.

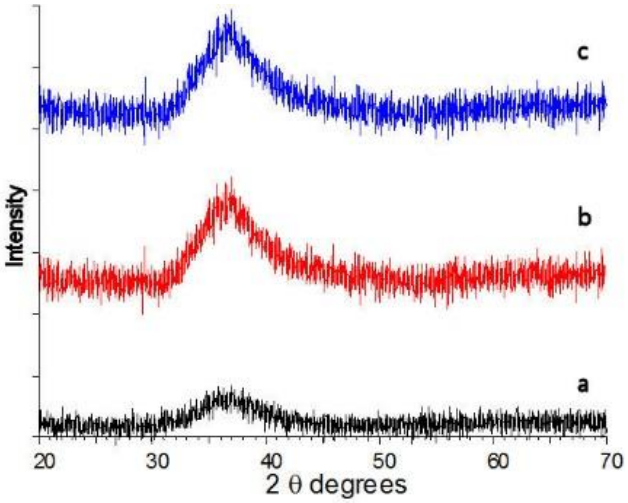

Figure 74 XRD traces of BMG sheet in (a) as-cast, (b) as-rolled rolled at 463 K, 1.62 ε and 0.7 s^{-1}, and (c) as-bonded state rolled during bonding rolled at 463 K, 1.62ε and 0.7 s^{-1}.

After a single roll pass the layer thickness of the BMG layer within the laminate is above 10 microns. The criteria to produce a plate that is stable in bending is $2R_p > D$, with D being the plate thickness. The R_p value calculated by the overloaded Vickers hardness test gives a value of 90 nm. Therefore, to create a laminate stable in bending, the lamalae spacing has to be reduced to sub 180 nm. To reduce the layer thickness to the nanometre range a second roll pass on the laminate is trialled. Accumulative roll bonding has been demonstrated as a method that can produce laminates with fine lamallae spacing in alloy systems that have similar mechanical properties between the layers [116-118]. On the second roll pass the BMG layer underwent catastrophic failure Figure 75(a) shows a backscattered electron image of a BMG-Al laminate material. In this image it can be seen the laminate structure is maintained during rolling with intimate bonds between the Al and BMG layers. Figure 75(b) shows the hybrid structure after a second roll pass, in this image the BMG layer has begun to fail and the laminate structure is destroyed. Characterisation of the material via XRD after rolling and after bonding confirmed the amorphous structure of the material is retained in both the as-rolled and as-bonded conditions Figure 74 Therefore, as the amorphous phase is stable during bonding, gross crystallisation cannot be the reason for the degradation of the BMG layer on the second roll pass. The catastrophic failure of the laminate structure is a common occurrence in accumulative roll bonding processes. This breakdown is due to the difference in mechanical properties between the constituent materials causing one layer to deform to a larger amount than the other [119, 120]. This differential deformation occurred in the initial bonding process but because the layers are not effectively bonded and therefore they could move relative to one another.

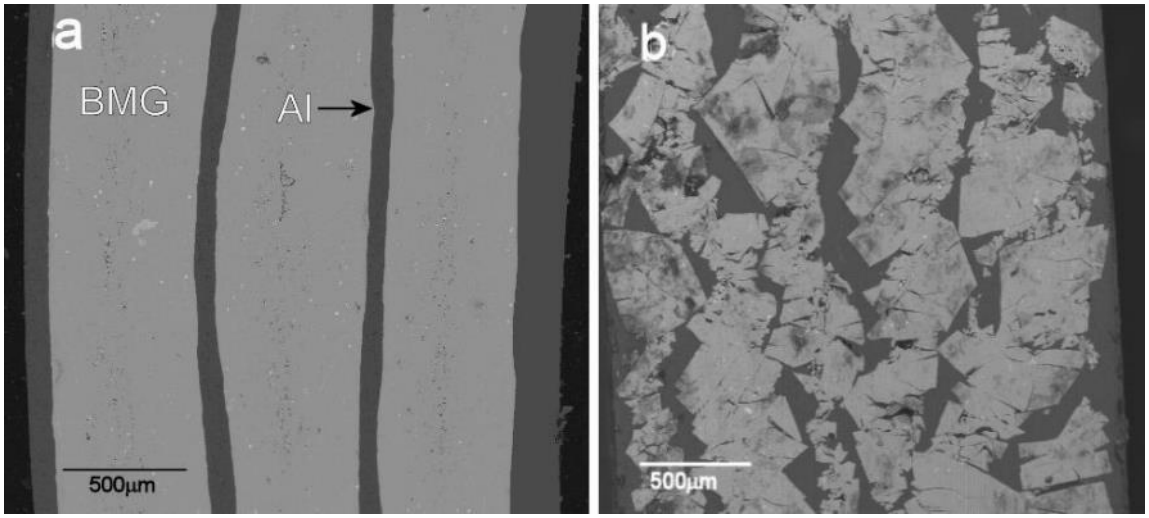

Figure 75 Backscattered electron SEM images showing cross-sections of BMG-Al laminate structures (a) produced via a single-pass roll bonding, and (b) after a second roll pass showing the disintegration of the BMG layers. Regions of darker grey contrast are the Al layers, and the light grey layers are the BMG.

6.2.4 Bond strength between Al and bulk metallic glass

The metal substrate is cleaned mechanically before rolling to remove any surface contamination and the linishing marks resulting from the cleaning process can be seen in Figure 76(a), as indicated by the arrows. The BMG layer deformed into the surface features of the Al layer on the micron length scale, as indicated by the arrows in Figure 76(b). The roughened surface gives a greater surface area and features that allow the BMG to key into the aluminium improving the bond strength. To measure the strength of the bond between the BMG and the aluminium layer the bonded area is subjected to a lap shear test. During the lap shear test the fracture occurred through the metallic glass layer not at the bond interface. The location of the fracture indicates that the weak point of the structure is the bulk material properties of the BMG not the interface join between the BMG and the aluminium. The fracture surface of the BMG is typical of a brittle material with large cleavage facets evident. The presence of shear bands on a cleavage facet of the BMG, as well as a clean fracture surface, indicates the brittle nature of the failure, as shown in Figure 76(c).

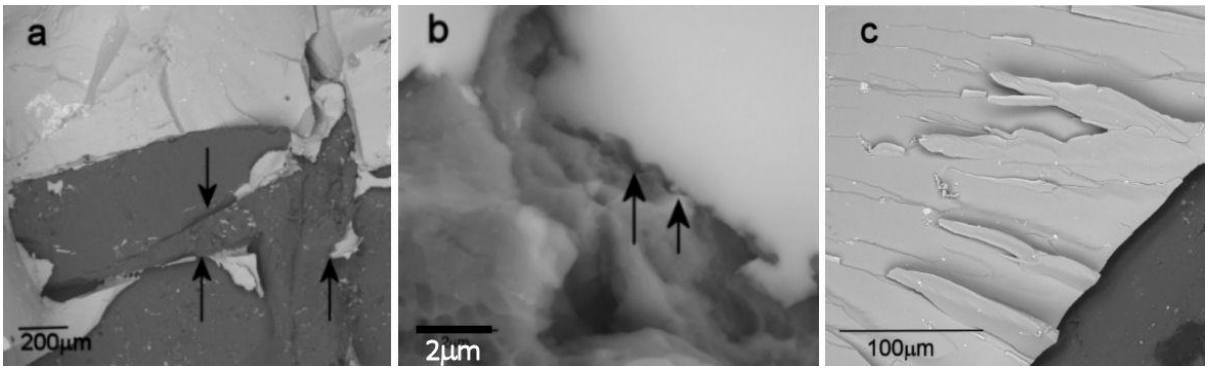

Figure 76 (a) Backscattered electron SEM image showing the fracture surface of a lap shear tested sample. Dark contrast area is the Al layer, and the grey area is BMG. (b) Higher magnification SEM image of the BMG layer conforming to micron scale surface features on the Al layer. (c) Fracture face of lap shear tested sample indicating brittle failure of the glass layer.

6.2.5 Mechanical properties in bending of laminates

To evaluate the mechanical properties of the BMG-Al laminates three-point bending test are performed. Performance in bending provides a combined measure of the compressive and tensile properties of a material, failure can either occur in compression at the inner surface of the test bar or in tension on the outer surface of the bar.

From the three-point bend test the flexural stress and flexural strain of samples are calculated using the following formulas:

Flexural stress is given by,

$$\sigma = \frac{3FL}{2bd^2} \quad (17)$$

Flexural strain is given by,

$$\varepsilon = \frac{6Dd}{L^2} \quad (18)$$

Where F = force applied to sample, L = span length of the sample, b = sample width, d = sample depth and D = deflection of sample.

Three-point bends tests are conducted on monolithic BMG and laminates that contained 2-, 3- and 4-layers of BMG. As the number of layers in the laminate increases, the thickness of each layer is reduced, as the total test piece thickness is kept constant. Figure 77(a) shows that as the number of layers in the hybrid structure is increased, the three-point bending performance is altered. The curve for the monolithic sample undergoes elastic deformation with increasing load until sudden catastrophic failure at the point of first fracture. In contrast, the laminated samples display staggered drops in load as each glass layer fractures sequentially, shown for the 4-layer BMG laminate in Figure 77. The maximum flexural stress value obtained for a laminate is 242 MPa, as compared to 150 MPa obtained for a monolithic glass sample. The flexural strain values for the laminates are also improved by over a 100% from 0.012 to 0.03, Figure 77. The three-point bend tests are stopped after the final BMG layer fractured, the aluminium layers did not fracture and they are able to support some load, in the 2- and 3-layer BMG laminate plateaus can be after large load drops which are regions where the aluminium is supporting the load.

In bending tests the point of maximum stress is the outer curved surface of the test bar. When the critical stress is obtained in the outer surface a shear band propagates from the outer surface and because of the lack of barriers to shear band movement in BMGs the sample fails catastrophically as seen in the curve for the monolithic sample. However, when barriers to shear band movement are present in the material, such as the Al layer in a laminate, the propagation of the shear band is halted and the test sample does not fail catastrophically. For the laminate that contains two BMG layers, the load curve follows that of the monolithic sample until the critical stress is reached at the outer surface of the test specimen. In the monolithic sample catastrophic failure occurs; however, in the two-layer laminate the Al layer stops the shear band movement and the sample did not fail, Figure 77. The sample fractures when the critical stress is reached at the outer surface of the second BMG layer. The stress level for the two-layer laminate does not return to zero on fracture of the BMG layers as some load is still carried by the Al layers which did not fracture during testing.

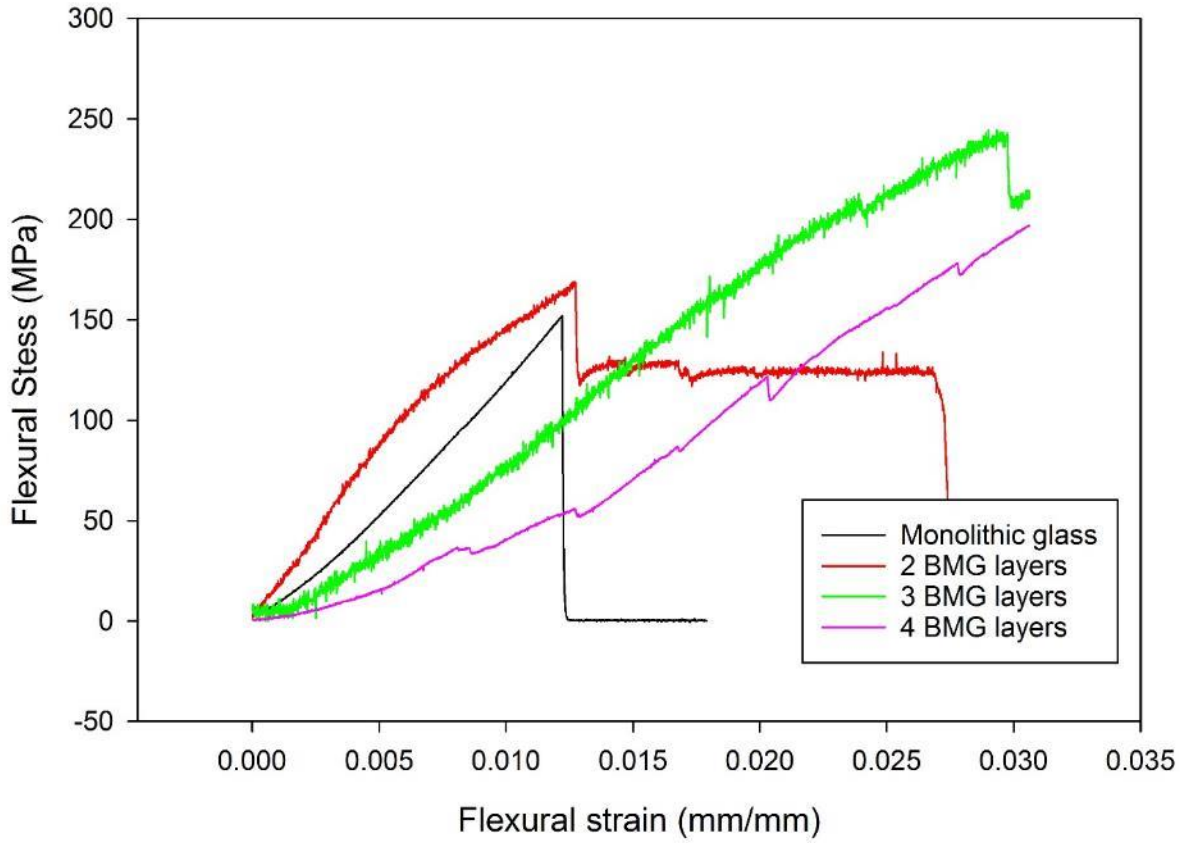

Figure 77 Displacement vs. load curves for three point bend tests. Each step in the curve represents the point at which BMG layer fractures. Fracture points in 4-layer BMG laminate corresponding approximately to the fracture points in the monolithic glass and 2-layer BMG laminate.

The values for maximum flexural stress and the flexural strain at the major strain drop off are given in Table 17.

Table 17 Flexural stress and strain values for BMG aluminium laminates.

Sample	Flexural stress (MPa)	Variance ±	Flexural strain at load drop off	Variance ±
Monolithic BMG	150	2	0.0122	0.0001
2 layer	170	7	0.0128	0.0003
3 layer	242	5	0.0298	0.001
4 layer	195	16	0.0305	0.003

Within the three-point bend test stress strain curves the typical shape is a build-up of stress until fracture is initiated at the outer radius of the bending sample. Fracture occurs when the stress on the outer layer reaches the tensile strength of the layer. The crack then propagates with no barriers until it encounters the soft aluminium layer.

Because accumulative roll bonding is unsuccessful, to reduce the thickness of the BMG layer further, the initial thickness of the monolithic BMG material is reduced. This is done by using planar flow casting to produce ribbon from the $Mg_{60}Cu_{29}Gd_{11}$ alloy. The maximum number of layers that could

be made with 1 mm thick monolithic BMG starting material is a 4-layer laminate, the use of planar flow casting (PFC) foil feedstock allowed laminates with a larger number of layers to be produced.

By using planar flow cast ribbon with a starting thickness of 100 μm it is possible to achieve a BMG layer thickness of 20 μm, (Figure 78). Although this is a large reduction from the layer thickness produced with the TRC feedstock it is still well above the target thickness of 180 nm, which is set by the R_p value of the BMG.

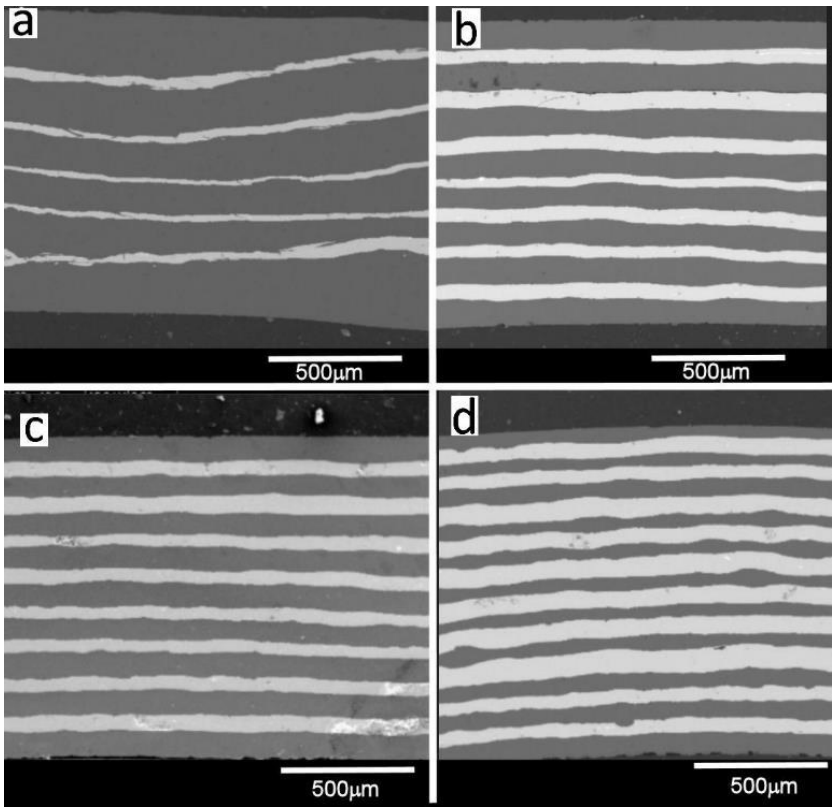

Figure 78 Backscattered electron SEM images showing cross-sections of laminates prior to testing. As the layers of BMG increase the layer thickness of Al decreases increasing the vol.% of BMG. The dark layers are the aluminium, with the lighter layers BMG. (a) 5 BMG layers, (b) 7 BMG layers, (c) 8 BMG layers, and (d) 10 BMG layers.

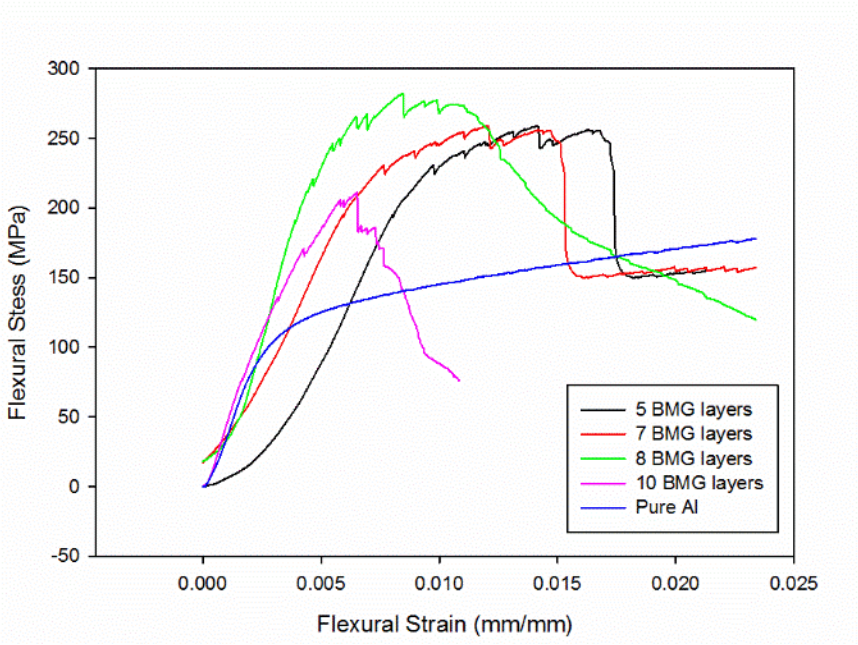

Figure 79 Flexural stress vs. flexural strain curves from three-point bend test of BMG aluminium laminates made with melt spun ribbon precursor, with pure aluminium as a reference.

When testing the laminates it is shown there is variance at the reported flexural stress values at point of fracture (Table 18). When calculating the flexural stress values the total thickness of the sample is used. In BMG aluminium laminates it is not the outer surface that is carrying the stress it is the outer BMG layer. The position of the outer BMG layer varies from each different laminate composition, in Figure 78 it can be seen the position of the outer BMG layer relative to the surface of the laminate varies from composition to composition and even within a single sample. In the 5 BMG layer laminate shown in Figure 78(a) the distance from the surface of the laminate to the BMG layer varies. The change in the position of the load bearing BMG layer causes the effective d value in Equation 17 to change.

Table 18 Flexural stress and strain values of BMG aluminium laminates produced from melt spun ribbon and Al foil.

Sample	Flexural Stress (MPa)	Variance ±	Flexural Strain at load drop off	Variance ±
5	260	15	0.017	0.008
7	258	5	0.015	0.0001
8	281	25	0.011	0.002
10	210	16	0.007	0.004
Pure Al	177	2	NA	

The transition from TRC feedstock to PFC feedstock occurred at the 4-layer BMG point, with the 5-layer laminate and greater being made from planar flow cast ribbon. When comparing the flexural stress values from the TRC feedstock to that from PFC, the ratio of aluminium to BMG initially increases with the 5-layer BMG laminate being predominantly aluminium, Figure 78(a), whereas the 3-layer laminate is predominantly BMG, Figure 73(a). Even with the higher level of the high strength BMG the 3-layer laminate has a lower flexural strength (242 MPa, Figure 77) than the 5-layer (281

MPa, Figure 79) laminate with a lower volume of BMG. This is due to the higher number of barriers to crack propagation in the 5-layer BMG laminate. This increase in stress with increase in layers was found by Tariq *et al.* [16] who tested laminates of Zr based BMG plates bonded with an epoxy bonding layer. They found that increasing the number of layers in a laminate increases the load to fracture.

In Figure 77 the stress / strain curve of the 4-layer BMG laminate test is shown, in which four steps in the curve can be seen, each of these corresponds to a glass layer fracturing. The fracture of the first two layers line up with the fracture points of the monolithic and 2-layer laminate, respectively, this is an indication that the fracture point of the outer layer is due to the stress at the outer surface, which is consistent for all the samples tested, Figure 77.

The flexural strain values in the three-point bend test for laminates have improved by over an order of magnitude when comparing the monolithic BMG to a 4-layer BMG laminate. As the thickness of a BMG layer reduces the amount of strain that it can accommodate prior to fracture increases. The plastic zone at the front of a crack tip, R_p, is a value that can be used to measure the toughness of a material. If the R_p value exceeds D/2 where D is the sample thickness, the sample will then be stable in bending [22]. If the laminate layer thickness could be reduced to meet this criterion for stable bending, then a large thickness composite that is stable in bending could be produced. For a brittle BMG such as Mg-Cu-Gd type BMGs the layer thickness will need to be in the sub-micron range. Reducing layer thickness in a laminate to sub-micron scales has been done by magnetron sputtering which resulted in layer thickness of 200 nm [121]. The laminate produced with layer thicknesses of 200 nm displayed bending ductility at room temperature even though their constituent BMGs (Zr- and La-based) are brittle when tested in the mm size region [41]. However, for this work one of the stated aims is to develop a process that could be used to produce a cheaper product that is produced via scalable technologies, this precludes the use of sputtering to achieve thin layer thickness.

6.2.6 Fracture through bending in laminates

After three-point bending the fracture surface of the laminates is inspected. It can be seen in the cross-section shown in Figure 80, that the failure of the aluminium layers is ductile in nature displaying significant necking (i.e. the layer labelled, a whilst the BMG layers the layer labelled b) show a sharp flat facetted fracture surface indicating a typical brittle failure. Moreover, during fracture de-lamination between the aluminium and BMG layers occurred over the majority of the fracture surface along or close to the interphase interfaces, Figure 81.

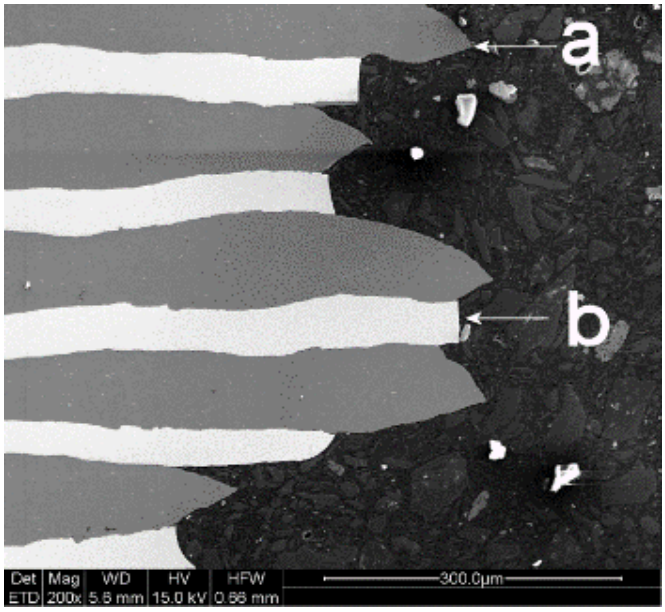

Figure 80 Backscattered electron SEM image of cross-section of the fracture face of a laminate showing ductile failure of the aluminium layer and brittle failure of BMG. The aluminium layer is labelled a, and the BMG layer b.

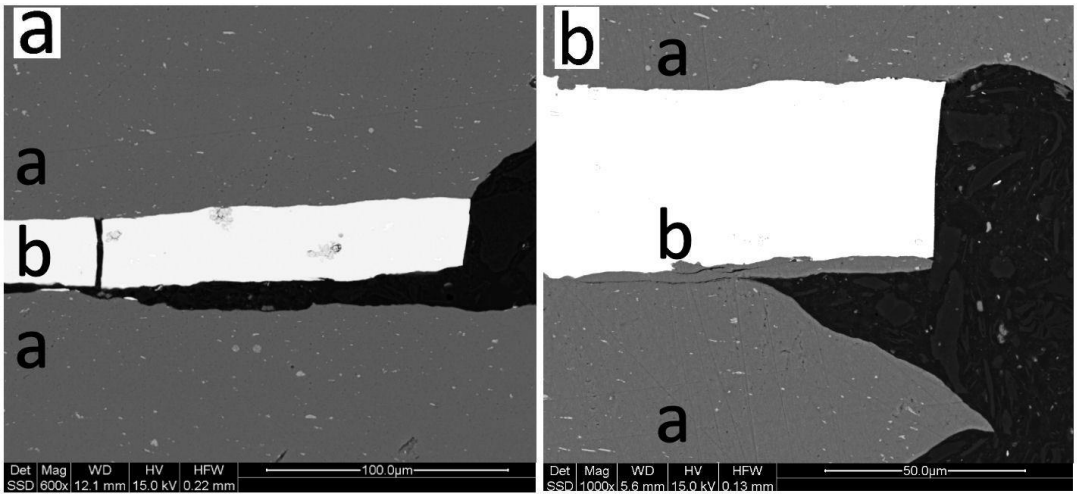

Figure 81 Backscattered electron SEM images showing cross-sections of the de-lamination which occurs through the interface or through the aluminium layer aluminium layer labelled a BMG layer labelled b. (a) De-lamination occurring through the aluminium layer. (b) Fracture occurring through the interface.

The de-lamination of the layers can occur on both the upper and lower side of the BMG layer. The outer BMG layer in Figure 82 shows de-lamination from both upper and lower surfaces. As one moves through the laminate the side of de-lamination varies from top to bottom of the BMG layer.

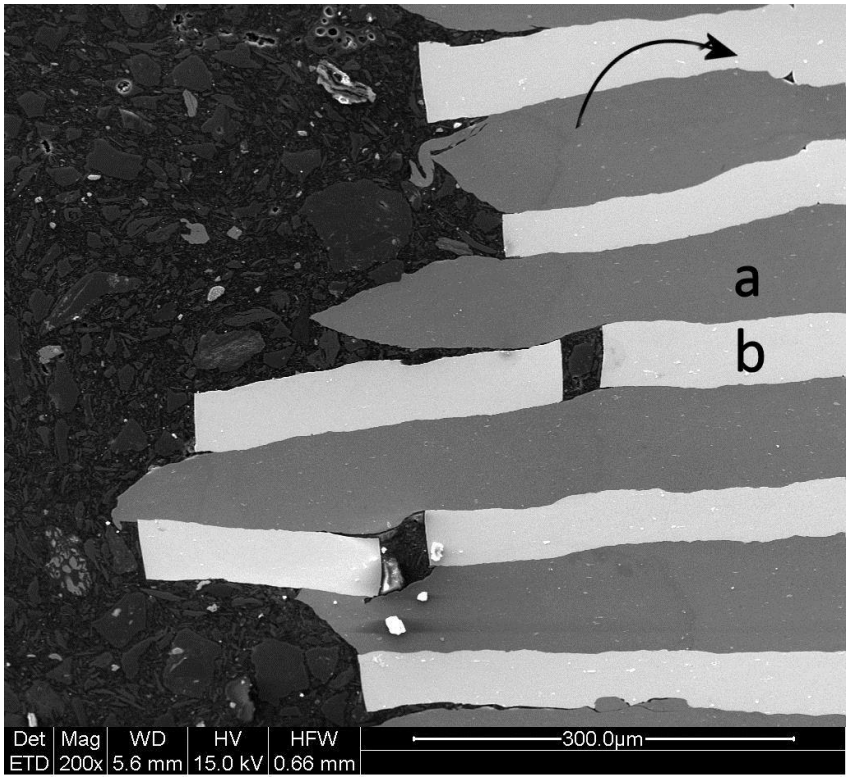

Figure 82 Backscattered electron SEM image showing cross-section of a laminate after fracture of three-point bend. Aluminium layer labelled a, BMG layer b. Arrow shows direction of bending, the top of the image is the outer radius of the bend test.

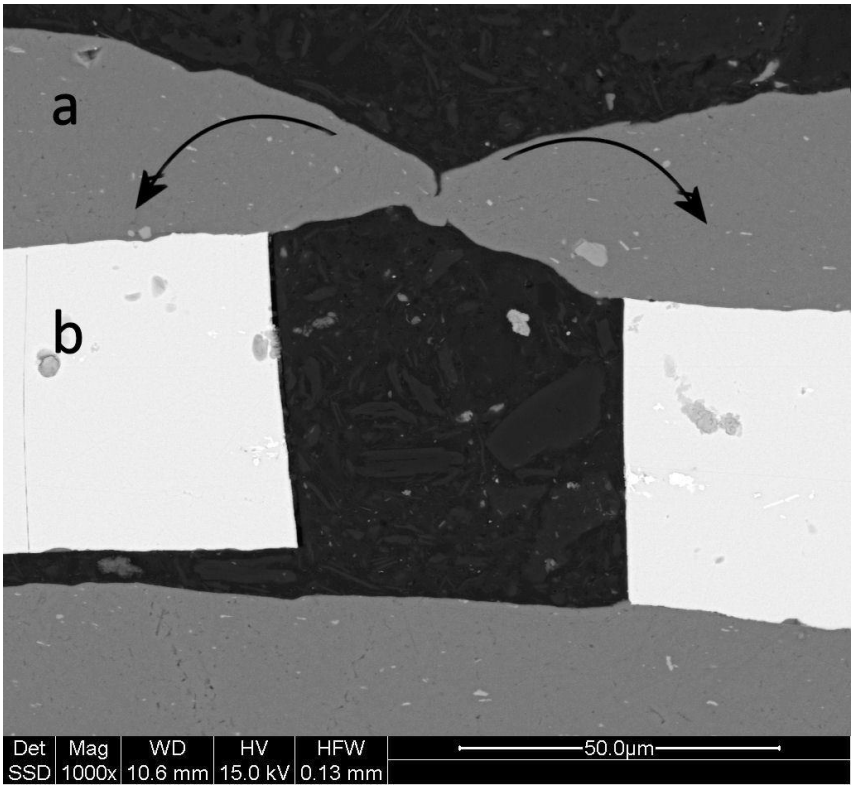

Figure 83 Backscattered electron SEM image showing cross-section after a bend test. The BMG, b, has failed, while the ductile Al layer, a, remains intact.

In Figure 83 the bend test is stopped midtest. In this image the ductile deformation of the aluminium can be seen by the elongation and necking of the upper aluminium layer. Whereas the BMG layer, that is located under the aluminium layer, has failed before the aluminium layer on the outer radius of the bend test specimen, where the stress is concentrated, has fractured. Compare this to the sharp line fracture in the BMG layer, the BMG layer shows no sign of deformation at all.

Stopping the three-point bend test prior to complete failure allows the observation of the failure development. Figure 84 shows the BMG layer does not only fail at the point of fracture on the aluminium layer. On each BMG layer there are secondary points of failure that occur away from the apex of the bend, prior to failure of the aluminium layer the BMG layer is still being placed under stress. If this stress exceeds the UTS of the BMG a secondary fracture will occur. In the example shown in Figure 84 two aluminium layers and the BMG layer closest to the inside radius of the bend is yet to fail

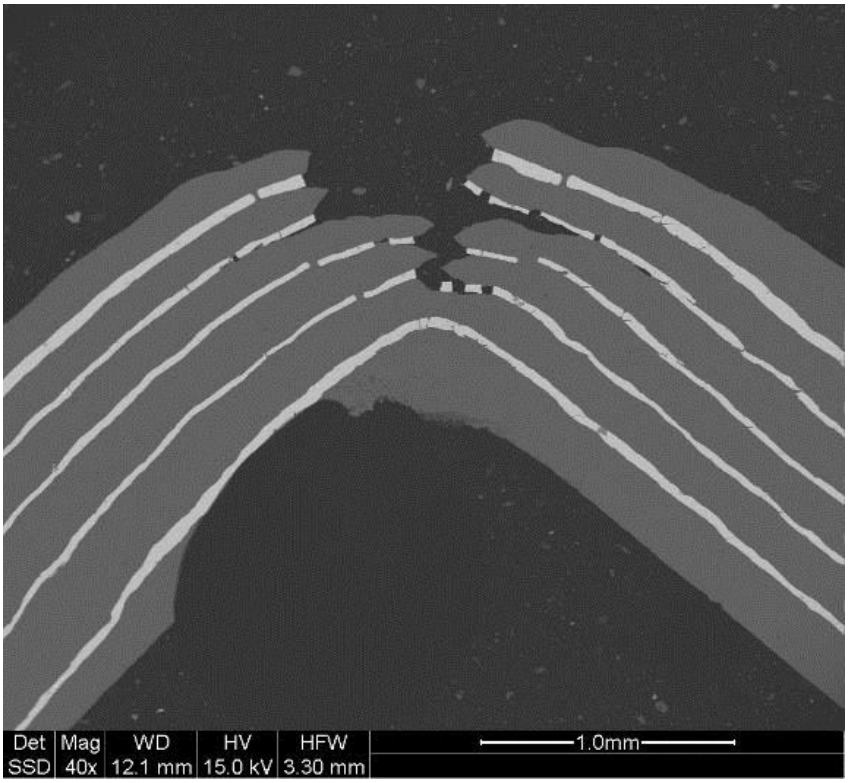

Figure 84 Backscattered electron SEM image of a laminate that has undergone three-point bend testing with the test interrupted prior to complete fracture.

6.2.7 Impact energy

Along with the strength of a material another important mechanical property is the toughness of a material. The toughness measures the amount of energy that a material can absorb during fracture. The Charpy impact test is a high strain rate test that can provide comparative values for the toughness of a material. By conducting Charpy impact tests on laminates a comparative measure of the toughness of various laminate structures and monolithic samples can be achieved.

It can be seen in Figure 85(a) that with an increase in the number of layers in the laminate the impact energy required to fracture the sample increases. When the amount of Al within the laminate is expressed as a volume fraction the relationship with impact energy becomes linear, Figure 85(b). The improvement in impact energy is significant in laminate materials. The addition of 10 vol.% of Al to the structure increases the fracture toughness by two orders of magnitude from 0.02 J for the monolithic glass to 2.5 J for a 15-layer (7BMG / 8Al) laminate. The impact values for the laminates tested are given in Table 19.

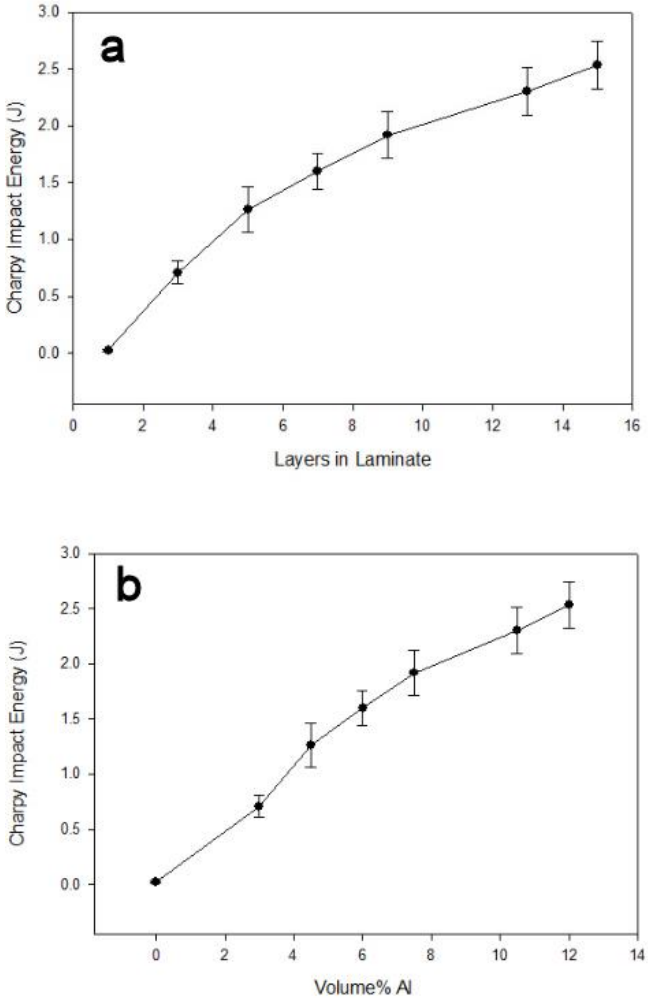

Figure 85 Variation of Charpy impact energy of BMG–Al laminate as a function of (a) number of layers within the 2 mm thick laminate, and (b) volume fraction of Al in the laminate.

Table 19 Charpy impact energy values for laminates.

Layers in laminate	Volume fraction Al (%)	Impact energy (Joules)
Monolithic glass	0.0000	0.0200
3	3.0000	0.7100
5	4.5000	1.2600
7	6.0000	1.6000
9	7.5000	1.9200
13	10.5000	2.3000
15	12.0000	2.5300

6.2.8 Fracture of constituent materials

The fracture surface of a monolithic glass is that of a brittle material, the fracture surface is microscopically flat and featureless with no signs of dimpling, Figure 86(a). The fracture surface of the aluminium foil is that of a ductile material with a high degree of dimpling and ridging, Figure 86(b). The soft ductile aluminium will act as a barrier to crack propagation stopping the catastrophic failure of the composite.

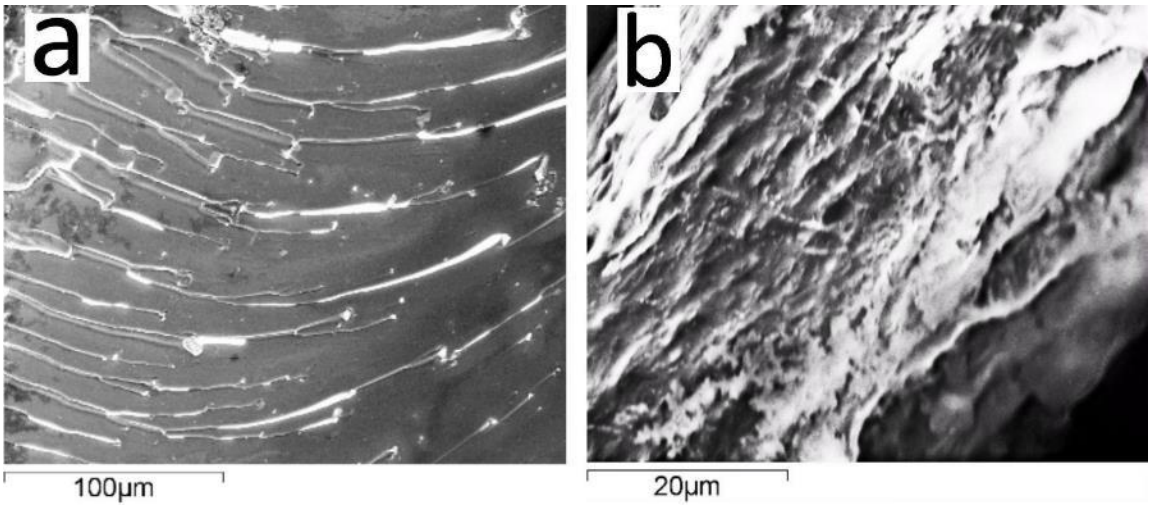

Figure 86 Backscattered electron SEM images showing the fracture surface of the constituent materials. (a) Brittle fracture surface of monolithic BMG. (b) Fracture surface of aluminium foil.

6.2.9 Fracture through Impact in laminates

The Charpy impact test is a high strain rate test that can provide comparative values for the toughness of a material. By conducting Charpy impact tests on laminates, a comparative measure of the toughness of various laminate structures and monolithic samples can be achieved. When the laminates are tested, the Al layer closest to the impact site did not fracture but deformed around the hammer. For the outer layers of Al foil within the laminate, the bond strength with the BMG is high enough that the Al deformed and fractured rather than delaminating from the metallic glass and deforming around the impact hammer.

The Al layers within the laminate act as a barrier to the propagation of cracks through the material. As can be seen in Figure 87a, the dark contrast Al thin layers prevented the transmission of a crack from one BMG layer to the next (as indicated by the arrows). The glass layer on the left hand side of the image has many cracks, as this is the closest to the site of impact of the hammer during the test. This area of high damage is stopped at the first Al layer. In subsequent glass layers the numbers of lateral cracks are reduced and are stopped at the interface with the neighboring Al foil layer.

Energy is absorbed by the Al layer in the laminate by stopping the propagation of cracks through the deformation and/or ductile failure of the Al foil. Breaking of the interfacial bond between the foil and the BMG can also absorb energy during fracture. In some areas of the laminate structure, de-lamination of the BMG from the metal foil is observed at the fracture face, as can be seen in Figure 87(b) (as indicated by the arrow), however, de-lamination did not occur throughout the entire sample, in Figure 87c the bond between the Al foil and BMG remained sound (as indicated by the arrow).

The Al foil layer fails in a ductile manner with many ridges and dimples on the fracture face, whereas the glass fails in brittle manner. The fracture face of the glass is smooth with no signs of deformation having taken place. The difference in fracture mechanisms between the glass and the metal foil is illustrated in Figure 87(b) and (c).

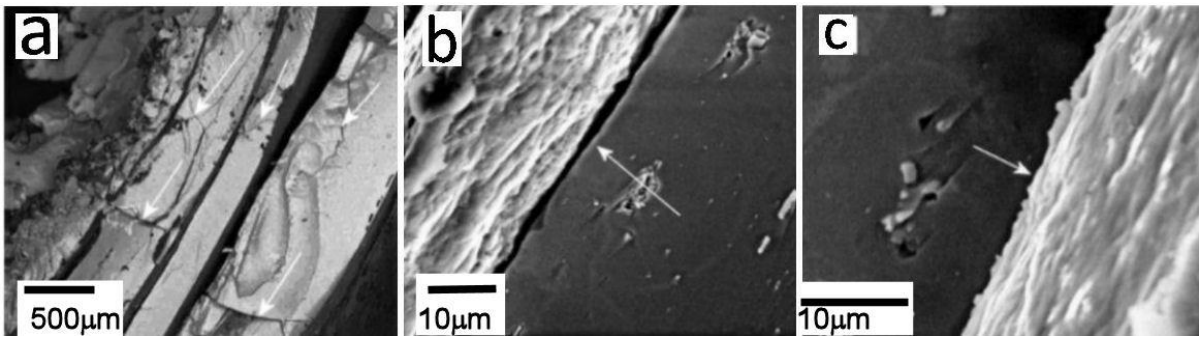

Figure 87 Backscattered electron SEM images showing (a) cracks within the BMG layers that are stopped by the presence of an Al interlayer, (b) fracture face of laminate showing interfacial de-lamination, and (c) fracture face on laminate without interfacial de-lamination.

6.3 CONCLUSIONS

Bulk metallic glass alloy strips are strong yet brittle at room temperature with a maximum flexural stress of 150 MPa and a maximum flexural strain of 0.012. The Charpy impact energy to fracture for $Mg_{60}Cu_{29}Gd_{11}$ amorphous alloy is 0.02 joules. The failure mechanism is sudden catastrophic failure along a single shear band due to the lack of microstructural barriers to shear band movement. To improve the toughness of the BMG strip laminates are produced, the laminates are produced via roll bonding.

The following conclusions can be made:

1. **For bonding to occur between the BMG and Al layers the reduction of the preform must exceed 40%**.

   The as-bonded structure shows no sign of intermetallic formation or diffusion across the bond. The bond is due to the conforming of the BMG to the aluminium surface. To achieve the required amount of plastic deformation to conform the two materials together a minimum reduction of 40% must be achieved.

2. **The critical crack size of the BMG is found to be in the nanometre range**.

   To construct a laminate that is stable in bending the maximum lamellae spacing has to be 2 times larger than the critical flaw size. By the use of overloaded Vickers hardness test method the critical flaw size was found to be 100 nm. This means that the lamellae spacing for a stable in bending laminate should be no more than 200 nm.

3. **The flexural stress and flexural strain of BMG-Al laminates are improved when compared with monolithic glass properties**. **The flexural stress and strain values are increased by at least 90%.**

   The flexural stress values for laminates compared with the monolithic glass improve by 90% from 150 MPa to 290 MPa. The flexural strain values improve by over 100% from 0.012 to 0.03. The variable that has the greatest influence on the increase in stress and strain values is the number of layers in the laminate not the volume percentage of the constituent materials. The dominance of the number of layers is due to importance of barriers to shear band and crack propagation stopping sudden catastrophic failure.

4. **The Charpy impact energies increase by two orders of magnitude from 0.02 to 2.5 joules.**

   The increase in Charpy impact energy is proportional to the amount of aluminium within the structure. The brittle nature of BMGs does not absorb any energy during failure through impact. To produce a material with high flexural stress and flexural strain combined with high impact toughness, the number of BMG layers should be maximised while maintaining low BMG layer thickness and the amount of aluminium in the structure should be maximised to toughen the laminate.

7 CONCLUSIONS

The aim of this work is to develop scalable processes to produce flat products from Mg-based BMG and laminates of both BMG and aluminium. As a part of developing these processes the effects of processing conditions on microstructure and mechanical properties are determined. It is concluded that TRC or PFC, and its combination with rolling within the SCLR, are suitable methods for producing both 100% amorphous sheet and laminates of BMG and aluminium. The combination of high cooling rate and continuous production made TRC a scalable production method for amorphous sheet with thicknesses between 1 mm and 3 mm. The addition of aluminium to form a laminated hybrid improved mechanical properties of the sheet in terms of flexural stress, flexural strain and impact energy. This is due to the introduction of barriers to shear band propagation through the sheet.

The following conclusions can be made in this project:

1. **To produce 100% amorphous sheet through twin roll casting the exit temperature of the sheet must be within the supercooled liquid region of the alloy. The cooling rate applied to the melt must be high enough to bypass the nose of the crystallisation curve on the CCT diagram.**

   Twin roll casting is explored for producing BMG sheet from two Mg-Cu-RE alloys. It is found that twin roll casting could be used to successfully produce BMG sheet with a thickness between 1 and 3 mm. To produce high quality BMG sheet via TRC the following criteria must be met:

   (1) The temperature of the sheet exiting the rolls must be within the SCLR of the alloy.

   (2) The thickness of the sheet as the melt temperature passes the T_{nx} isotherm must be below the critical thickness of the alloy being cast.

   (3) The contact time of the melt with the rolls is rate controlling. The required contact time could be achieved by varying the contact length and the roll speed as long as criteria 1 and 2 are not violated.

   By following these three processing rules, TRC can be applied to other BMG systems. The development of continuous production could allow BMG sheet to be used as a structural material or as a feedstock for subsequent forming operations.

   To meet these criteria and to produce amorphous sheet the key variables are the contact time between the rolls and the melt, and the cooling rate applied to the melt. The cooling rate is controlled via the heat transfer to the rolls from the melt, this can be changed by changing the material of the roll but in this study the roll material is kept constant. The cooling rate is maximised by the use of Cu-Be alloys rolls. The other variable that controls the cooling rate is the thickness of the strip. It is shown during the experiments that to produce 100% amorphous strip the thickness of the alloy as it passed the T_{nx} point should be held below the critical thickness of the alloy as measured by wedge casting using the same mould material as the roll.

   To control the temperature of the strip as it exits the roll the contact time between the roll surface and melt has to be controlled. The combination of contact length and roll rotation speed control the time that the melt is in contact with the roll. By increasing the contact length the roll speed can be increased to maintain the contact time as a constant. This can be done until the increase in contact length causes the increase in material thickness to be such that the cooling rate is now insufficient to bypass the crystallisation point on the CCT diagram.

2. **Rolling of $Mg_{60}Cu_{29}Gd_{11}$ bulk metallic glass within the supercooled liquid region can be done successfully. The conditions under which rolling is conducted influence the structure of the rolled material. This can be in the macro form where the formation of cracks can occur and in the atomic scale where rolling conditions influence the local ordering. Under the rolling condition of a strain rate 13.63 s^{-1} and a strain of 1.67 metastable quasicrystals form within the amorphous matrix.**

   The stability range of the $Mg_{60}Cu_{29}Gd_{11}$ BMG as a function of time and temperature is determined by the use of XRD on heat treated samples to locate the time at which the first signs of crystal formation occurred at a specific temperature. This data is determined to provide an estimation of the residence time at the temperature that can be tolerated without crystallisation being initiated prior to rolling taking place.

   Temperature change during rolling is an understood phenomenon when rolling crystalline metals and there are established equations to calculate this increase. When calculating the temperature increase that occurs during rolling the standard equations do not consider the large change in viscosity that occurs within the SCLR of BMGs. For the standard rolling calculations to accurately predict the adiabatic heating conditions the change in viscosity that occurs in BMGs needs to be considered.

   Within the adiabatic heating calculation the τ value is dependent on the viscosity of the material being rolled, for crystalline metals this value does not change dramatically with temperature, however, for magnesium BMGs the change can be four orders of magnitude. The dramatic change in viscosity causes the difference between the calculated and measured temperature rise to be 370 K. For a more accurate prediction of the temperature increase during rolling $d\eta/dT$ should be introduced to the formula to account for the change in viscosity with change in temperature. The change in viscosity with temperature formula will be different for different BMG.

   The formation of macro defects is influenced by the combination of strain, strain rate and rolling temperature. For temperatures between 483 and 463 K defect free rolling occurred at all strains and strain rates tested. In rolling trails, conducted at 443 K, the influence of both adiabatic heating and conductive heating is observed to affect the quality of the rolled sheet. At a strain rate of 16.33 s^{-1}, the domination of adiabatic heat transfer increases the temperature of the work piece and the samples can be rolled without the formation of surface defects. At strain rates lower than 0.7 s^{-1}, the domination of conductive heat transfer from the heated roll surface to the work piece allows the sample to be rolled defect free.

   XAFS are used to study the change in short-range order prior to the beginning of crystallisation. The order within the glass increased with an increase in strain. Strained sample which are subjected to heat treatment produced a different mix of phases upon crystallisation that that produced from samples in the as cast state. The devitrified structure of the glass is the same in both samples rolled with high and low strain rate. During rolling at high strain rate a temperature spike occurs, allowing metastable quasicrystals to form. This indicates the structural change occurring is similar in both samples. The structural change that is occurring is likely to be the formation of nano-scale crystallites. The temperature spike that occurs during rolling at high strain rate allows for these crystallites to grow to detectable size. The rapidity of the heating and cooling spike during deformation does not allow sufficient time for the crystals to transform to other phases.

   In-situ heat treatment XRD experiments are conducted and it is found the application of 1.67 rolling strain to the glass at a strain rate of 0.7 or 13.63 s^{-1} resulted in a change of the crystallised

phases when compared with the as-cast sample. The change in the crystalline phase content after a sample has been rolled at both low and high strain rates indicates that structural change during strain. XAFS indicated the order within an amorphous sample increased with an increase in the strain applied to the sample.

Under conditions of high strain and high strain rate, the nano crystallites grow to form quasicrystalline particles. The presence of quasicrystalline particles in an amorphous matrix indicated that the formation of quasicrystalline phase had a lower energy barrier than that of the primary crystalline phases, which is different from a previous report. The formation of quasicrystals of a composition similar to the amorphous matrix has been shown to be an indication of icosahedral type ordering within glass. This supports the recent first-principles calculation results [84] that the atomic structure of Mg-Cu-Gd type BMG is an icosahedral cluster type.

When rolling BMGs, at a particular temperature within the SCLR, in order to reduce the amount of ordering and to prevent dynamic crystallization the amount of strain introduced and the strain rate imposed during the rolling process should both be minimised. If the BMG is rolled in a manner that preserves its SCLR then second forming operations can be carried out on the rolled sample. This two-stage forming operation will allow for a cast block to be rolled to the desired thickness and then fabricated into the final part via a subsequent second forming process, such as blow or press forming.

3. **The formation of laminates composed of aluminium and $Mg_{60}Cu_{29}Gd_{11}$ bulk metallic glass improves the flexural stress, flexural strain and Charpy impact energy values compared with the properties measured from monolithic glass.**

Bulk metallic glass alloy strips are strong yet brittle at room temperature with a maximum flexural stress of 150 MPa and a maximum flexural strain of 0.012. The Charpy impact energy to fracture for $Mg_{60}Cu_{29}Gd_{11}$ amorphous alloy is 0.02 joules. The failure mechanism is sudden catastrophic failure along a single shear band due to the lack of microstructural barriers to shear band movement. To improve the toughness of the BMG strip, laminates are produced, the laminates are produced via roll bonding. From these investigations the following is found:

(1) For bonding to occur between the BMG and Al layers the reduction on the preform must exceed 40%. The as bonded structure showed no sign of intermetallic formation or diffusion across the bond. The bond is due to the conforming of the BMG to the aluminium surface.

(2) The critical crack size of the BMG is found to be in the nanometre range. To construct a laminate that is stable in bending the maximum lamellae spacing is double the critical flaw size. To produce nanometre scale lamellae spacing accumulative roll bonding is trailed. The accumulative roll bonding process is not successful for this purpose.

(3) The flexural stress, flexural strain and Charpy impact energy properties of BMG-Al laminates are improved when compared with monolithic glass properties. The flexural stress values for laminates compared with the monolithic glass is improved by 90% from 150 MPa to 290 MPa. The flexural strain values are improved by 100% from 0.012 to 0.03. The variable that had the greatest influence on the increase in stress and strain values is the number of layers in the laminate not the volume percentage of the constituent materials. The dominance of the number of layers is due to importance of barriers to shear band and crack propagation stopping sudden catastrophic failure.

(4) The Charpy impact energies increased by two orders of magnitude from 0.02 to 2.5 joules. The increase in Charpy impact energy is proportional to the amount of aluminium within the structure. The brittle nature of the magnesium BMGs did not absorb any energy during failure through impact. To produce a material with high flexural stress and flexural strain combined with high impact toughness, the number of BMG layers should be maximised while maintaining low BMG layer thickness and the amount of aluminium in the structure should be maximised to provide sufficient toughness to the laminate.

8 PUBLICATIONS

1. Production and mechanical properties of roll bonded bulk metallic glass / aluminium laminates, **D. East**, M. Gibson, D. Liang, J.F. Nie, Metallurgical and Materials Transactions A: 2013, vol. 44, issue 5, pages 2010-2020.
2. High performance bulk metallic glass/carbon nanotube composite cathodes for electron field emission, P. Hojati-Talemi, M. Gibson, **D. East**, G. Simon, Applied Physics Letters: 2011, vol. 99, article 194104.
3. Amorphous magnesium sheet produced by twin roll casting, **D. East**. M. Kellam, M. Gibson, A. Seeber, D. Liang, J.F. Nie. Materials Science Forum: 2010, vols. 654-656, pages 1078-1081.
4. Devitrification studies of $Mg_{60}Cu_{29}Gd_{11}$ bulk metallic glass. **D. East**, M. Reid, M. Gibson, R. Dippenaar, R. O'Donnell; Materials Science Forum: 2010, vols. 654-656, pages 1082-1085.

9 REFERENCES

[1] Ashby MF, Greer AL. Metallic glasses as structural materials. Scripta Materialia 2006; 54:321.

[2] Laws KJ, Gun B, Ferry M. Influence of Casting Parameters on the Critical Casting Size of Bulk Metallic Glass. Metallurgical and Materials Transactions A 2009; 40A:2377.

[3] Lee JG, Lee H, Oh YS, Lee S, Kim NJ. Continuous fabrication of bulk amorphous alloy sheets by twin-roll strip casting. Intermetallics 2006; 14:987.

[4] Lee JG, Park SS, Lee SB, Chung HT, Kim NJ. Sheet fabrication of bulk amorphous alloys by twin-roll strip casting. Scripta Materialia 2005; 53:693.

[5] Hofmann DC, Suh J-Y, Wiest A, Duan G, Lind M-L, Demetriou MD, Johnson WL. Designing metallic glass matrix composites with high toughness and tensile ductility. Nature 2008; 451:1085.

[6] Chen HS, Turnbull D. Formation, stability and structure of palladium-silicon based alloy glasses. Acta Metallurgica 1969; 17:1021.

[7] Peker A, Johnson WL. A highly processable metallic glass: $Zr_{41.2}Ti_{13.8}Cu_{12.5}Ni_{10.0}Be_{22.5}$. Applied Physics Letters 1993; 63:2342.

[8] Li F, Guan S, Shen B, Makino A, Inoue A. High specific strength and improved ductility of bulk $(Mg_{0.65}Cu_{0.25}Gd_{0.1})_{(100-x)}$ Ti_x metallic glass composites. Materials Transactions 2007; 48:3193.

[9] Xu YK, Xu J. Ceramics particulate reinforced $Mg_{65}Cu_{20}Zn_5Y_{10}$ bulk metallic glass composites. Scripta Materialia 2003; 49:843.

[10] Jang JSC, Chang LJ, Young JH, Huang JC, Tsao CYA. Synthesis and characterization of the Mg-based amorphous/nano ZrO_2 composite alloy. Intermetallics 2006; 14:945.

[11] Conner RD, Dandliker RB, Johnson WL. Mechanical properties of tungsten and steel fiber reinforced $Zr_{41.25}Ti_{13.75}Cu_{12.5}Ni_{10}Be_{22.5}$ metallic glass matrix composites. Acta Materialia 1998; 46:6089.

[12] Inoue A, Kong FL, Zhu SL, Shalaan E, Al-Marzouki FM. Production methods and properties of engineering glassy alloys and composites. Intermetallics 2015; 58:20.

[13] Babilas R, Cesarz-Andraczke K, Nowosielski R, Burian A. Structure, properties, and crystallization of Mg-Cu-Y-Zn bulk metallic glasses. Journal of Materials Engineering and Performance 2014; 23:2241.

[14] Go YH, Cho J, Jeong CY, Kang CS, Park JS. Stress distribution of bulk metallic glass/metal laminate composites during uni-axial fracture. Materials Science and Engineering A 2007; 460-461:377.

[15] Park JS, Lim HK, Park ES, Shin HS, Lee WH, Kim WT, Kim DH. Fracture behavior of bulk metallic glass/metal laminate composites. Materials Science and Engineering A 2006; 417:239.

[16] Tariq NH, Hasan BA, Akhter JI, Shaikh MA. Fracture behavior of laminated Zr-based bulk metallic glass under bending. Journal of Alloys and Compounds 2009; 479:242.

[17] Inoue A. Stabilization of metallic supercooled liquid and bulk amorphous alloys. Acta Materialia 2000; 48:279.

[18] Inoue A, Takeuchi A. Recent development and application products of bulk glassy alloys. Acta Materialia 2011; 59:2243.

[19] Schroers J. Processing of Bulk Metallic Glass. Advanced Materials 2010; 22:1566.

[20] Zheng Q, Cheng S, Strader JH, Ma E, Xu J. Critical size and strength of the best bulk metallic glass former in the Mg-Cu-Gd ternary system. Scripta Materialia 2007; 56:161.

[21] Men HK, D. H. Fabrication of ternary Mg–Cu–Gd bulk metallic glass with high glass-forming ability under air atmosphere. Journal of Materials Research 2003; 18:1502.

[22] Cheng HM. Glass forming ability and mechanical properties of Mg-Cu-Ag-Gd Bulk metallic glasses. PhD thesis National Sun Yat-sen University 2005.

[23] Li G, Cai Q, Li H, Zheng L, He B, Sun T. Structure relaxation of $Mg_{65}Cu_{25}Gd_{10}$; metallic glass and its effect on strength. Journal of Wuhan University of Technology--Materials Science Edition 2009; 24:210.

[24] Bae GT, Lee SB, Kim NJ. Effect of alloying elements on the crystallization kinetics of Mg-Cu-(Y, Gd) bulk amorphous alloys. Materials Science and Engineering: A 2007; 489: 449-451.
[25] Li GQ, Cai Q, Zheng LJ, Li HX. EXAFS Studies on Glass-Forming Ability of Amorphous $Mg_{65}Cu_{25}Y_xGd_{10-x}$(x=0,5,10) Alloys. Rare Metal Materials and Engineering. 2008; 37:2081.
[26] Soubeyroux JL, Puech S, Donnadieu P, Blandin JJ. Synthesis and mechanical behavior of nanocomposite Mg-based bulk metallic glasses. Journal of Alloys and Compounds 2007; 434:84.
[27] Rizzi P, Satta M, Enzo S, Georgarakis K, Yavari AR, Baricco M. Crystallisation process in $Mg_{60}Cu_{30}Gd_{10-x}Nd_x$ (x=0, 8.5) amorphous alloys - art. no. 012057. In: Schultz L, Eckert J, Battezzati L, Stoica M, editors. 13th International Conference on Rapidly Quenched and Metastable Materials, vol. 144. Bristol: Iop Publishing Ltd, 2009; 12057.
[28] Inoue A, Kato A, Zhang T, Kim SG, Masumoto T. Mg-Cu-Y amorphous-alloys with high mechanical strengths produced by a metallic mold casting method. Materials Transactions JIM 1991; 32:609.
[29] Park ES, Kang HG, Kim WT, Kim DH. The effect of Ag addition on the glass-forming ability of Mg-Cu-Y metallic glass alloys. Journal of Non-Crystalline Solids 2001; 279:154.
[30] Hui X, Dong W, Chen GL, Yao KF. Formation, microstructure and properties of long-period order structure reinforced Mg-based bulk metallic glass composites. Acta Materialia 2007; 55:907.
[31] Collocott S, East D, Gibson M; Hussain, Z, O'Donnell R; Song S, Venkatesan K, Bulk metallic glasses and amorphous matrix composites. CSIRO internal report 2011.
[32] Laws KJ, Gun B, Ferry M. Effect of die-casting parameters on the production of high quality bulk metallic glass samples. Materials Science and Engineering A 2006; 425:114.
[33] Laws KJ, Gun B, Ferry M. Large-scale production of $Ca_{65}Mg_{15}Zn_{20}$ bulk metallic glass samples by low-pressure die-casting. Materials Science and Engineering A 2008; 475:348.
[34] Schroers J, Paton N. Amorphous metal alloys form like plastics. Advanced Materials and. Processes. 2006; 164:61.
[35] Chang YC. Study on the thermomechanical properties and workability of Mg based bulk metallic glass. PhD thesis National Sun Yat-sen University; 2008.
[36] Cheung TL, Shek CH. Thermal and mechanical properties of Cu-Zr-Al bulk metallic glasses. Journal of Alloys and Compounds 2007; 434-435:71.
[37] Johnson WL. Bulk metallic glasses -- a new engineering material. Current Opinion in Solid State and Materials Science 1996; 1:383.
[38] Amiya K, Inoue A. Mg-based bulk glassy alloys produced by water quenching. In: Hanada S, Zhong Z, Nam SW, Wright RN, editors. 4th Pacific Rim International Conference on Advanced Materials and Processing (PRICM4). Honolulu, Hi, 2001; 23.
[39] Zhang X, Zhang Y, Chen X, Chen G. Bulk metallic glass rings prepared by a modified water quenching method. International Journal of Minerals, Metallurgy and Materials 2009;16:108.
[40] Illeková E, Jergel M, Duhaj P, Inoue A. The relation between the bulk and ribbon $Zr_{55}Ni_{25}Al_{20}$ metallic glasses. Materials Science and Engineering: A 1997; 226-228:388.
[41] Kato H, Kawamura Y, Inoue A, Masumoto T. Bulk glassy Zr-based alloys prepared by consolidation of glassy alloy powders in supercooled liquid region. Materials Science and Engineering A 1997; 226-228:458.
[42] Lee MH, Bae DH, Kim WT, Kim DH, Rozhkova E, Wheelock PB, Sordelet DJ. Synthesis of Ni-based bulk amorphous alloys by warm extrusion of amorphous powders. Journal of Non-Crystalline Solids 2003; 315:89.
[43] Oleszak D, Kolesnikov D, Kulik T. Bulk amorphous $Ni_{59}Zr_{20}Ti_{16}Sn_5$ alloy fabricated by powder compaction. Journal of Alloys and Compounds 2009; 483:162.
[44] Xie G, Louzguine-Luzgin DV, Song L, Kimura H, Inoue A. Dual phase metallic glassy composites with large-size and ultra-high strength fabricated by spark plasma sintering. Intermetallics 2009; 17:512.

[45] Fiedler H, Muhlbach H, Stephani G. The effect of the main processing parameters on the geometry of amorphous metal ribbons during planar flow casting (PFC). Journal of Materials Science 1984; 19:3229.
[46] Ge S, Isac M, Guthrie RIL. Progress of Strip Casting Technology for Steel; Historical Developments. ISIJ International 2012; 52:2109.
[47] Ge S, Isac M, Guthrie RIL. Progress in Strip Casting Technologies for Steel; Technical Developments. ISIJ International 2013; 53:729.
[48] Haga T, Tkahashi K, Ikawaand M, Watari H. Twin roll casting of aluminum alloy strips. Journal of Materials Processing Technology 2004; 153:42.
[49] Ferry M. Chapter 3 - Continuous Casting Processes and the Emergence of DSC. Direct Strip Casting of Metals and Alloys. Woodhead Publishing, 2006; 63.
[50] Yun M, Lokyer S, Hunt JD. Twin roll casting of aluminium alloys. Materials Science and Engineering: A 2000; 280:116.
[51] Johnson WL, Kaltenboeck G, Demetriou MD, Schramm JP, Liu X, Samwer K, Kim CP, Hofmann DC. Beating Crystallization in Glass-Forming Metals by Millisecond Heating and Processing. Science 2011; 332:828.
[52] Urata A, Nishiyama N, Amiya K, Inoue A. Continuous casting of thick Fe-base glassy plates by twin-roller melt-spinning. Materials Science and Engineering A 2007; 449-451:269.
[53] Oh YS, Lee H, Lee JG, Kim NJ. Twin-roll strip casting of iron-base amorphous alloys. Materials Transactions 2007; 48:1584.
[54] Lee JG, Kim HS, Lee S, Kim NJ. Deformation behavior of strip-cast bulk amorphous matrix composites containing various crystalline particles. Materials Science and Engineering A 2007; 449:176.
[55] Zhang T, Zhang X, Zhang W, Jia F, Inoue A, Hao H, Ma Y. Study on continuous casting of bulk metallic glass. Materials Letters 2011; 65:2257.
[56] Duggan G, Browne D. Modelling and simulation of twin roll casting of bulk metallic glasses. Transactions of the Indian Institute of Metals 2009; 62:417.
[57] Zeng J, Koitzsch R, Pfeifer H, Friedrich B. Numerical simulation of the twin-roll casting process of magnesium alloy strip. Journal of Materials Processing Technology 2009; 209:2321.
[58] Nayak RK, Sundarraj S. Selection of Initial Mold-Metal Interface Heat Transfer Coefficient Values in Casting Simulations-a Sensitivity Analysis. Metallurgical and Materials Transactions B 2010; 41:151.
[59] Martinez R, Kumar G, Schroers J. Hot rolling of bulk metallic glass in its supercooled liquid region. Scripta Materialia 2008; 59:187.
[60] Park ES, Kang HG, Lee JC, Huh MY, Kim HJ, Bae JC. Evolution of strain states during rolling of bulk metallic glass canned with crystalline copper. Journal of Materials Processing Technology 2007; 187-188:783.
[61] Wang G, Fang S, Xiao X, Hua Q, Gu J, Dong Y. Microstructure and properties of $Zr_{65}Al_{10}Ni_{10}Cu_{15}$ amorphous plates rolled in the supercooled liquid region. Materials Science and Engineering A 2004; 373:217.
[62] Hwang KC, Park ES, Huh MY, Kim HJ, Bae JC. Effect of thickness reduction on mechanical property and microstructure of Zr-based bulk metallic glass during warm-rolling in the supercooled liquid region. Intermetallics 2010; 18:1912.
[63] Hofmann DCHDC, Suh JY, Wiest A, Lind ML, Demetriou MD, Johnson WL. Development of tough, low-density titanium-based bulk metallic glass matrix composites with tensile ductility. Proceedings of the National Academy of Sciences of the United States of America 2008; 105:20136.
[64] Xu W, Robin L, Zheng R, Laws KJ, Ferry M. Phase redistribution in an in situ Mg-based bulk metallic glass composite during deformation in the supercooled liquid region. Scripta Materialia 2010; 63:556.

[65] Deibler LA, Findley KO. Characterization of an amorphous-crystalline Mg-based composite. Journal of Alloys and Compounds 2008; 463:173.
[66] Hays CC, Kim CP, Johnson WL. Microstructure Controlled Shear Band Pattern Formation and Enhanced Plasticity of Bulk Metallic Glasses Containing in situ Formed Ductile Phase Dendrite Dispersions. Physical Review Letters 2000; 84:2901.
[67] Shamlaye KF, Laws KJ, Ferry M. Supercooled liquid fusion of carbon fibre-bulk metallic glass composites with superplastic forming properties. Scripta Materialia 2016; 111:127.
[68] Hofmann D, Kozachkov H, Khalifa H, Schramm J, Demetriou M, Vecchio K, Johnson W. Semi-solid induction forging of metallic glass matrix composites. Journal of the Minerals, Metals and Materials Society (JOM) 2009; 61:11.
[69] Qiao JW, Zhang Y, Chen GL. Fabrication and mechanical characterization of a series of plastic Zr-based bulk metallic glass matrix composites. Materials and Design 2009; 30:3966.
[70] Peng XK, Heness G, Yeung WY. Effect of rolling temperature on interface and bond strength development of roll bonded copper/aluminium metal laminates. Journal of Materials Science 1999; 34:277.
[71] Ragani J, Volland A, Gravier S, Blandin JJ, Suéry M. Metallic glass/light alloy (MEGA) multimaterials elaborated by co-pressing at high temperature. Journal of Alloys and Compounds 2010; 495: 323-326
[72] Hao SG, Wang CZ, Li M, Napolitano RE, Mendelev MI, Ho KM. Prediction of cooling rate dependent ordering in metallic glass transition using a two-state model. Computational Materials Science 2010; 49:615.
[73] Fujita T, Konno K, Zhang W, Kumar V, Matsuura M, Inoue A, Sakurai T, Chen MW. Atomic-Scale Heterogeneity of a Multicomponent Bulk Metallic Glass with Excellent Glass Forming Ability. Physical Review Letters 2009; 103:075502.
[74] Gun B, Laws KJ, Ferry M. Static and dynamic crystallization in Mg-Cu-Y bulk metallic glass. Journal of Non-Crystalline Solids 2006; 352:3887.
[75] Gun B, Laws KJ, Ferry M. Superplastic flow of a Mg-based bulk metallic glass in the supercooled liquid region. Journal of Non-Crystalline Solids 2006; 352:3896.
[76] Nieh TG, Wadsworth J, Liu CT, Ohkubo T, Hirotsu Y. Plasticity and structural instability in a bulk metallic glass deformed in the supercooled liquid region. Acta Materialia 2001; 49:2887.
[77] Nieh TG, Schuh C, Wadsworth J, Li Y. Strain rate-dependent deformation in bulk metallic glasses. Intermetallics 2002; 10:1177.
[78] Gun B, Laws KJ, Ferry M. Elevated temperature flow behaviour of a Mg-based bulk metallic glass. Materials Science & Engineering A 2007; 471:130.
[79] Puech S, Blandin JJ, Soubeyroux JL. Viscoplastic Forming of Mg Bulk Metallic Glasses in the Supercooled Liquid Region. Metallurgical and Materials Transactions A 2008; 39:1874.
[80] Shen YT, Kim TH, Gangopadhyay AK, Kelton KF. Icosahedral Order, Frustration, and the Glass Transition: Evidence from Time-Dependent Nucleation and Supercooled Liquid Structure Studies. Physical Review Letters 2009; 102:057801.
[81] Kelton KF. Crystallization of liquids and glasses to quasicrystals. Journal of Non-Crystalline Solids 2004; 334:253.
[82] Gangopadhyay AK, Hyers RW, Kelton KF. Nucleation and Thermophysical Properties of Glass-Forming Liquids. Journal of the Minerals, Metals and Materials Society (JOM) 2012; 64:1109.
[83] Ding J, Cheng Y, Ma E. Charge-transfer-enhanced prism-type local order in amorphous $Mg_{65}Cu_{25}Y_{10}$: Short-to-medium-range structural evolution underlying liquid fragility and heat capacity. Acta Materialia 2013; 61:3130.
[84] Gao R, Zhao YF, Liu XJ, Liu ZK, Hui X. Ab initio molecular dynamics simulation of the liquid and amorphous structure of $Mg_{65}Cu_{25}Gd_{10}$ alloy. Physica B: Condensed Matter 2013; 426:65.
[85] Jovri P, Saksl K, Pryds N, Lebech B, Bailey NP, Anders M, Delaplane RG, Franz H. Atomic structure of glassy $Mg_{60}Cu_{30}Y_{10}$ investigated with EXAFS, x-ray and neutron diffraction, and reverse Monte Carlo simulations. Physical Review B 2007; 76:054208.

[86] Ishii A, Iwase A, Fukumoto Y, Yokoyama Y, Konno TJ, Hori F. Effect of thermal annealing on the local structure in ZrCuAl bulk metallic glass. Journal of Alloys and Compounds; 504:S230.
[87] Newville M. IFEFFIT: interactive XAFS analysis and FEFF fitting. Journal of Synchrotron Radiation 2001; 8:322.
[88] Ravel B, Newville M. Athena, Artemis, Hephaestus: data analysis for X-ray absorption spectroscopy using IFEFFIT. Journal of Synchrotron Radiation 2005; 12:537.
[89] Su YG, Chen FL, Chang CM, Wu CY, Chang MH, Chung CA. Tuning the Planar-Flow Melt-Spinning Process Subject to Operability Conditions. Journal of the Minerals, Metals and Materials Society (JOM) 2014; 66:1277.
[90] Lin XH, Johnson WL. Formation of Ti-Zr-Cu-Ni bulk metallic glasses. Journal of Applied Physics 1995; 78:6514.
[91] Slipenyuk A, Eckert J. Correlation between enthalpy change and free volume reduction during structural relaxation of $Zr_{55}Cu_{30}Al_{10}Ni_5$ metallic glass. Scripta Materialia 2004; 50:39.
[92] Kim J-H, Park J, Park E, Kim W, Kim D. Estimation of critical cooling rates for glass formation in bulk metallic glasses through non-isothermal thermal analysis. Metals and Materials International 2005; 11:1.
[93] Sahoo S, Kumar A, Dhindaw BK, Ghosh S. Modeling and Experimental Validation of Rapid Cooling and Solidification during High-Speed Twin-Roll Strip Casting of Al-33 wt pct Cu. Metallurgical and Materials Transactions B 2012; 43:915.
[94] Zapuskalov N. Effect of coiling operation on strip quality of 4.5% Si steel in twin-roll casting process. ISIJ International 1999; 39:463.
[95] Kreith F, Manglik RM, Bohn MS. Principles of Heat Transfer, SI Edition 2011: Cengage Learning.
[96] Lenard J, Primer for flat rolling 2007: Elsevier.
[97] Chang YC, Huang JC, Tang CW, Chang CI, Jang JSC. Viscous Flow Behavior and Workability of Mg-Cu-(Ag)-Gd Bulk Metallic Glasses. Materials Transactions 2008; 49:2605.
[98] Tan CG, Tian YB, Li W, Lin JG. Effects of the non-Newtonian deformation on the crystallization behavior in a Cu-based bulk metallic glass. Materials Science and Engineering A 2013; 586:53.
[99] Young Kyun K, Won Tae K, Do Hyang K. Quasicrystal-reinforced Mg alloys. Science and Technology of Advanced Materials 2014; 15:2:024801.
[100] Huang H, Tian Y, Yuan G, Chen C, Wang Z, Ding W, Inoue A. Secondary phases in quasicrystal-reinforced Mg3.5Zn0.6Gd Mg alloy. Materials Characterization 2015; 108:132.
[101] Wang Q, Du W, Liu K, Wang Z, Li S, Wen K. Microstructure, texture and mechanical properties of as-extruded MgZnEr alloys. Materials Science and Engineering A 2013; 581:31.
[102] Yuan GY, Kato H, Amiya K, Inoue A. Excellent creep properties of Mg-Zn-Cu-Gd-based alloy strengthened by quasicrystals and Laves phases. Journal of Materials Research 2005; 20:1278.
[103] Zheng Q. Mg-Cu(Ag)-Gd Bulk Metallic Glass Forming Alloy: Phase Selection of Melt Crystallization. Science of Advanced Materials 2012; 4:969.
[104] Eckert J, Kahn U, Mattern N, Reger-Leonhard A, Heilmaier M. Bulk nanostructured Zr-based multiphase alloys with high strength and good ductility. Scripta Materialia 2001; 44:1587.
[105] Raghavan R, Murali P, Ramamurty U. On factors influencing the ductile-to-brittle transition in a bulk metallic glass. Acta Materialia 2009; 57:3332.
[106] Castellero A, Moser B, Uhlenhaut DI, Torre FHD, Löffler JF. Room-temperature creep and structural relaxation of Mg-Cu-Y metallic glasses. Acta Materialia 2008; 56:3777.
[107] Castellero A, Uhlenhaut DI, Moser B, Löffler JF. Critical Poisson ratio for room-temperature embrittlement of amorphous $Mg_{85}Cu_5Y_{10}$. Philosophical Magazine Letters 2007; 87:383.
[108] Schroers J, Pham Q, Peker A, Paton N, Curtis RV. Blow molding of bulk metallic glass. Scripta Materialia 2007; 57:341.
[109] Kruzic JJ, Ritchie RO. Determining the toughness of ceramics from Vickers indentations using the crack-opening displacements: An experimental study. Journal of the American Ceramic Society 2003; 86:1433.

[110] Tiryakiou M. On the relationship between Vickers hardness and yield stress in AlZnMgCu Alloys. Materials Science and Engineering A 2015; 633:17.
[111] Zhao JX, Qu RT, Wu FF, Zhang ZF, Shen BL, Stoica M, Eckert J. Fracture mechanism of some brittle metallic glasses. Journal of Applied Physics 2009; 105:6.
[112] Zhang CM, Hui X, Li ZG, Chen GL. Improving the strength and the toughness of Mg-Cu-(Y, Gd) bulk metallic glass by minor addition of Nb. Journal of Alloys and Compounds 2009; 467:241.
[113] Conner RD, Li Y, Nix WD, Johnson WL. Shear band spacing under bending of Zr-based metallic glass plates. Acta Materialia 2004; 52:2429.
[114] Conner RD, Johnson WL, Paton NE, Nix WD. Shear bands and cracking of metallic glass plates in bending. Journal of Applied Physics 2003; 94:904.
[115] Gravier S, Puech S, Blandin JJ, Suéry M. New Metallic Glass/Alloy (MeGA) Rods Produced by Co-extrusion. Advanced Engineering Materials 2006; 8:948.
[116] Mehr VY, Toroghinejad MR, Rezaeian A. Mechanical properties and microstructure evolutions of multilayered Al-Cu composites produced by accumulative roll bonding process and subsequent annealing. Materials Science and Engineering A 2014; 601:40.
[117] Pirgazi H, Akbarzadeh A. Characterization of nanostructured aluminum sheets processed by accumulative roll bonding. International Journal of Modern Physics B 2008; 22:2840.
[118] Su LH, Lu C, Tieu AK, Deng GY, Sun XD. Ultrafine grained AA1050/AA6061 composite produced by accumulative roll bonding. Materials Science and Engineering A 2013; 59:345.
[119] Qu P, Zhou L, Xu H, Acoff V. Microtexture Development of Niobium in a Multilayered Ti/Al/Nb Composite Produced by Accumulative Roll Bonding. Metallurgical and Materials Transactions A 2014; 45:6217.
[120] Motevalli PD, Eghbali B. Microstructure and mechanical properties of Tr-metal Al/Ti/Mg laminated composite processed by accumulative roll bonding. Materials Science and Engineering A 2015; 628:135.
[121] Sharma P, Yubuta K, Kimura H, Inoue A. Brittle metallic glass deforms plastically at room temperature in glassy multilayers. Physical Review B 2009; 80:8.